A Novel Universal Corner Module for Urban Electric Vehicles: Design, Prototype, and Experiment

by

Allison Waters

A thesis
presented to the University of Waterloo
in fulfillment of the
thesis requirement for the degree of
Master of Applied Science
in
Mechanical and Mechatronics Engineering

Waterloo, Ontario, Canada, 2017

Abstract

This thesis presents the work of creating and validating a novel corner module for a three-wheeled urban electric vehicle in the tadpole configuration. As the urban population increases, there will be a growing need for compact, personal transportation. While urban electric vehicles are compact, they are inherently less stable when negotiating a turn, and they leave little space for passengers, cargo and crash structures. Corner modules provide an effective solution to increase the space in the cabin and increase the handling capabilities of the vehicle.

Many corner module designs have been produced in the hopes of increasing the cabin space and improving the road holding capabilities of the wheel. However, none have been used to increase the turning stability of the vehicle via an active camber mechanism while remaining in an acceptable packaging space. Active camber mechanisms are also not a new concept, but they have not been implemented in a narrow packaging space with relatively large camber angle.

Parallel mechanism research and vehicle dynamics theory were combined to generate and analyse this new corner module design. The corner module increases the stability of the urban electric vehicle by cambering the front wheels to $-15°$ when the vehicle is turning. The camber angle augmentation increases the track width which subsequently decreases the center of gravity height. These changes accumulated to increase the stability of the vehicle. The corner module uses two actuators to control the orientation of the wheel. Bias ply tires are incorporated into the corner module to enable the large camber angles. To increase the space in the cabin, the front left and right wheels are not connected by a mechanical linkage, and the motors are mounted to the wheel rim. While disc brakes are integrated into the corner module, the motor is also capable of regenerative braking.

By integrating this corner module into urban electric vehicles, the vehicle size and pollution can be reduced while increasing the cabin space and public space.

Acknowledgements

I would like to thank Dr. Khajepour for his guidance and support throughout my studies as a graduate student. I would not have been able to accomplish as much as I did without his counsel.

Dedication

This thesis is dedicated to my parents and my brother.

Table of Contents

List of Tables **x**

List of Figures **xi**

List of Abbreviations **xv**

List of Symbols **xvi**

1 Introduction **1**

2 Background and Literature Review **5**

2.1 Background Knowledge 5

2.1.1 Vehicle Dynamics 5

2.1.2 Parallel Mechanisms 9

2.2 State-of-the-Art 14

3 Proposed Design **19**

3.1 Product Design Specifications 19

3.2 Concept Generation and Evaluation 21

3.3 Final Solution 24

4 Design Optimization **26**

4.1 Inverse Kinematic Model used in Optimization 26

4.2 Model Validation using Adams/View 29

4.3 Genetic Algorithm 30

4.3.1 Objectives 31

4.3.2 Constraints 32

4.4 Optimization Results 36

4.5 Singularity Analysis 43

4.5.1 Forward Kinematic Model 43

4.5.2 Taghirad Method 47

4.5.3 Zlatonov Method 50

4.6 Sensitivity Analysis 56

5 Suspension Kinematic and Dynamic Modelling **60**

5.1 Bump Camber 60

5.2 Bump Steer 63

5.3 Spring and Damper Selection 65

5.4 Caliper and Rotor Selection 70

5.5 Force Analysis 71

5.5.1 Lateral Dynamics 71

5.5.2 Vertical Dynamics 74

6 Detailed Design **78**

6.1 Rotor Coupler 78

6.2 Upright Coupler 80

6.3 Upright 82

6.4 Upper Control Arm 87

6.5 Fixed-Length Link 89

6.6 Mounts . . . 90
6.6.1 Outboard Cylinder Mount . . . 91
6.6.2 Inboard Cylinder Mount . . . 93
6.6.3 Shock Mount . . . 95

7 Fabrication and Experimental Testing 97
7.1 Fabrication . . . 97
7.2 Sensor Calibration . . . 101
7.3 Equipment . . . 110
7.4 Test Procedure . . . 111
7.5 Experimental Results . . . 112

8 Conclusion and Recommendations 115
8.1 Conclusions . . . 115
8.2 Future Work . . . 117

References 118

APPENDICES 123

A Concept Generation Tables 124
A.1 Generated Concepts from Grübler-Kutzbach Mobility Formula . . . 124
A.2 Configurations for Limb and Joint Combinations with Unknown Joints . . . 126

B Matlab Code 127
B.1 Genetic Algorithm . . . 127
B.2 Inverse Kinematic Model . . . 130
B.3 Forward Kinematic Model . . . 132
B.4 Singularity Determination . . . 133
B.4.1 Taghirad Method . . . 133

B.4.2 Zlatonov Method 134
B.5 3DOF Handling Model Simulink Diagram 137
B.6 2DOF Quarter Car Model Simulink Diagram 138

GLOSSARY **139**

List of Tables

3.1 Estimated vehicle parameters 20
3.2 Lower kinematic joints 22
3.3 Final options for joint and link combinations 23

4.1 Upper and lower limits for free variables [35] 33
4.2 Four cylinders considered in the optimization program [35] 35

6.1 Safety factors against sleeve yield and sleeve slip for various joints. 91

7.1 Configurations examined in the experiment. 113

A.1 Link and joint combinations 124

List of Figures

2.1 Vehicle coordinate system used in corner module design [17] 6

2.2 Parameter definitions for kingpin axis in rear view (a) and side view (b) [10] 8

2.3 Transverse cross-section view of the front suspension diagram. RC is the roll centre and CG is the centre of gravity for the sprung mass. 9

2.4 Loop closure method for a parallel mechanism 11

2.5 NASA eModule [31] 15

2.6 Siemens eCorner [16] 15

2.7 Volvo ACM [36] 16

2.8 Cross-section of the Michelin Active Wheel [26] 16

2.9 GM corner module [7] 17

2.10 Bridgestone in-wheel suspension [29] 17

2.11 The University of Waterloo's corner module developped in the Mechatronic Vehicles Laboratory [30] 18

3.1 Final four options for parallel mechanism configuration and joint selection. The grey oval represents the moving platform. The black lines are links and the blue circles are joints. The letter beside the joint specifies the joint type as per table 3.2 24

3.2 Isometric view of the UCM 25

4.1 Schematic of mathematical model used in hard point optimization 27

4.2 Isometric view of the Adams/View model. 29

4.3 Matlab model cylinder lengths as compared with Adams/View model cylinder lengths. 30

4.4 Location of origin and orientation of coordinate system used in optimization 33

4.5 Map of input workspace. 37

4.6 Displacement of theoretical contact patch with respect to its nominal position at 0° steer and 0° camber. 38

4.7 Longitudinal displacement of the contact patch plotted against steer angle for various constant camber orientations. 39

4.8 Displacement of the wheel center with respect to its nominal position at 0° steer and 0° camber. 40

4.9 Wheel spin angle, β, for various camber and steer angles. 41

4.10 Rear cylinder length for various camber and steer angles. 42

4.11 Steer and camber angles of the wheel at various rear and cross cylinder lengths. 46

4.12 Sensitivity of the steer angle output to the rear cylinder length input. . . . 57

4.13 Sensitivity of the steer angle output to the cross cylinder length input. . . 58

4.14 Sensitivity of the camber angle output to the rear cylinder length input. . . 59

4.15 Sensitivity of the camber angle output to the cross cylinder length input. . 59

5.1 Geometric definition of the roll center with respect to the sprung mass CG. 61

5.2 Camber alteration at approximately 0° steer angle. 62

5.3 Steer and camber alteration from approximately 0 steer angle and 0 camber angle. 63

5.4 Steer alteration at approximately 0°, $-5°$,$-10°$ and $-15°$ camber angles. . 64

5.5 Cross cylinder length for various camber and steer angles [35]. 65

5.6 Transmissibility results for selected spring and damper. 68

5.7 Desired and actual force-velocity curves for different valving options. Positive force is compression and negative is rebound. 69

5.8 Wheel assembly showing the packaging of the selected rotor and caliper. The rotor connects to the wheel via the rotor coupler. 71

5.9 Forces in the cylinders. 73

5.10 Forces in the fixed-length link and upper control arm outboard joint. . . . 74
5.11 Two degree of freedom, quarter car model during the event of bump impact at 100 km/hr. 76
5.12 Upper control arm rotational acceleration [rad/s^2]. 77

6.1 Upright Coupler. 80
6.2 Upright with mesh, fixture (green) and rigid parts (orange). 84
6.3 Upright simulation results for load case 1: 1 g lateral acceleration at 15° steer and 0° camber. 85
6.4 Upright simulation results for load case 2: 1 g lateral acceleration at 15° steer and −15° camber. 86
6.5 Upright simulation results for load case 3: 1 g longitudinal deceleration with locked braking. 87
6.6 Final design of the left front wheel's upper control arm. 88
6.7 Von Mises stress (N/m^2) developed in the upper control arm damper mount. 89
6.8 Exploded view of the fixed-length link assembly. 90
6.9 Outboard cylinder mount showing the locations of bolt A and bolt B. . . . 92
6.10 Inboard cylinder mount finite element analysis. 94
6.11 Shock mount finite element analysis. 96

7.1 3D printed, scaled model of the corner module. 98
7.2 Milled aluminum components. 99
7.3 Upper control arm assembly welding. 100
7.4 Final assembly of the steering and suspension system for the corner module. 100
7.5 Top view of the left side corner module showing the front, rear and ride height rotary potentiometers. 102
7.6 Ride height sensor geometry. 102
7.7 Ride height sensor calibration curves for the angle between h and dz, and the z- and y-components of the outboard upper control arm joint. 103
7.8 Rear sensor top view. 104

7.9 Steer angle for given front and rear sensor voltages at ride height. 105
7.10 Camber angle for given front and rear sensor voltages at ride height. 106
7.11 Steer angle as determined by the sensor voltages. 107
7.12 Steer angle as determined by the sensor voltages. 108
7.13 Rear cylinder length vs rear sensor voltage at ride height for constant front sensor voltage. 109
7.14 Cross cylinder length vs front sensor voltage at ride height for constant rear sensor voltage. 109
7.15 Test equipment 110
7.16 Control and hydraulic system diagram. 111
7.17 Actual and theoretical angles at ride height for various configurations. . . . 113
7.18 Steer and camber deviation at ride height for various configurations. 114

A.1 Parallel mechanism configuration 126

B.1 Simulink diagram for 3DOF handling model. 137
B.2 Simulink diagram for 2DOF quarter car model. 138

List of Abbreviations

CG center of gravity xii, 15, 60, 61, 72

CGK Chebychev-Grübler-Kutzbach 10

DOF degrees of freedom 10

UCM Universal Corner Module 25

UEV urban electric vehicle 2

List of Symbols

$\boldsymbol{AI}$ Location vector of the inboard spherical joint on the rear cylinder. 26, 29, 34

$\boldsymbol{AO}$ Instantaneous location vector of the outboard spherical joint on the rear cylinder. 26, 34

A_p Brake caliper piston area. 70

$\boldsymbol{BI}$ Location vector of the inboard spherical joint on the fixed-length link. 26, 29, 34

$\boldsymbol{BO}$ Instantaneous location vector of the outboard spherical joint on the fixed-length link. 26, 28, 34

$\boldsymbol{CI}$ Location vector of the inboard spherical joint on the cross cylinder. 26, 29

$\boldsymbol{CO}$ Instantaneous location vector of the outboard spherical joint on the cross cylinder. 26

FoS Factor of safety. The ratio of the maximum stress or load a part may experience over the estimated stress or load the part is expected to experience. 79

F_{zfl} Normal force at the contact patch on the front left tire. 70

$\boldsymbol{J_I}$ Jacobian input matrix. 51

$\boldsymbol{J_O}$ Jacobian output matrix. 51

$\boldsymbol{J_X}$ Jacobian matrix of the platform twist. 51

$\boldsymbol{J}$ Jacobian Matrix: a matrix describing the homogeneous relationship between the velocity of the actuated joints and the rate of change in the moving platform's twist vector. 52

$\boldsymbol{J_a}$ Jacobian matrix of the active joints. 51

$\boldsymbol{J_p}$ Jacobian matrix of the passive joints. 51

$\boldsymbol{KI}$ Instantaneous position of the inboard spherical joint on the rear sensor. 104

$\boldsymbol{KO_i}$ Initial position of the outboard spherical joint on the rear sensor. 104

K_{sbr} Steer-by-roll coefficient. 72

$\boldsymbol{LI}$ Instantaneous position of the inboard spherical joint on the front sensor. 104

$\boldsymbol{LO_i}$ Initial position of the outboard spherical joint on the front sensor. 104

K_{MR} Motion ratio relating the wheel travel to the spring travel. 65

N Total degrees of freedom for all joints, active and passive, considered in the calculation of the Jacobian matrix. 51, 54

P_{brake} Brake pad pressure on the rotor. 70

$\boldsymbol{P}$ A vector from the fixed origin to a point on the moving platform. 44

r_e The effective rotor radius is the radius to the position where the normal force from the brake pads is applied. 70

r_{rotor} Rotor radius. 70

Sp Proof strength. 79

$\boldsymbol{S}$ Location vector of the outboard spherical joint on the upper control arm. 26, 29, 43, 65, 104

a Longitudinal distance from the front wheels to the CG. 72

α Side slip angle. 72

$\boldsymbol{a_i}$ Position vector in base reference frame describing the position of the base-connected joint of limb i with respect to the base reference frame 11

β Wheel spin angle: the rotation angle about the y-axis in the platform's (wheel's) coordinate system after it has rotated about the z-axis by an angle of δ then about the x-axis by an angle of γ. 27, 28, 40, 43

q Number of Independent Closed Loops: total number of independent, closed loops 10

c Damping coefficient. 67

δ Steer angle:the rotation angle about the z-axis in the platform's (wheel's) coordinate system. 27, 43, 72

f_{n1} Body (sprung mass) natural frequency in Hertz. 66

f_{n2} Wheel (unsprung mass) natural frequency in Hertz. 66

γ Camber angle: the rotation angle about the x-axis in the platform's (wheel's) coordinate system after it has rotated about the z-axis by an angle of δ. 27, 43, 72

f_i Joint Mobility: the degrees of freedom in a joint coupling two bodies 10

$\dot{\boldsymbol{L}}$ Velocity vector of the actuated joints in a parallel mechanism. 12, 50

p Number of Joints: total number of joints in a system 10

k_s Spring stiffness. 65

k_u Tire stiffness. 66

ε_y Lateral contact patch displacement measured from the contact patch at 0° steer and 0° camber in the vehicle's coordinate system. 31

v Lateral velocity. 72

l_{free} Length of the spring without any load applied. 65

ε_x Longitudinal contact patch displacement measured from the contact patch at 0° steer and 0° camber in the vehicle's coordinate system. 31

u Longitudinal velocity. 72

m_f Front sprung mass. 66

M Mobility: the degrees of freedom of a multi-body system 10

b_k Motion Parameter: the number of motions not suppressed by a mechanism after loop closure 10

n The mobility (degrees of freedom) of the moving platform on a parallel mechanism. 51, 54

$\boldsymbol{\Omega_p}$ Velocity vector of the passive joints in a parallel mechanism. 50

ϕ Body roll angle. 72

$\boldsymbol{b_i}$ Position vector in platform reference frame describing the position of the platform reference frame with respect to the platform-connected joint of limb i 11

$\boldsymbol{c_i}$ Position vector in base reference frame describing the position of the platform reference frame with respect to the platform-connected joint of limb i 11

$\boldsymbol{p}$ Position vector in base reference frame describing the position of the platform reference frame with respect to the base reference frame 11

r Jacobian Matrix Rank: the rank of a mechanism's matrix which relates the input actuator velocities to the output end-effector velocities 10

$\boldsymbol{R}$ Rotation matrix of the platform reference frame with respect to the base reference frame 11

s Longitudinal slip. 79

$\dot{\boldsymbol{X}}$ Rate of change in twist for a parallel mechanism. 12, 50

$\hat{\boldsymbol{a}}$ Rear cylinder unit vector describing the direction from $\boldsymbol{AI}$ to $\boldsymbol{AO}$. 47

$\hat{\boldsymbol{b}}$ Fixed-length link unit vector describing the direction from $\boldsymbol{BI}$ to $\boldsymbol{BO}$. 48

$\hat{\boldsymbol{c}}$ Cross cylinder unit vector describing the direction from $\boldsymbol{CI}$ to $\boldsymbol{CO}$. 47

$\dot{l}_A$ Velocity of the prismatic joint on the rear cylinder. 50

$\dot{l}_C$ Velocity of the prismatic joint on the cross cylinder. 50

$\boldsymbol{\omega_A}$ Rear cylinder rotational velocity vector. 47, 51

$\boldsymbol{\omega_B}$ Fixed-length link rotational velocity vector. 51

$\boldsymbol{\omega_C}$ Cross cylinder rotational velocity vector. 47, 51

ω_x Camber rate of change in the moving platform (wheel assembly). 50

ω_y Spin rate of change in the moving platform (wheel assembly). 50

ω_z Steer rate of change in the moving platform (wheel assembly). 50

ω_{n1} Body (sprung mass) natural frequency in rad/s. 66

ω_2 Wheel (unsprung mass) natural frequency in rad/s. 66

r Yaw rate. 72

ζ Damping ratio. 67

Chapter 1

Introduction

In 2050, the global urban population is projected to increase by 64 percent of the urban population in 2014. An additional 2.5 billion people will be living in cities by 2050 [4]. Sustainable urbanization will be imperative to maintain a high quality of life for all citizens living in these densely populated cities. The growing population will require an increase in public facilities such as hospitals, schools and residences. City developers will be faced with building more infrastructure within the confines of the already existing space.

A key factor to solving the increased population density issue lies with the sustainable development of the transportation industry. The majority of commuters travel to and from work in vehicles that can seat a minimum of five people. However, commute carpooling has not gained significant popularity to reduce traffic and congestion. The real estate required for transportation could be reduced if the average vehicle on the road was smaller than the current average car. Another important problem to consider with the significant increase in population density is the increase in pollution. More vehicles on the roads will increase the pollution in these densely populated cities.

Many solutions have been proposed to solve the two major challenges facing the growing population in major cities. Such solutions include hybrid vehicles, personal aircraft or increasing public transportation. However, one solution is gaining traction for its practicality and modest transition from the current state of the automotive industry. UEVs are subcompact vehicles that can seat up to two passengers and have minimal cargo space. The UEV will reduce the space required per individual not only on roads and highways, but also in parking lots. Therefore, more commuters could be accommodated by the current road infrastructure. The UEV uses electric motors for its propulsion system and produces zero emissions. Lastly, autonomous UEVs would allow vehicles on highways and roads to travel in close proximity to one another. This would also reduce the space required for personal transportation in densely populated cities.

However, UEVs face their own challenges before they can be adopted by the automotive industry and the general public. By definition, there is little space within this subcompact vehicle for passengers, cargo, auxiliary systems and crash structures. For the UEV to be competitive in the current automotive market, it must feature auxiliary systems such as air conditioning, radio, heating, etc. along with ample space for passengers and cargo. To increase the space within UEVs and other vehicles, corner modules have been proposed as a solution. Corner modules may also be used to increase the handling stability of a UEV when they include features such as active camber or ride height control. Lastly, UEVs are generally low to medium production vehicles. This will especially be the case when UEVs are first introduced into the market. Therefore, the modular aspect of corner modules allows companies to adapt the vehicle's platform to a changing market demand while keeping the suspension, powertrain and steering system the same.

A corner module is a subsystem of the chassis consisting of the suspension, steering system and wheel assembly. The electric motor, rotor and caliper are housed within the wheel assembly. The steering system is no longer mechanically connected to the steering wheel. Instead the wheel motion is controlled by one or more actuators. By using a corner module, the powertrain, steering system and suspension are located in the wheel well instead of within the vehicle body.

In this thesis, a novel corner module design to be used on a three-wheeled urban electric vehicle in the tadpole configuration is proposed. The proposed corner module provides a solution to the two major challenges preventing the mass production of urban electric vehicles. It minimizes the packaging space required for the powertrain, steer system and suspension. By using only three wheels, the space required for these systems is further reduced. However, the used of three wheels instead of four increases the instability of the vehicle. The proposed corner module solves the inherit instability of the three-wheeled urban electric vehicle using active camber. The corner module is optimized to remain with the narrow, predefined packaging space.

This thesis begins by introducing the hurdles that the urban electric vehicles must overcome to be a viable solution to urban population growth and, therefore, defining the need for the corner module. A literature review presents the required background knowledge and state-of-the-art that was used to develop the corner module. The concept generation and selection as well as a detailed explanation of the final concept are shown after the literature review. In chapter four, the hard points of the corner module are optimized using a genetic algorithm. The optimization successfully determined the geometry of the corner module based on the nonlinear, discrete objectives and constraints; and the results are presented. A singularity analysis and sensitivity analysis are performed on the optimized corner module to evaluate its theoretical stiffness and controllability. The corner module is then modelled with the theoretical urban electric vehicle parameters to determine bump coefficients and select a spring, damper, rotor and caliper using multiple vehicle dynamics models. A force analysis is also completed to determine the loads in the suspension members during various vehicle load cases. Chapter six offers the detailed design of the various corner module components. The fabrication and testing of the corner module prototype are exhibited in chapter seven. The test results successfully validate the corner module kinematic models. The final chapter offers concluding thoughts on the research and recommends improvements for future work.

Chapter 2

Background and Literature Review

A literature review of the relevant information is presented below. Background knowledge is discussed first; then, the state-of-the-art for existing corner module technology is reviewed. Within background knowledge, vehicle dynamics and parallel mechanisms are discussed. They include the fundamental principles on which the corner module was developed.

2.1 Background Knowledge

2.1.1 Vehicle Dynamics

The corner module was developed using the coordinate system in accordance with DIN 70000 and ISO 8855 as shown in figure 2.1. The longitudinal axis (x-axis) always points in the direction that the vehicle or wheel is travelling. The longitudinal axes of the vehicle and wheel will not always point in the same direction. The vertical axis will always be in the opposite direction of gravity. In this thesis, the lateral direction will point to the left side of the vehicle or wheel regardless of which wheel coordinate system is being considered.

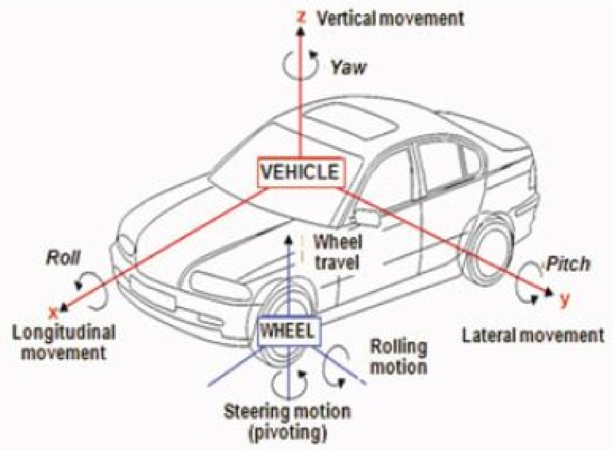

Figure 2.1: Vehicle coordinate system used in corner module design [17]

.

A corner module consists of independent suspension and steering systems. The proposed corner module has similar behaviour to a double wishbone suspension, therefore, the kinematics for a double wishbone suspension is presented. A turn is initiated by the driver via a steering input which is sent to the wheel by either a mechanical or mechatronic system. This causes the wheel to rotate about its kingpin axis. The kingpin axis is defined as the axis passing through the two joints that connect the upper and lower control arms to the wheel in a double wishbone suspension. In more general terms, it is the axis about which the wheel rotates where no rotation occurs. Due to the location and orientation of the kingpin axis with respect to the wheel, the wheel will translate and rotate as it is steered and as the spring is compressed or extended. The kingpin axis can be strategically placed and oriented to manipulate the passive wheel translation and rotation to improve vehicle handling capabilities.

The orientation and location of the kingpin axis with respect to the wheel can be defined using four of the following parameters: inclination angle, caster angle, inclination offset, caster offset and caster trail (figure 2.2). It is preferable to have positive caster trail for stability purposes [10]. If the steering system were to fail, the wheel would gain an extra degree of freedom. With positive caster trail, the wheel would self-align so that the vehicle would continue to drive straight. Static caster trail values are typically between 10 mm and 40 mm [1]. A positive static caster angle and negative caster offset can be selected to increase vehicle handling. Caster angles are usually between 0° and 5° in the static position [10]. Both the inclination and caster angles induce passive camber in the wheel when it is steered. The inclination angle causes positive camber regardless of the direction of the steered wheel. However, the caster angle causes negative camber on the outside wheel and positive camber on the inside wheel of the vehicle. Due to the lateral forces at the contact patch caused by camber, it is preferrable to have negative camber on the outside wheel and positive camber of the inside wheel [17]. This also increases the handling capabilities of the vehicle. Therefore, it is ideal to have zero inclination angle and to select an optimal value for the caster angle when considering the camber alteration induced by steer. Although, the inclination angle is hardly ever zero due to packaging constraints. The inclination angle for passenger cars is generally between 11° to 15.5° and the inclination offset is -18 mm to +20 mm [18]. The combined effect of caster angle, caster trail, inclination angle and caster offset will impact the amount of vehicle jacking when the wheels are steered [10]. Lastly, tire wear and steering loads can be reduced by minimizing caster trail, inclination offset, inclination angle and caster angle. Therefore, there exist conflicting objectives when selecting the caster trail, caster angle and caster offset.

The kingpin axis changes position and orientation as the wheels are steered and as the spring is compressed or extended. Spring travel is caused by bumps in the road and by lateral and longitudinal accelerations acting on the vehicle body causing it to roll or pitch. Body roll induces three main wheel motions: steer-by-roll, camber-by-roll and scrub-by-roll which are related to the wheel motions caused by bump: bump steer, bump camber and bump scrub. An instantaneous centre of rotation can be defined for the sprung mass for

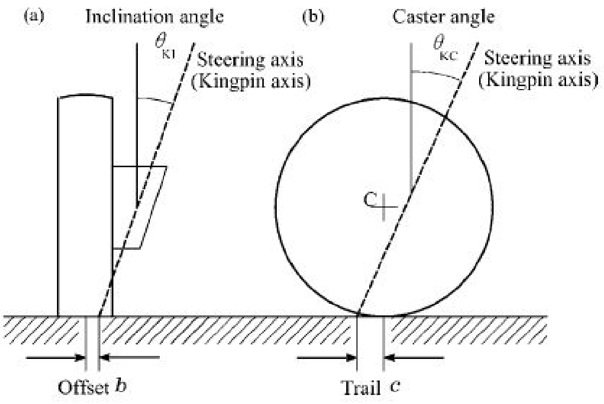

Figure 2.2: Parameter definitions for kingpin axis in rear view (a) and side view (b) [10]

roll and pitch. These instantaneous centres of rotation are not static as they move with sprung mass movement. In a double wishbone suspension, the placement and orientation of the upper and lower control arms dictate the position and translation of the roll and pitch instantaneous centres of rotation (roll centre and pitch centre).

SAE defines the roll axis of the vehicle as the axis in the fore-aft direction which the sprung mass rotates about [10]. The roll axis can be derived using the geometry of the front and rear suspensions. Figure 2.3 shows a transverse cross-section view of a vehicle's front, double wishbone suspension for one time instant. The lower and upper control arms form a four-bar linkage for each wheel. The roll centre of each wheel is found at the intersection of two lines which are co-linear with the upper and lower control arms. Knowing the locations of the left and right suspension roll centres, the front suspension creates another four-bar linkage with the vehicle body. At this instant, the wheel-road contact points and suspension roll centres are the joints of the four-bar linkage. Then the roll centre of the front suspension is the roll centre of the coupler link connecting the left and right suspension roll centres. This same procedure can be done to find the rear suspension roll centre. Then, the roll axis is the line passing through the front and rear suspension roll centres. The roll axis will not always be parallel with the longitudinal axis

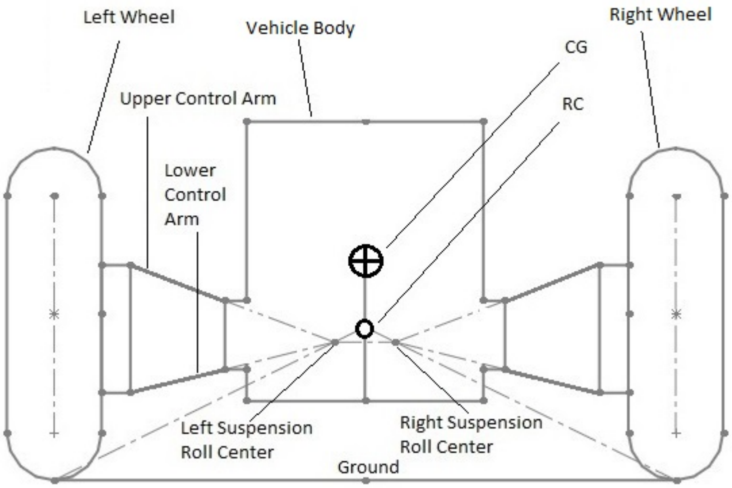

Figure 2.3: Transverse cross-section view of the front suspension diagram. RC is the roll centre and CG is the centre of gravity for the sprung mass.

and it will not always lie in the xz-plane. This method for finding the front and rear roll centres makes a few assumptions. This method treats the wheel contact patch as a point and does not account for tire compression. It also assumes that the control arms rotate about an axis parallel to the longitudinal axis. This is not always the case for double wishbone suspensions.

2.1.2 Parallel Mechanisms

Concepts for the corner module were generated under the assumption that the proposed corner module would take a configuration that could be treated as a parallel mechanism. Therefore, knowledge of the kinematic and dynamic analysis of parallel mechanisms was required to complete this thesis. A parallel mechanism or robot is similar to a serial robot in the sense that the motion of the end-effector with respect to the base is of interest. However, while a serial robot has one limb connecting the base to the end-effector, a parallel robot has two or more limbs.

When designing a serial or parallel robot, it is important to know how many DOF the robot has when the actuators are free to move. Many theories have been proposed to determine the DOF with the most widely known formula being the extended CGK mobility formula [12]. The extended CGK mobility formula is shown in equation 2.1.

$$M = \sum_{i=1}^{p} f_i - \sum_{k=1}^{q} b_k \tag{2.1}$$

Equation 2.1 states that the mobility of the system, M is equal to the sum of the each joint's DOF, f_i, minus the sum of motion parameters for each independent closed loop, b_k. p is the number of joints. q is the number of independent closed loops. However, this formula for mobility, M, does not hold true for all parallel robots in their entire workspace as proved by Gogu [11]. To determine the mobility of any mechanism, the joint DOFs that lose their independence after loop closure, r, should be subtracted from the sum of the DOF of each joint to determine the mobility of the mechanism (eq. 2.2). The joint DOFs that lose their independence, r, is equal to the rank of the Jacobian matrix.

$$M = \sum_{i=1}^{p} f_i - r \tag{2.2}$$

The rank of the homogeneous linear set of velocity constraint equations characterizing the mechanism is equal to the joint DOFs that lose their independence after loop closure [12].

The homogeneous linear set of velocity constraint equations (also known as the Jacobian matrix [15]) can be determined by using velocity loop closures or screw coordinates [34]. The velocity loop closure method was used to determine the mobility and singularities of the proposed mechanism. The velocity loop closure method can be completed through inverse or forward kinematics [32]. Forward kinematics (also known as direct kinematics [13]) assumes that the input actuator parameters are known. The input actuator parameters are used to determine the position and orientation of the end-effector. Inverse kinematics uses the known position and orientation of the end-effector to calculate the input actuator parameters. Inverse kinematic analysis is usually less complex than forward

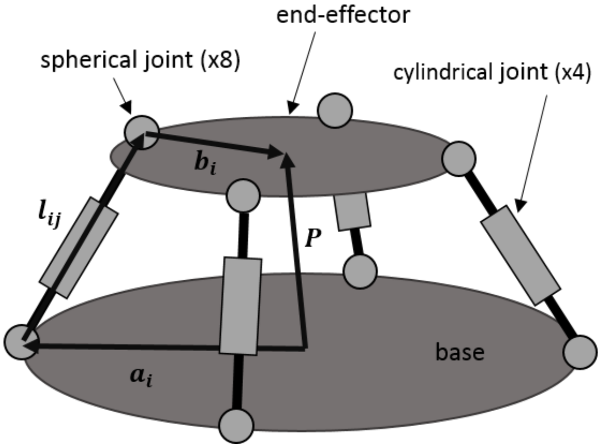

Figure 2.4: Loop closure method for a parallel mechanism

kinematic analysis for parallel mechanisms [34]. Figure 2.4 shows a parallel mechanism with four limbs. Each limb consists of two spherical joints and one cylindrical joint.

Using inverse or forward kinematics, a system of equations to describe the parallel mechanism can be determined. Loop closure method defines a platform vector, $\boldsymbol{p}$, from the base frame of reference to the moving platform frame of reference. The platform vector is described by creating a closed vector loop with the platform vector and one limb vector set. The closed vector loop for one limb is described in equation 2.3 using inverse kinematics and in equation 2.4 using forward kinematics.

$$\sum_{j=1}^{n} \boldsymbol{l_{ij}} = \boldsymbol{c_i} + \boldsymbol{p} - \boldsymbol{a_i} \tag{2.3}$$

$$\boldsymbol{p} - \boldsymbol{c_i} = \sum_{j=1}^{n} \boldsymbol{l_{ij}} - \boldsymbol{a_i} \tag{2.4}$$

The position vectors $\boldsymbol{a_i}$ and $\boldsymbol{b_i}$ are known constants. The vector, $\boldsymbol{c_i}$, describing the reference frame of the moving platform with respect to the platform-connected end of the limb is found on the left side of equation 2.4 because it contains the rotation matrix, $\boldsymbol{R}$, of the moving platform with respect to the base reference frame (eq. 2.5).

$$\boldsymbol{c_i} = \boldsymbol{R}\boldsymbol{b_i} \tag{2.5}$$

Forward kinematics is more complex because two separate terms describe the position and orientation of the platform. When cylindrical or prismatic joints are used as actuators, it is also difficult to calculate because usually only the lengths of the actuated joints are known, but not their orientations.

In order to evaluate the feasibility and workspace of a parallel mechanism, it is important to know if any singularities exist in the workspace. There exists six types of singularities: redundant input (RI-type), redundant output (RO-type), impossible input (II-type), impossible output (IO-type), redundant passive motion (RPM-type) and increased instantaneous mobility (IIM-type) [37][13]. There are also constraint singularities, but these singularities can be classified as IIM-type singularities [39][38].

RI-type and RO-type singularities are also known as inverse and forward singularities or type 1 and type 2 singularities, respectively [13]. RI-type and RO-type singularities can be determined from the velocity equations of the parallel mechanism. By taking the time derivative of loop closure equations (eq. 2.3), an equation relating the actuated joint velocities to the rate of change in twist of the moving platform can be derived (eq. 2.6). Equation 2.7 is found by rearranging the velocities equations (eq. 2.6) for each limb and transforming them into matrix format. The Jacobian matrix relates the velocity of the actuated joints, $\dot{\boldsymbol{L}}$, to the rate of change in twist vector, $\dot{\boldsymbol{X}}$, of the parallel mechanism (eq. 2.8) [15][13][34].

$$\sum_{j=1}^{n} \dot{\boldsymbol{l}}_{\boldsymbol{ij}} = \boldsymbol{\omega} \times \boldsymbol{R}\boldsymbol{b_i} + \dot{\boldsymbol{p}} \tag{2.6}$$

$$\boldsymbol{J_l}\dot{\boldsymbol{L}} = \boldsymbol{J_x}\dot{\boldsymbol{X}} \tag{2.7}$$

$$\boldsymbol{J} = \boldsymbol{J_l^{-1}}\boldsymbol{J_x} \tag{2.8}$$

A RI-type singularity occurs when the moving platform losing one or more degrees of freedom [34]. The inverse Jacobian matrix becomes rank deficient at this point (eq. 2.9). A RO-type singularity occurs when the moving platform gains one or more degrees of freedom which cannot be controlled by the actuated joints [34]. The forward Jacobian matrix becomes rank deficient at a RO-type singularity (eq. 2.10). Combined singularity (also called type 3) occurs when both of the inverse and forward Jacobian matrices are rank deficient [34][13].

$$det(\boldsymbol{J_l}) = 0 \tag{2.9}$$

$$det(\boldsymbol{J_x}) = 0 \tag{2.10}$$

IO-type singularities occur when there exists a non-zero output velocity where there is not a possible input velocity to induce the output velocity [40][6][13]. Therefore, equation 2.7 cannot be solved for any active and passive velocity input for this particular velocity output. An II-type singularity is the opposite of an IO-type singularity. An II-type singularity occurs when a non-zero actuated input velocity exists where there is no feasible combination of output velocity and passive velocity [40][6][13]. The set of velocity equations (eq. 2.7) cannot be satisfied by any combination of output velocity and passive velocity vectors for this particular actuated input velocity vector. Zlatanov demonstrated in his thesis that although IO-type singularities can occur simultaneously with RI-type singularities and II-type singularities can occur with RO-type singularities, this is not always the case as one singularity type may occur without the other [40].

RPM-type singularities occur when the passive joints have a nonzero velocity vector while both active joint velocities and output velocities are equal to zero [40][6][13]. When a RPM-type singularity occurs equation 2.7 cannot be solved using inverse or forward kinematics [40]. IIM-type singularities occur when the mechanism gains one or more degrees of freedom as compared to the operational (full cycle [40] or global [39]) degrees of freedom of the mechanism [40][6][13]. Constraint singularities are a subset of IIM-type singularities, and can only occur in constrained parallel mechanisms [39]. Constrained parallel mechanisms have limbs that do not necessarily have the same degrees of freedom as the moving platform. The combined constraints of each limb result in the parallel mechanism's degrees of freedom. However, when the constrained system created by the joints loses rank, the instantaneous degrees of freedom of the parallel mechanism will increase by one or more degrees of freedom [39]. It was demonstrated by D. Zlatanov et al. that constraint singularities can permit the parallel mechanism to alter its configuration space, thus changing its mode of operation [38].

2.2 State-of-the-Art

The corner module is not a new concept. There have been previous corner modules generated by a variety of companies and research groups. Some corner module concepts have been patented, however, the technology is still in its early stages and has not reached the consumer market. The corner module is growing in popularity due to its ease of assembly with the frame and compact packaging. A few companies who have published corner module concepts include NASA, Siemens, Volvo, Michelin, General Motors and Bridgestone. All of the concepts make use of in-wheel electric motors and brake-by-wire systems. The information in section 2.2 is summarized in the conference paper by Waters and Khajepour [35].

NASA has developed a modular robotic vehicle (MRV) as a prototype for future urban electric vehicles and land vehicles for space missions. The MRV uses a corner module titled the eModule. The eModule includes passive suspension, and an electric motor to steer the wheel [8]. Each eModule is capable of rotating $\pm 180^\circ$ and can output approximately 258 Newton-meters of torque [31]. Figure 2.5 shows NASA's eModule. The eModule uses centerline steering as the kingpin offset and kingpin inclination angle are equal to zero.

Figure 2.5: NASA eModule [31]

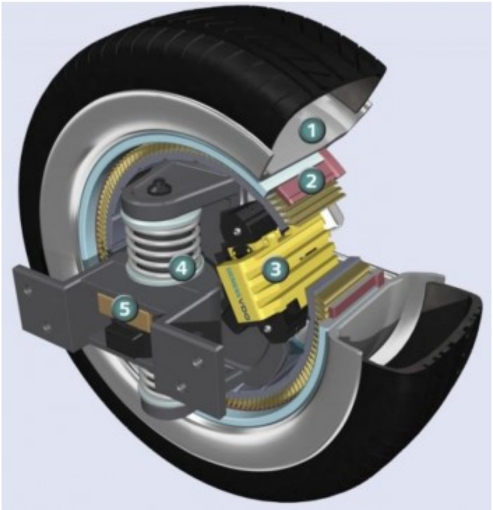

Figure 2.6: Siemens eCorner [16]

While the bump steer of the eModule is approximately equal to zero, the eModule requires a large packaging space, and it increases the vehicle's CG height as the steering motor is above the wheel. An increase in CG height causes the vehicle to be more susceptible to roll-over at high speed turning.

Siemens has introduced a concept that is more compact than NASA's eModule. Siemens' eCorner is very similar to the eModule in the sense that it uses an electric motor to steer, however, additionally it has a compact active suspension system [16]. One eCorner without cooling wou1d be capable of producing 150 Newton-meters of torque [33]. Siemens' eCorner is shown in figure 2.6. The Siemens eCorner is very compact, but it is not capable of active or passive camber alteration. Therefore, the wheels will have to endure the full lateral load as opposed to the lateral acceleration being distributed between the springs and the tires.

The novelty of Volvo's corner module, the Autonomous Corner Module (ACM), is that it provides some anti-roll stability to the vehicle with an adjustable torsional spring incorporated into the upper control arm (fig. 2.7) [36]. The ACM includes an in-wheel

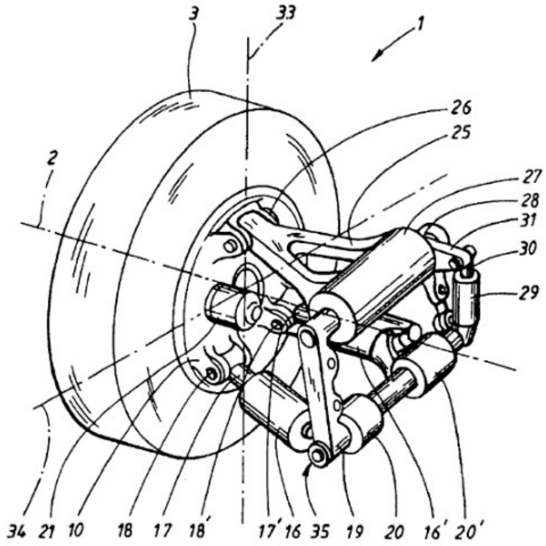

Figure 2.7: Volvo ACM [36]

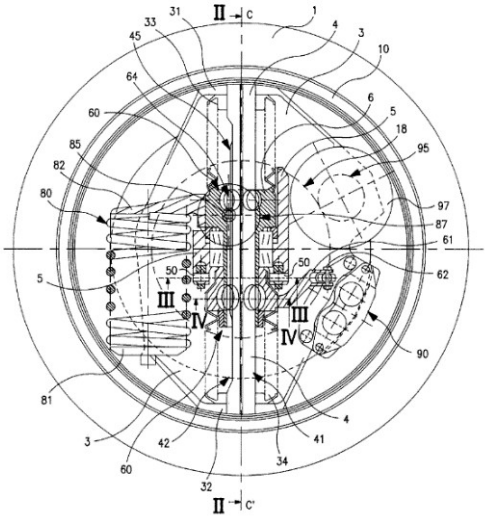

Figure 2.8: Cross-section of the Michelin Active Wheel [26]

electric motor capable of regenerative braking accompanied by a friction drum brake in case additional braking is required [16]. Electric linear actuators are used in the ACM to control the steering angle of the wheel in contrast to the eModule and eCorner which use electric motors [23].

Michelin's Active Wheel is capable of regenerative braking and active suspension (fig. 2.8) [26]. The spring inside the wheel is used to support the weight of the vehicle while the vertical actuator in the middle of the wheel controls the vertical motion of the wheel. The Active Wheel also permits active camber [25]. The wheel can be steered using a single linear actuator [16].

General Motor's corner module resembles a typical double wishbone arrangement except it includes steering and camber actuators. The camber actuator is coupled with the upper control arm [7]. Figure 2.9 shows the suspension geometry for General Motor's corner module.

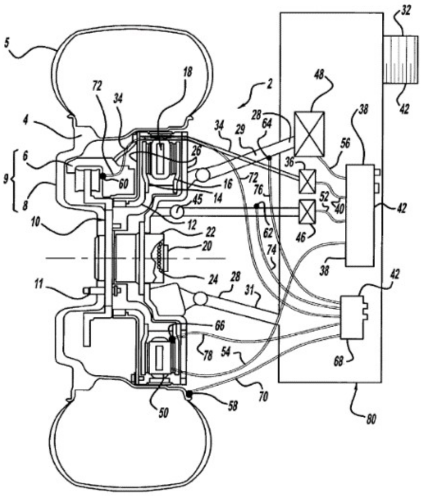

Figure 2.9: GM corner module [7]

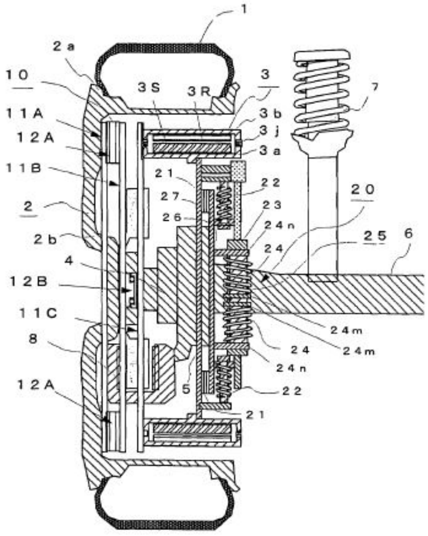

Figure 2.10: Bridgestone in-wheel suspension [29]

All of the designs previously discussed connect the electric motor and brake-by-wire system directly to the wheel before the spring resulting in a large unsprung mass. Large unsprung masses contribute to poor road holding and ride comfort characteristics for the vehicle. Bridgestone has invented a solution to increase corner module feasibility. Bridgestone's In-Wheel Motor System connects the electric motor and brake-by-wire system to the wheel through the spring and dampers, shown in figure 2.10, and consequently, reduces the unsprung mass of the for the vehicle. Vertical and horizontal cross guides couple the rotational motion of the motor to the wheel while allowing the wheel to translate with respect to the motor [29]. This mechanism improves the road holding capabilities of the wheel, however, it still requires a shock absorber to support the weight of the vehicle. A steering system has not yet been integrated with Bridgestone's In-Wheel Motor System.

The University of Waterloo's Mechatronic Vehicles Laboratory recently designed and tested a corner module for their urban electric vehicle. The corner module is capable of

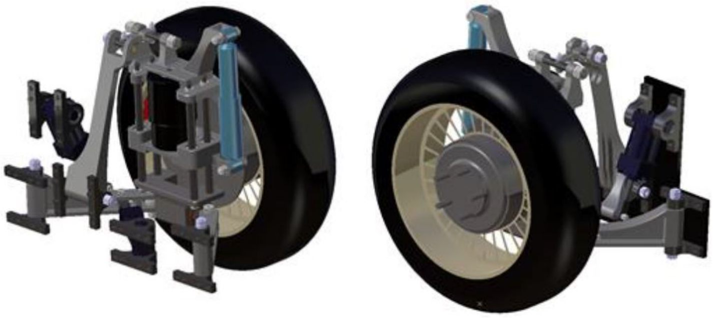

Figure 2.11: The University of Waterloo's corner module developped in the Mechatronic Vehicles Laboratory [30]

multiple X-by-wire functions including camber, steering, braking and driving. The steer and camber motions of the wheel are decoupled from the two linear actuators that control the motions. The steering system is composed of a planar four-bar linkage with a hydraulic cylinder while the camber system is made of a spatial four-bar linkge [30]. The use of the four-bar linkages allow the corner module to be packaged in a small space (fig. 2.11).

Chapter 3

Proposed Design

3.1 Product Design Specifications

A solution was required to increase the stability of an urban electric vehicle in the tad-pole configuration while minimizing the packaging required for the suspension, steering and powertrain systems. The work in this thesis solved the design problem for the same vehicle as the one specified by Rajaie [30]. The overall vehicle specifications affecting the corner module design are summarized in table 3.1. Some of these parameters are different than those reported in [30]. As time progressed on the project more accurate estimates of the vehicle parameters were available. The updated estimates are shown in table 3.1.

The product design specifications required that the proposed corner module achieve minimum steer and camber ranges as well as a target lateral wheel travel at -15° of camber. The camber range and target lateral wheel travel were specified to increase the stability of the vehicle. The minimum steer range was selected to be $\pm 20^\circ$. Conventional cars typically have steer ranges between $\pm 30^\circ$ and $\pm 43^\circ$ [17]. However, the urban vehicle under consideration would be capable of all-wheel steer because the same corner module would be used for each wheel. Therefore, $\pm 20^\circ$ was an acceptable minimum steer range.

Table 3.1: Estimated vehicle parameters

Description	**Value**	**Units**	**Symbol**
Total mass*	550	kg	m
CG height*	0.417	m	h
Front wheel to CG distance*	0.743	m	a
Rear wheel to CG distance*	1.057	m	b
Wheelbase	1.8	m	L
Cornering stiffness, front tire	250000	N/m	$C_{\alpha f}$
Cornering stiffness, rear tire	400000	N/m	$C_{\alpha r}$
Nominal track width	1.2	m	T
Ground clearance	0.15	m	d_g

*Parameter different from that reported in [30]

Targets were also placed on the fore/aft wheel travel induced by steering and on the steer induced by bump/roll. It was decided to minimize the longitudinal wheel travel caused by steering the wheel so that there would be less wear on the tire. The bump steer was limited to a maximum deviation of $\pm 0.4°$ from the steer angle at zero vertical wheel travel. The bump steer was limited to make the dynamics of the system more predictable during cornering and bump events.

Another purpose of the corner module was to maintain a reasonable level of ride comfort as compared to conventional cars while increasing the stability of the three-wheeled urban electric vehicle. The natural frequencies of the sprung and unsprung masses had to remain outside of 4 to 8 Hz as this is the frequency range that most severely affects the human body [19]. The wheel's natural frequency was targeted to be between 10 and 12 Hz, while the natural frequency of the vehicle body was targeted to be between 1 to 1.33 Hz.

The corner module also had to meet the constraints imposed by the overall vehicle design. Along with designing the corner module for the vehicle specified in table 3.1, it also had to fit in a packaging space available in the wheel well. This space was constrained a 630 mm length, 300 mm width and 630 mm height from the ground. The width of the packaging space was measured from the vehicle body to the inside edge of the tire when the wheel was in the 0° steer and 0° camber position at ride height. The corner module could only use two actuators due to packaging and cost constraints. Lastly, the corner module was constrained to use the wheel and motor assembly from EnerTrac Corp. Listed below is a summary of the product design specifications.

Summary of Product Design Specifications

- minimum of $\pm 20^\circ$ steer range
- minimum 0° to -15° camber range
- minimum of 10 cm of lateral wheel travel at -15° of camber
- minimize longitudinal wheel travel induced by steer
- maximum of $\pm 0.4^\circ$ bump steer
- target vehicle body natural frequency of 1 to 1.33 Hz
- target unsprung mass natural frequency of 10 to 12 Hz
- fit within a $630 \times 300 \times 630$ mm^3 box
- maximum of two actuators to control the steer and camber
- use the wheel and motor assembly from EnerTrac Corp.

3.2 Concept Generation and Evaluation

Concepts for the corner module were generated using the Grübler-Kutzbach mobility formula (eq. 3.1) for parallel mechanisms [21]. Equation 3.1 approximates the mobility for a

Table 3.2: Lower kinematic joints

Joint Type	**DOF**	**Symbol**	**Rotations**	**Translations**
Prismatic	1	P	0	1
Revolute	1	R	1	0
Universal	2	U	2	0
Spherical	3	S	3	0

parallel mechanism with l number of links and j number of joints. For spatial mechanisms, $\lambda = 6$. Each joint has f_i degrees of freedom and v is the number of redundant constraints.

$$M = \lambda(l - j - 1) + \Sigma_{i=1}^{j} f_i + v \tag{3.1}$$

The Grübler-Kutzbach formula was simplified by assuming that there were zero redundant constraints in the mechanism. To generate the first iteration of concepts, the geometry of the mechanism was ignored. The Grübler-Kutzbach mobility equation was used to determine what combination of joints and links would result in a parallel mechanism with three degrees of freedom. It should be noted that the Grübler-Kutzbach formula does not apply to all parallel mechanisms and further analysis was required to determine the feasibility of the mechanisms selected [11].

Joints with one to three degrees of freedom were considered for the concept generation. Equation 3.2 was used to determine all combinations of joints and links that would result in a mechanism with three degrees of freedom ($M = 3$) for steering, cambering and vertical travel.

$$3 = 6(l - j - 1) + j_1 + 2j_2 + 3j_3 \tag{3.2}$$

j_1 to j_3 represented the number of joints that had one degree of freedom to three degrees of freedom, respectively. Joints with more than three degrees of freedom were not considered as they would over-complicate the mechanism. A summary of the mechanisms that satisfy equation 3.2 are list in appendix A.1. Different parallel mechanism configurations were

Table 3.3: Final options for joint and link combinations

Option	**Joints**	**Links**	**1 DOF Joints**	**2 DOF Joints**	**3 DOF Joints**
a	8	7	4	1	3
b	8	7	3	3	2
c	8	7	2	5	1
d	9	8	6	0	3
e	9	8	5	2	2
f	9	8	3	6	0
g	10	8	4	1	5
h	10	8	3	3	4

generated depending on the quantity of links and joints (appendix A.1). Table 3.2 lists the different types of joints considered.

The options in table A.1 were reduced to 20 by considering the product design requirement for two linear actuators. Therefore, there had to be a minimum of two 1 DOF joints in the mechanism. Furthermore, some joint and link combinations from table A.1 could not be configured into a viable solution and were also eliminated. Such configurations had five joints and five links. Concepts were further eliminated using figure A.1. Due to the two linear actuator requirement, configurations that did not have two sets of two links in series were eliminated. Therefore, the remaining options for the parallel mechanism were: 7 links and 8 joints, 8 links and 8 joints, 8 links and 9 joints, and 8 links and 10 joints. The 8 links and 8 joints configuration was eliminated because the combination of the configuration options and the joint set would not allow the moving platform (or wheel) to undergo bump motion. The remaining joint and link combination options are summarized in table 3.3. Option g was eliminated because it had more spherical joints than limbs. This would cause one of the degrees of freedom of the mechanism to be redundant and therefore option g would be a RPM-type mechanism. To simplify the active rotational degree of freedom of the mechanism (i.e. the rotation controlled by the spring/damper), the link that the spring/damper would mount to had to have a revolute joint connected to the base of the

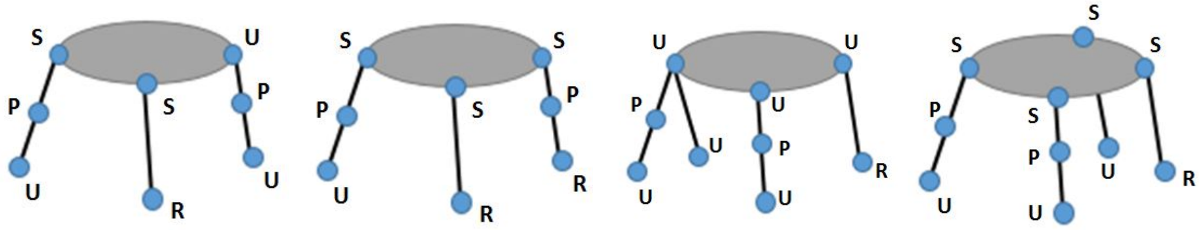

(a) Option b (b) Option c (c) Option f (d) Option h

Figure 3.1: Final four options for parallel mechanism configuration and joint selection. The grey oval represents the moving platform. The black lines are links and the blue circles are joints. The letter beside the joint specifies the joint type as per table 3.2

parallel mechanism. Therefore, option c was removed from the possible choices. Option d and e were eliminated because they did not have enough universal or spherical joints to decouple the suspension motion from the steer or camber motions. Therefore, option d and e were impossible to implement. The four remaining options are shown in figure 3.1. Of the final four options, option h was selected (fig. 3.1d) because it did not put the linear actuators into bending and it was less complex than option f (fig. 3.1c).

3.3 Final Solution

The final solution used two linear, prismatic actuators to control the two degrees of the freedom in the mechanism when the spring and damper was locked. The parallel mechanism is considered to have four limbs. The spring and damper controls the rotation of the revolute joint connecting the upper control arm to the vehicle body. Therefore, when the spring and damper is free to move, the mechanism has three degrees of freedom and can be controlled via two linear, prismatic actuators and one revolute actuator. These three actuators are considered the active joints in the parallel mechanism. The mechanism has seven passive joints and three active joints. The passive joints of the conceptual mechanism consisted of three universal joints and three spherical joints. To simplify the

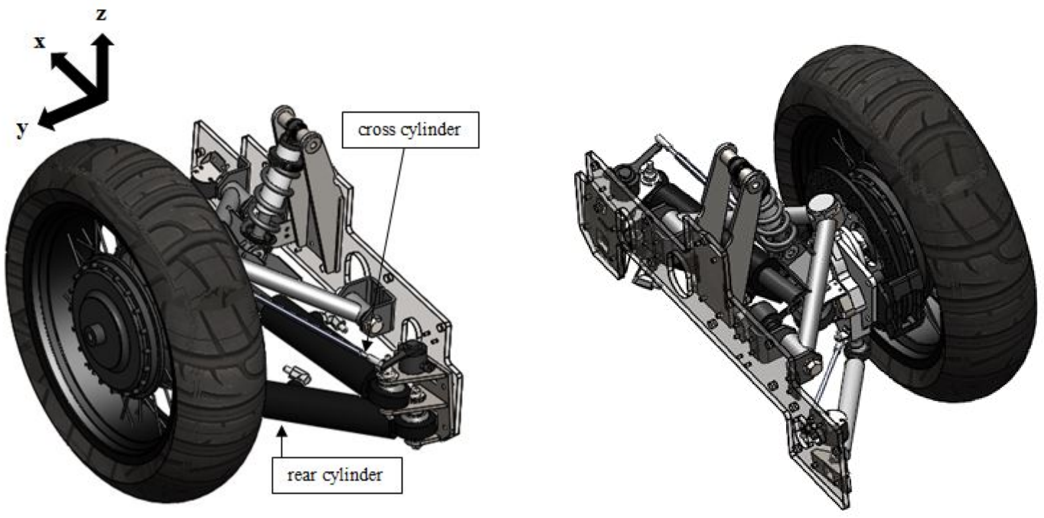

(a) UCM with coordinate system (b) UCM viewed from inside the vehicle

Figure 3.2: Isometric view of the UCM

construction of the mechanism and prevent unintentional lock-up, redundancy was added to the mechanism. This was done by replacing the universal joints with spherical joints. Figure 3.2 shows two views of the final solution for the corner module. The corner module was titled the UCM because it can be installed on any wheel of an urban electric vehicle. The wheel is the moving platform and the large grey plate (back plate) is the base of the parallel mechanism. The corner module was able to satisfy the product design specifications by optimizing the joint locations at 0° steer and 0° camber of the wheel with respect to the base and with the spring/damper at ride height length. These points are considered the hard points of the corner module.

Chapter 4

Design Optimization

4.1 Inverse Kinematic Model used in Optimization

Before the hard points of the corner module could be optimized, a mathematical model describing the behaviour of the system was required. The model was generated by using the loop closure method described in section 2.1.2. The model only considered cases when the shock absorber was in the ride height position (the position in which the shock absorber had a length of 236.86 mm). This caused the outboard spherical joint on the upper control arm, $\boldsymbol{S}$, to be fixed with respect to the vehicle body. Figure 4.1 shows a schematic of the system modelled for the optimization algorithm. The joints labelled $\boldsymbol{S}$, $\boldsymbol{AO}$, $\boldsymbol{AI}$, $\boldsymbol{BO}$, $\boldsymbol{BI}$, $\boldsymbol{CO}$ and $\boldsymbol{CI}$ were are spherical joints. Limbs A and C have prismatic joints between the spherical joints, whereas limb B has a constant length.

The inverse kinematic problem was solved as opposed to the forward kinematic problem because it reduced the number of equations required to provide a solution. Tait-Bryan angles were used to describe the rotation of the platform's frame of reference with respect to the fixed frame of reference. A steer rotation followed by a camber rotation followed by a wheel spin rotation was the desired rotation sequence. Therefore, the Tait-Bryan angle sequence used was z-x'-y" (eq. 4.1). Equations 4.2 to 4.4 are the rotation matrices for each

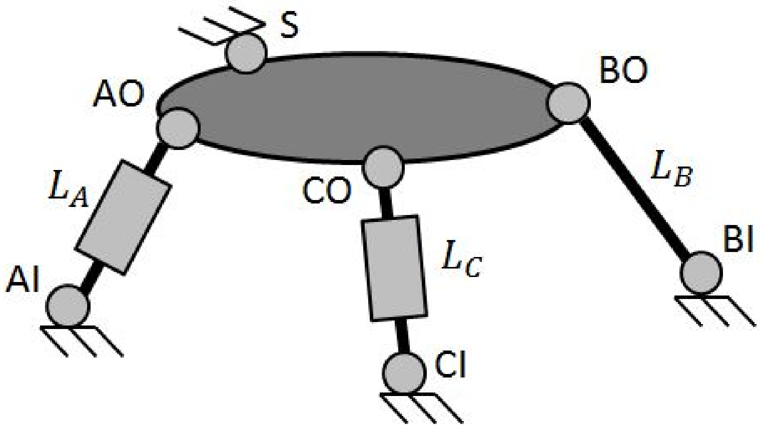

Figure 4.1: Schematic of mathematical model used in hard point optimization

angle. The wheel spin angle, β, was one of the four unknowns in the system of equations. Whereas the steer, δ, and camber, γ, angles were the inputs because inverse kinematics was used. The inverse kinematic problem was solved using two vector equations (eq. 4.5 & 4.6) [35]. The location of the outboard spherical joint of the fixed-length link at 0° steer and 0° camber, $\boldsymbol{BO_i}$, was known. The Cartesian components of the instantaneous location of the outboard spherical joint of the fixed-length link, $\boldsymbol{BO}$, were the other three unknowns.

$$\boldsymbol{R} = \boldsymbol{R_z}\boldsymbol{R_x}\boldsymbol{R_y} \tag{4.1}$$

$$\boldsymbol{R_z} = \begin{bmatrix} \cos(\delta) & -\sin(\delta) & 0 \\ \sin(\delta) & \cos(\delta) & 0 \\ 0 & 0 & 1 \end{bmatrix} \tag{4.2}$$

$$\boldsymbol{R_x} = \begin{bmatrix} 1 & 0 & 0 \\ 0 & \cos(\gamma) & -\sin(\gamma) \\ 0 & \sin(\gamma) & \cos(\gamma) \end{bmatrix} \tag{4.3}$$

$$\boldsymbol{R_y} = \begin{bmatrix} \cos(\beta) & 0 & \sin(\beta) \\ 0 & 1 & 0 \\ -\sin(\beta) & 0 & \cos(\beta) \end{bmatrix} \tag{4.4}$$

$$\boldsymbol{BO} - \boldsymbol{S} = \boldsymbol{R}(\boldsymbol{BO_i} - \boldsymbol{S}) \tag{4.5}$$

$$\|\boldsymbol{BO} - \boldsymbol{BI}\|_2^2 = \|\boldsymbol{BO_i} - \boldsymbol{BI}\|_2^2 \tag{4.6}$$

Equations 4.5 and 4.6 created a nonlinear system of equations given the four unknowns. Therefore, the nonlinear solver, fsolve, from Matlab was chosen because it allowed the optimal value and the optimal solution to be vectors. The trust-region algorithm was selected because it was the quickest to solve of the three algorithm options. The trust-region algorithm took 73% less time than the trust-region-dogleg algorithm and 79% less time than the Levenberg-Marquardt algorithm. By using Matlab's nonlinear solver to solve the system of equations, the cylinder positions and lengths could be determined for all steer and camber positions within the mechanism's workspace.

Once the unknowns, $\boldsymbol{BO}$ and β, were found for a given camber angle and steer angle, all other points on the wheel assembly could be determined. Therefore, the location of the rear and cross cylinders' outboard spherical joints could be determined (eq. 4.7 & 4.8). The lengths of the rear and cross cylinders were then found using the inboard and outboard joint locations for each camber and steer instance (eq. 4.9 & 4.10). The Matlab code for the inverse kinematic model is shown in appendix B.2.

$$\boldsymbol{AO} = \boldsymbol{R}(\boldsymbol{AO_i} - \boldsymbol{S}) + \boldsymbol{S} \tag{4.7}$$

$$\boldsymbol{CO} = \boldsymbol{R}(\boldsymbol{CO_i} - \boldsymbol{S}) + \boldsymbol{S} \tag{4.8}$$

$$l_A = \|\boldsymbol{AO} - \boldsymbol{AI}\|_2 \tag{4.9}$$

$$l_C = \|\boldsymbol{CO} - \boldsymbol{CI}\|_2 \tag{4.10}$$

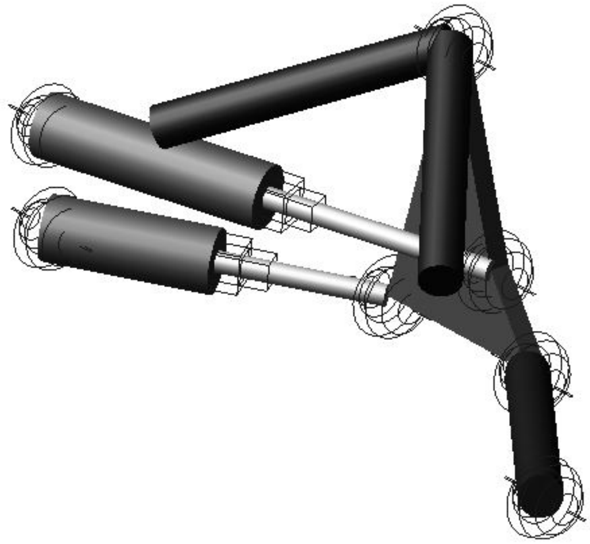

Figure 4.2: Isometric view of the Adams/View model.

4.2 Model Validation using Adams/View

Before the genetic algorithm could run, it was important to ensure that the Matlab model accurately represented the corner module. Therefore, Adams/View was used to validate the model described in section 4.1. One configuration that could be generated by the genetic algorithm was selected. The same inputs ($\boldsymbol{AI}$, $\boldsymbol{BI}$, $\boldsymbol{CI}$, $\boldsymbol{S}$, $\boldsymbol{AO_i}$, $\boldsymbol{BO_i}$ and $\boldsymbol{CO_i}$) were used in both of the Matlab and Adams/View models. Figure 4.2 shows an isometric view of the configuration in Adams/View. At 0° camber, the Matlab model gave the exact same results as the Adams/View model. The lengths of the rear and cross cylinders for both of the Matlab and Adams/View models are shown in figure 4.3. As it is shown, the Matlab model gave the same results as the Adams/View model, therefore, the Matlab model was theoretically correct.

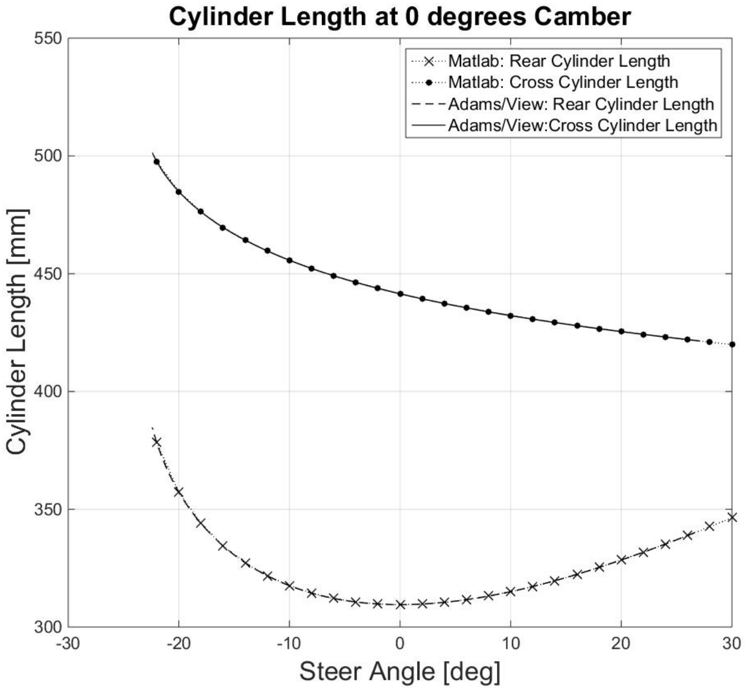

Figure 4.3: Matlab model cylinder lengths as compared with Adams/View model cylinder lengths.

4.3 Genetic Algorithm

Matlab's genetic algorithm was used to optimize the corner module's hard points. A genetic algorithm was chosen due to the nonlinearity of the objective function and the constraints. The use of a genetic algorithm was also prompted by the fact that the problem was multi-modal with multiple objectives to be minimized [35]. The search space was also discrete due to the cylinder constraints. The Matlab code for the genetic algorithm is shown in appendix B.1.

The hard points to be optimized included the locations of the inboard spherical joints and the locations of the outboard spherical joints at 0° steer and 0° camber. In total, that consisted of 7 joints and three components for each joint. Therefore, there were 21 variables to be optimized. The model was simplified to reduce the computation time. The placement of the cross cylinder did not impact the motion of the wheel during steer and camber rotations at constant spring and damper length. The placement of the cross cylinder impacted the forces in the links and bump steer. However, neither the link forces or the bump steer implications were accounted for in the optimization. Therefore, the initial locations of the inboard and outboard cross cylinder joints were removed from the number of variables to be optimized.

The location of the y-component of the inboard joints was selected to be equal for all inboard joints and at the furthest possible distance from the wheel within the packaging space. The y-component location was -260 mm from the inside edge of the wheel so that the corner module could fit in a longitudinal spacing of 630 mm. The z-component of the inboard rear cylinder joint was set to be equal to the z-component of the inboard fixed-length link joint to simplify the bump and roll motions of the corner module. After the simplifications, the optimization program had 12 variables to be optimized.

4.3.1 Objectives

The objectives in the genetic algorithm reflected the requirements specified in section 3.1. The first objective was to obtain a lateral contact patch displacement, ε_y, of 100 mm at a steer angle of 0° and a camber angle of 15°. This objective would allow the wheel to camber so that the center of gravity was lowered and the track width was increased sufficiently to increase the stability of the vehicle.

The second and third objectives were implemented to limit the amount of wheel movement throughout the steer range at 0° camber. This objective was implemented to reduce the wear on the tires from steering and reduce the size of the wheel well. The maximum and minimum longitudinal contact patch displacements, ε_x, at 0° camber were minimized. The minimum longitudinal contact patch displacement was included in the objective function because the longitudinal displacement was 0 mm at 0° steer and 0° camber. Therefore, a negative displacement would occur for negative steer angles.

Absolute brackets were used for all objectives to prevent individual objective terms from reducing the objective function to zero. The first objective was scaled by a factor of two so that it's magnitude would be similar to that of the second and third objectives added together (eq. 4.11).

$$F_{obj} = 2|\varepsilon_y(0,15) - 100| + |\min(\varepsilon_x(\delta,0))| + |\max(\varepsilon_x(\delta,0))| \tag{4.11}$$

4.3.2 Constraints

Three main constraints from the product design specifications in section 3.1 were used in the genetic algorithm. The corner module had to fit in a $630 \times 300 \times 630$ mm^3 packaging space, use a maximum of two practically sized cylinders and integrate with the vehicle as specified in table 3.1. The optimization was performed on the front, left wheel with the fixed origin located at the wheel center projected onto the ground when the wheel was in the 0° steer and 0° camber position (fig. 4.4). The coordinate system of the fixed origin had the x-axis pointing to the front of the vehicle, the y-axis pointing away from the vehicle and the z-axis pointing away from the ground. The fixed coordinate system was crucial in determining the upper and lower bounds on the optimization variables (table 4.1).

Due to the width of the EnerTrac wheel and the packaging of the rotor and caliper, the closest any outboard joints could be in the y-direction was 150 mm from the origin. Therefore, the upper limit of the y-component for all outboard joints was -150 mm. To reduce computation time, the lower limit on the y-component for all outboard joints was set to -180 mm. It would be unrealistic for the lower limit to be any less than -180 mm as this would leave a lateral space less than 150 mm for the cylinders and upper control arm.

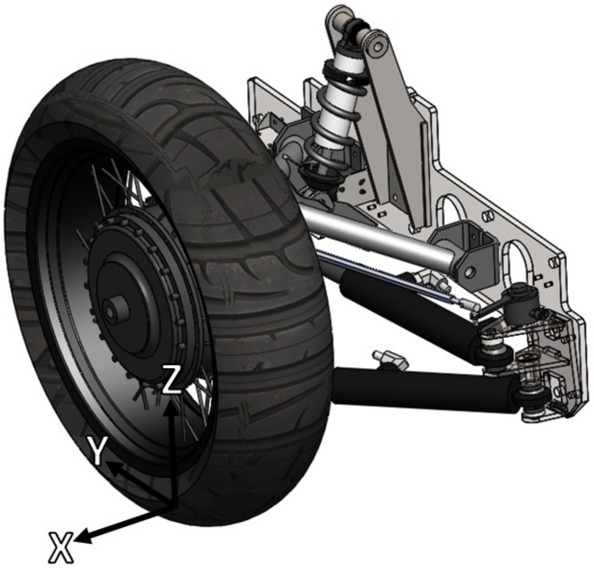

Figure 4.4: Location of origin and orientation of coordinate system used in optimization

Table 4.1: Upper and lower limits for free variables [35]

Joint Location	**Symbol**	**Lower Limit (mm)**	**Upper Limit (mm)**
Inboard rear cylinder	AI_x	-280	-100
	AI_z	170	315
Inboard fixed-length link	BI_x	100	310
Outboard UCA	S_x	-150	20
	S_y	-180	-150
	S_z	370	450
Outboard rear cylinder	AO_{ix}	-250	0
	AO_{iy}	-180	-150
	AO_{iz}	160	270
Outboard fixed-length link	BO_{ix}	0	250
	BO_{iy}	-180	-150
	BO_{iz}	160	270

Also, earlier executions of the genetic algorithm showed that the optimal solution would consistently converge to the upper limit for the y-component of all outboard joints.

The lower and upper limits for the z-components for the outboard fixed-length link and cylinder joints were set to prevent interference with the ground when the wheel was cambered and to maintain leverage on the wheel assembly, respectively. The lower and upper limits on the x-components on the outboard fixed-length link and outboard cylinder joints were selected to prevent interference of the two joints and to keep the joints at reasonable locations to be mounted to the upright.

The lower and upper limits on the z-component of the outboard upper control arm joint were selected to maintain leverage on the wheel assembly and to keep the joint in an area where it could be connected to the upright, respectively. The range of the x-component for the outboard upper control arm joint in previous iterations was much larger than that shown in table 4.1. However, the optimal solution for this component would consistently converge to a point within the range specified in table 4.1.

The x-components of the inboard joints had upper and lower limits to prevent interference with one another and to remain within the packaging space without interfering with the frame. The limits on the z-component of the cylinder were selected so that the inboard joints could be mounted on the frame at ride height and so that they would be higher than the outboard joints on the fixed-length link and cylinder. The latter requirement was implemented to achieve a reasonable camber-by-roll behaviour in the vehicle which is later explained in section 5.1.

Inequality constraints were also used to influence the camber-by-roll behaviour, the link lengths and joint interference. Equations 4.12 and 4.13 ensured that the x-components of the outboard joints of the spatial four-bar linkage (four-bar linkage formed by $\boldsymbol{BI}$, $\boldsymbol{BO}$, $\boldsymbol{AO}$ and $\boldsymbol{AI}$) are contained within the x-components of the inboard joints. Equation 4.14 prevents the longitudinal distance between the inboard joints from exceeding 400 mm.

Combined with equations 4.12 and 4.13, this inequality constraint also prevented the longitudinal distance between the outboard four-bar linkage joints from exceeding 400 mm. Equation 4.15 prevented the longitudinal distance between the outboard four-bar linkage joints from being less than 150 mm. This inequality constraint was implemented to prevent joint interference. Equations 4.16 and 4.17 placed upper and lower limits on the vertical distance between the inboard and outboard joints on the rear cylinder. This was used to influence the passive camber-by-roll behaviour of the vehicle.

$$AI_x - AO_{ix} \leq 0 \tag{4.12}$$

$$BO_{ix} - BI_x \leq 0 \tag{4.13}$$

$$BO_{ix} - AO_{ix} \leq 400 \tag{4.14}$$

$$AO_{ix} - BO_{ix} \leq -150 \tag{4.15}$$

$$AO_{iz} - AI_z \leq -40 \tag{4.16}$$

$$AI_z - AO_{iz} \leq 100 \tag{4.17}$$

The final constraints considered in the optimization program were the constraints on the cylinder stroke and compressed length. It was undesired to achieve an optimal solution for the corner module that had cylinders which were not readily available from hydraulic cylinder suppliers. Therefore, four existing hydraulic cylinders with specified stroke and compressed length were considered in the optimization program (table 4.2).

Table 4.2: Four cylinders considered in the optimization program [35]

Hydraulic Cylinder	1	2	3	4
Stroke (mm)	75	100	126	152
Compressed Length (mm)	290	315	323	343
Extended Length (mm)	365	415	449	495

These constraints were discrete so they were implemented in the fitness function instead of in the non-linear constraints section. This greatly reduced the computation time of the genetic algorithm. The fitness function began by calculating the length of the rear cylinder in the initial position. It would then select a cylinder from table 4.2 based on which cylinder's mid-length was closest to the length of the rear cylinder in the initial position. Then the fitness function would calculate the outboard joint locations for all desired steer and camber positions. If a position had a rear cylinder length outside of the workspace of the chosen cylinder, this position data would be omitted from the final calculation of the objective function. If the workspace of the mechanism was unable to achieve a minimum steer range of $-20°$ to $20°$ at $0°$ camber or a minimum camber range of $-15°$ to $0°$ at $0°$ steer, the objective function would be heavily penalized.

4.4 Optimization Results

The optimization program successfully found an optimal solution to the problem. It is not certain whether the solution was a local or global optimal solution. However, the solution reasonably minimized the objective function while meeting all of the constraints. Also, the optimization program was executed multiple times without changing any parameters to determine if it would converge to the same solution. The program would consistently converge to approximately the same points within a few millimeters. The optimization program was also run with varying boundary limits. Certain points, such as the outboard link and rear cylinder joints, would consistently converge to the maximum boundary limit.

Some of the following figures in this chapter include the cross cylinder length data. These figures were calculated after the location of the cross cylinder was selected. This selection process will be explained in section 5.2.

Figure 4.5 shows the lengths of the cross cylinder and rear cylinder for every camber

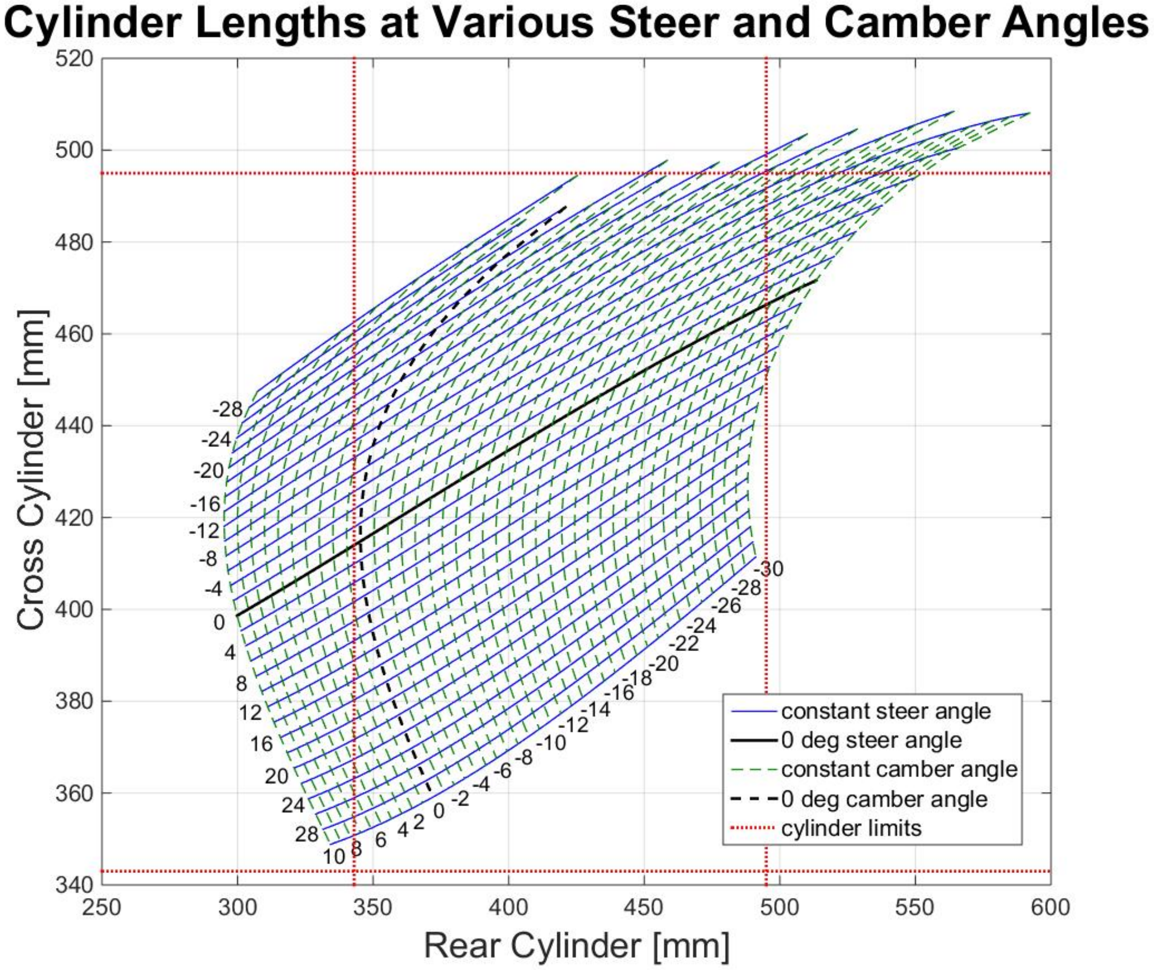
Cylinder Lengths at Various Steer and Camber Angles

Figure 4.5: Map of input workspace.

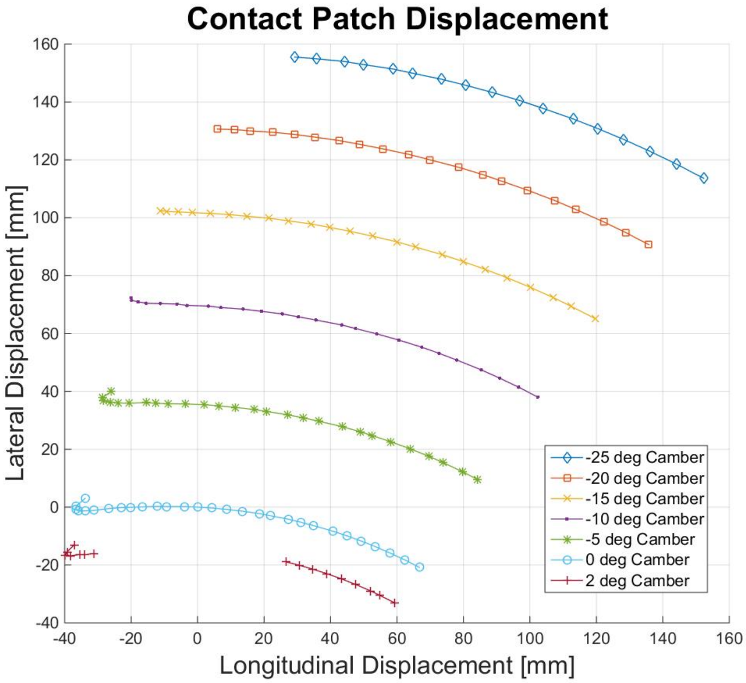

Figure 4.6: Displacement of theoretical contact patch with respect to its nominal position at 0° steer and 0° camber.

and steer position. It also indicates the workspace of the mechanism as limited by the hydraulic cylinders. The workspace exists within the box formed by the upper and lower limit lines. Figure 4.5 only shows the wheel positions ranging from $-30°$ to $30°$ steer and $-30°$ to $10°$ camber. From the figure, it is apparent that the wheel could achieve more steer and camber, however, at these positions, component interference occurs. At certain positions of less than $-14°$ steer and less than $2°$ camber, the non-linear solver could not find a solution within the tolerance limit. Fortunately, the majority of these positions are outside of the workspace.

The contact patch displacement at ground level ($\varepsilon_z = 0$) is shown in figure 4.6. A section of the curve at 2° camber is missing because it is outside of the cylinder workspace.

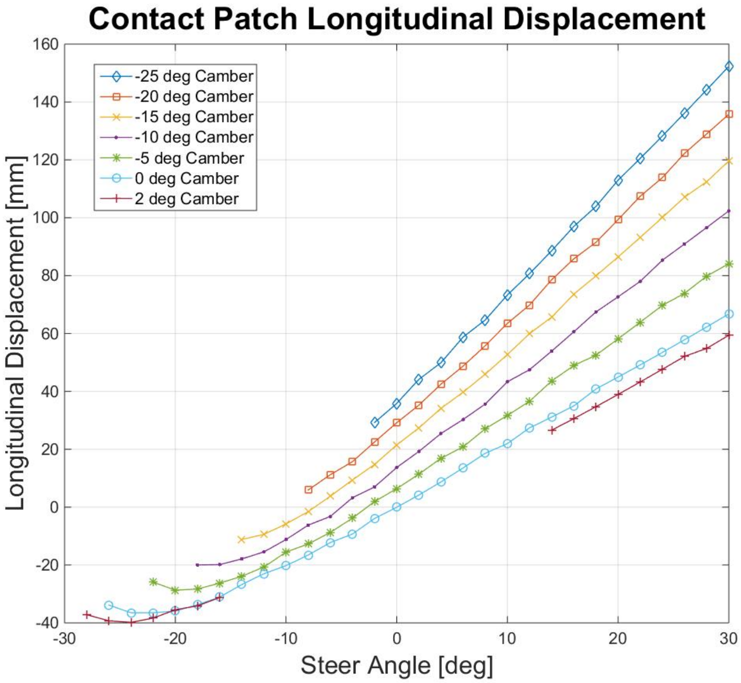

Figure 4.7: Longitudinal displacement of the contact patch plotted against steer angle for various constant camber orientations.

The rear cylinder's compressed length limited the mechanism's ability to achieve certain positive camber positions at various steer angles. From figure 4.6, it is apparent that the optimal solution achieved the first objective. At −15° camber and 0° steer, the wheel's contact patch had a lateral displacement of 101.5 mm. Also, the steer range was greater than the specified minimum. At 0° camber, the wheel was able to steer −26° to 30°. The camber range was also greater than the specified minimum. At 0° steer, the wheel could achieve −30° to 0° camber.

Figures 4.6 and 4.7 are approximations of the location of the contact patch's center point. This approximation assumed no tire deflection. The wheel was approximated as a disc drawn on the center plane of the wheel and centred about the wheel center. The disc

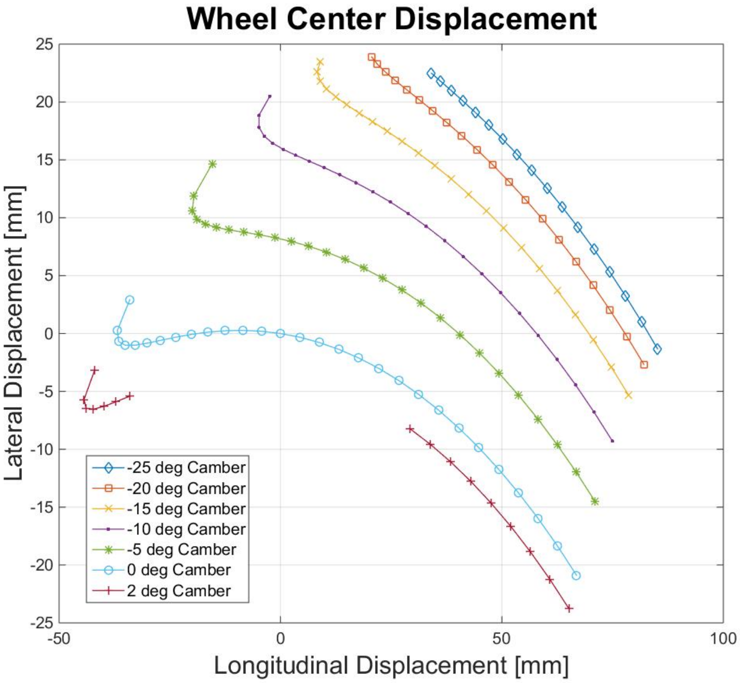

Figure 4.8: Displacement of the wheel center with respect to its nominal position at 0° steer and 0° camber.

had a diameter of 630 mm which was the same as the maximum diameter of the wheel. The point of contact between the wheel and the ground was assumed to always be the lowest point on the disc. The disc approximation was necessary due to the resulting wheel spin, β. A constant vector in the rotated wheel's coordinate system could not be used due to the wheel spin.

The longitudinal displacement of the contact patch is plotted against the steer angle in figure 4.7. This graph indicates that the optimal solution obtained a minimum longitudinal displacement of approximately 80 mm between $-20°$ and $20°$ steer at $0°$ camber. Figure 4.7 was plotted using the disc approximation. Figure 4.8 validates the disc approximation because it allows shows that at $0°$ camber the longitudinal displacement of approximately

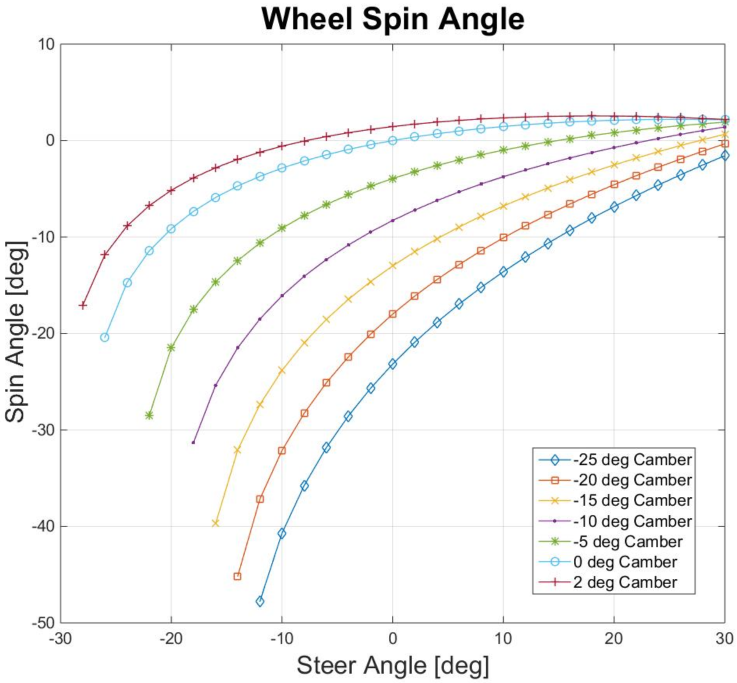

Figure 4.9: Wheel spin angle, β, for various camber and steer angles.

80 mm between −20° and 20° steer. The longitudinal and lateral displacement of the wheel center projected onto the ground is shown in figure 4.8. The plots of the wheel center and contact patch were exactly the same at 0° camber, therefore, the disc calculation was correct.

The wheel spin angle is shown in figure 4.9 for various positions of steer and camber within the workspace. This is the third rotation angle in the Tait-Bryan intrinsic rotations used to define the orientation of the wheel. The Tait-Bryan rotation sequence used was the z-x'-y" sequence. Therefore, the wheel spin angle was the rotation about the y"-axis. The wheel spin angle grew larger when the wheel camber was increased. This occurred because, in order to increase camber, the fixed-length link must rotate away from the vehicle body. This motion combined with the fixed outboard spherical joint on the upper control arm

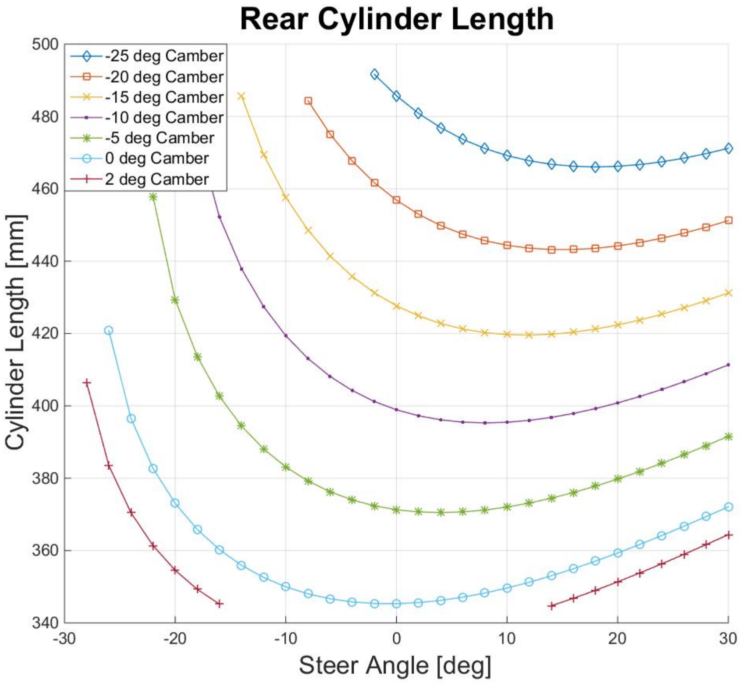

Figure 4.10: Rear cylinder length for various camber and steer angles.

generated an increase in spin angle. Larger magnitudes of wheel spin angles also occurred for negative steer angles. This was caused by the fixed-length link rotating away from the vehicle body and by the rear cylinder pushing the other side of the wheel away from the vehicle body which added to the spin rotation.

The rear cylinder length for various steer and camber positions is shown in figure 4.10. The rear cylinder could achieve all positions for negative camber at positive steer angles. However, between $-16°$ and $14°$, the compressed length of the rear cylinder limited the wheel's ability to achieve $2°$ of camber. The extended length of the rear cylinder limited the steering of the wheel at negative camber angles. After $-26°$ steer and $0°$ camber and after $-28°$ steer and $2°$ camber, the non-linear solver was unable to obtain a solution for lower steer angles.

4.5 Singularity Analysis

A singularity analysis was performed on the final solution of the optimization to determine if the mechanism had any of the singularity types mentioned in subsection 2.1.2 that existed in its workspace. Multiple Jacobian matrices were determined using the methods proposed by Taghirad and Zlatonov [34][40]. The singularity analysis was performed symbolically to obtain the global rank of the Jacobian matrices, and for each instance determined by both the inverse and forward kinematic problems to obtain the instantaneous rank of the Jacobian matrices. The inverse kinematic model was previously explained in section 4.1. The forward kinematic model of the corner module is explained below.

4.5.1 Forward Kinematic Model

The forward kinematic model required a greater number of equations than the inverse kinematic model because there were nine unknowns in the forward kinematic model whereas there were only four unknowns in the inverse kinematic model. The unknowns in the forward kinematic model included the steer angle, camber angle, spin angle, and the normalized y- and z-components for the outboard cylinder and link joints (δ, γ, β, $\frac{AO_y}{l_A}$, $\frac{AO_z}{l_A}$, $\frac{BO_y}{l_B}$, $\frac{BO_z}{l_B}$, $\frac{CO_y}{l_C}$ and $\frac{CO_z}{l_C}$). The normalized x-components of the outboard cylinder and link joints were already known due to the mechanism geometry when the lengths of the cylinders were given. Cosine law was used to determine the angle between the cylinder or link and the constant vector from the inboard joint of the cylinder or link to the outboard upper control arm joint, $\boldsymbol{S}$ (eq. 4.18-4.20). Then, the normalized x-components of the outboard cylinder and link joints was determined using the definition of the dot product (eq. 4.21-4.23).

$$\cos\theta_A = \frac{l_A^2 + \|\boldsymbol{S} - \boldsymbol{AI}\|_2^2 - \|\boldsymbol{S} - \boldsymbol{AO_i}\|_2^2}{2l_A\|\boldsymbol{S} - \boldsymbol{AI}\|_2} \tag{4.18}$$

$$\cos\theta_B = \frac{l_B^2 + \|\boldsymbol{S} - \boldsymbol{BI}\|_2^2 - \|\boldsymbol{S} - \boldsymbol{BO_i}\|_2^2}{2l_B\|\boldsymbol{S} - \boldsymbol{BI}\|_2} \tag{4.19}$$

$$\cos\theta_C = \frac{l_C^2 + \|\boldsymbol{S} - \boldsymbol{CI}\|_2^2 - \|\boldsymbol{S} - \boldsymbol{CO_i}\|_2^2}{2l_C\|\boldsymbol{S} - \boldsymbol{CI}\|_2} \tag{4.20}$$

$$AO_x = \frac{\|\boldsymbol{S} - \boldsymbol{AI}\|_2 \cos\theta_A - (S_y - AI_y)AO_y - (S_z - AI_z)AO_z}{S_x - AI_x} \tag{4.21}$$

$$BO_x = \frac{\|\boldsymbol{S} - \boldsymbol{BI}\|_2 \cos\theta_B - (S_y - BI_y)BO_y - (S_z - BI_z)BO_z}{S_x - BI_x} \tag{4.22}$$

$$CO_x = \frac{\|\boldsymbol{S} - \boldsymbol{CI}\|_2 \cos\theta_C - (S_y - CI_y)CO_y - (S_z - CI_z)CO_z}{S_x - CI_x} \tag{4.23}$$

The system of non-linear equations was generated by using the loop closure method. Four independent closed vector loops were formed from limbs A, B, C and S (eq. 4.24-4.27) where vector $\boldsymbol{P}$ points to a location on the moving platform from the fixed origin. These limbs were composed of the rear cylinder, cross cylinder, fixed-length link and the outboard upper control arm joint, respectively.

$$\boldsymbol{AI} + l_A\hat{\boldsymbol{a}} = \boldsymbol{P} + \boldsymbol{R}(\boldsymbol{AO_i} - \boldsymbol{P}) \tag{4.24}$$

$$\boldsymbol{BI} + l_B\hat{\boldsymbol{b}} = \boldsymbol{P} + \boldsymbol{R}(\boldsymbol{BO_i} - \boldsymbol{P}) \tag{4.25}$$

$$\boldsymbol{CI} + l_C\hat{\boldsymbol{c}} = \boldsymbol{P} + \boldsymbol{R}(\boldsymbol{CO_i} - \boldsymbol{P}) \tag{4.26}$$

$$\boldsymbol{S} = \boldsymbol{P} + \boldsymbol{R}(\boldsymbol{S} - \boldsymbol{P}) \tag{4.27}$$

The four vector equations were reduced to three by substituting equation 4.27 into equations 4.24 to 4.26. Equations 4.28 to 4.30 depict the three vector loops formed by the link and cylinders with the outboard upper control arm joint. Matlab's non-linear least-squares solver, lsqnonlin, was used so that upper and lower bounds could be placed on the angles. The unknown y- and z-components were normalized since the lengths of the link and cylinders were known (eq. 4.31-4.33). This also reduced the search space for the non-linear least-squares solver (app. B.3).

$$\boldsymbol{AI} + l_A\hat{\boldsymbol{a}} = \boldsymbol{S} + \boldsymbol{R}(\boldsymbol{AO_i} - \boldsymbol{S}) \tag{4.28}$$

$$\boldsymbol{BI} + l_B\hat{\boldsymbol{b}} = \boldsymbol{S} + \boldsymbol{R}(\boldsymbol{BO_i} - \boldsymbol{S}) \tag{4.29}$$

$$\boldsymbol{CI} + l_C\hat{\boldsymbol{c}} = \boldsymbol{S} + \boldsymbol{R}(\boldsymbol{CO_i} - \boldsymbol{S}) \tag{4.30}$$

$$\hat{\boldsymbol{a}} = \begin{bmatrix} \frac{AO_x}{l_A} & \frac{AO_y}{l_A} & \frac{AO_z}{l_A} \end{bmatrix}^T \tag{4.31}$$

$$\hat{\boldsymbol{b}} = \begin{bmatrix} \frac{BO_x}{l_B} & \frac{BO_y}{l_B} & \frac{BO_z}{l_B} \end{bmatrix}^T \tag{4.32}$$

$$\hat{\boldsymbol{c}} = \begin{bmatrix} \frac{CO_x}{l_C} & \frac{CO_y}{l_C} & \frac{CO_z}{l_C} \end{bmatrix}^T \tag{4.33}$$

The non-linear least-squares solver successfully determined the unknown angles and normalized components. Figure 4.11 shows the steer and camber angles of the wheel

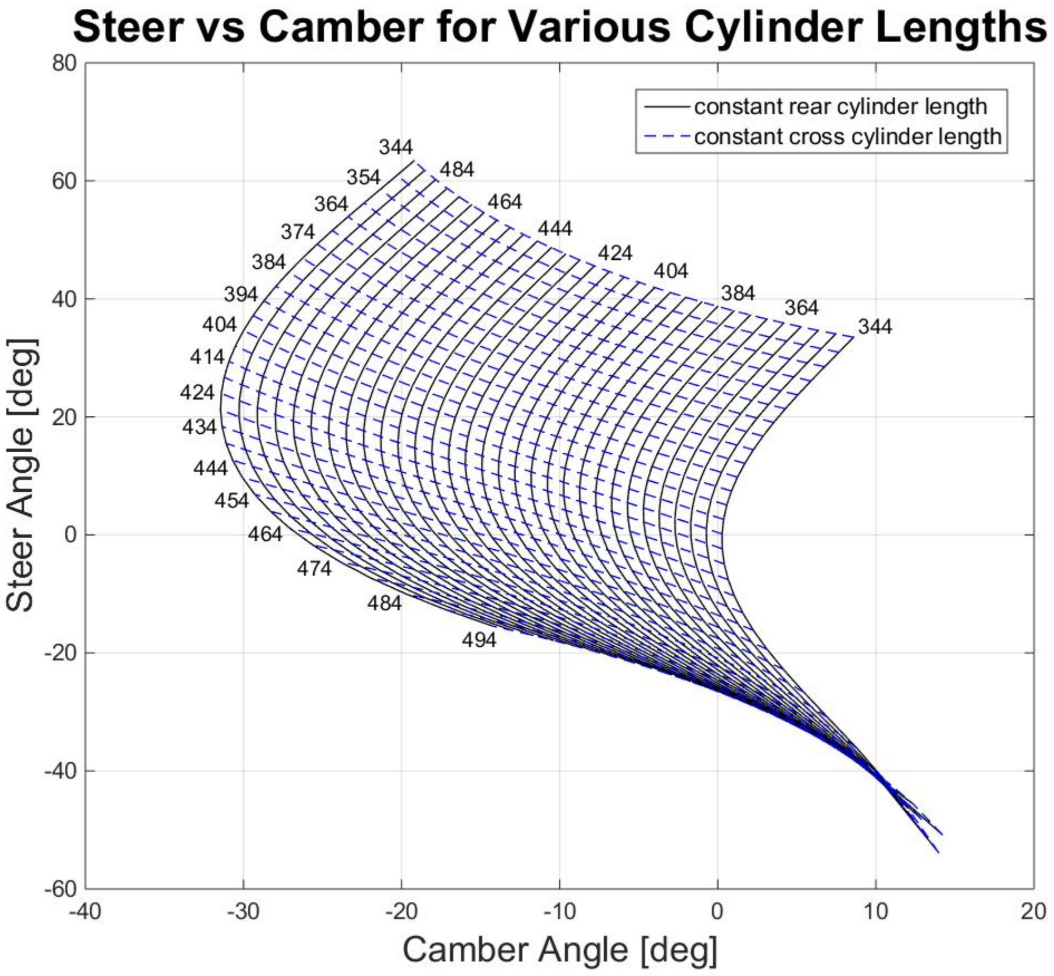

Figure 4.11: Steer and camber angles of the wheel at various rear and cross cylinder lengths.

given various rear and cross cylinder lengths. The results from the forward kinematic model agreed with the results from the inverse kinematic model. However, the forward kinematic model was able to solve more corner module configurations than the inverse kinematic model. Although, there were still some configurations that the non-linear solver was unable to determine.

4.5.2 Taghirad Method

The loop closure method has been used by many authors to determine the system of equations and subsequently find the Jacobian matrices [34][13][15][32]. However, Taghirad proposed finding the combined Jacobian matrix of a hydraulic shoulder by first finding the Jacobian matrix of the active joints and the Jacobian matrix of the passive joints.

To find the active Jacobian matrix, the time derivative was performed on the closed loop equations containing the active joints (eq. 4.24 & 4.26). This resulted in equations 4.34 and 4.40.

$$\boldsymbol{\hat{a}}\dot{l}_A + (\boldsymbol{\omega_A} \times \boldsymbol{\hat{a}})l_A = \boldsymbol{\dot{P}} + \boldsymbol{\omega} \times \boldsymbol{R}(\boldsymbol{AO_i} - \boldsymbol{P}) \tag{4.34}$$

$$\boldsymbol{\hat{c}}\dot{l}_C + (\boldsymbol{\omega_C} \times \boldsymbol{\hat{c}})l_C = \boldsymbol{\dot{P}} + \boldsymbol{\omega} \times \boldsymbol{R}(\boldsymbol{CO_i} - \boldsymbol{P}) \tag{4.35}$$

Equations 4.34 and 4.40 were multiplied by the dot product of the cylinder unit vectors, $\boldsymbol{\hat{a}}$ and $\boldsymbol{\hat{c}}$, respectively in order to eliminate the rotational velocity vectors of the rear and cross cylinders, $\boldsymbol{\omega_A}$ and $\boldsymbol{\omega_C}$. Equations 4.36 and 4.37 were rearranged and rewritten in matrix form to find the active Jacobian matrix (eq. 4.38).

$$\dot{l}_A = \boldsymbol{\hat{a}} \cdot \boldsymbol{\dot{P}} + \boldsymbol{\hat{a}} \cdot (\boldsymbol{\omega} \times \boldsymbol{R}(\boldsymbol{AO_i} - \boldsymbol{P})) \tag{4.36}$$

$$\dot{l}_C = \boldsymbol{\hat{c}} \cdot \boldsymbol{\dot{P}} + \boldsymbol{\hat{c}} \cdot (\boldsymbol{\omega} \times \boldsymbol{R}(\boldsymbol{CO_i} - \boldsymbol{P})) \tag{4.37}$$

$$\begin{bmatrix} \dot{l}_A \\ \dot{l}_C \end{bmatrix} = \begin{bmatrix} \boldsymbol{\hat{a}}^T & (\boldsymbol{R}(\boldsymbol{AO_i} - \boldsymbol{P}) \times \boldsymbol{\hat{a}})^T \\ \boldsymbol{\hat{c}}^T & (\boldsymbol{R}(\boldsymbol{CO_i} - \boldsymbol{P}) \times \boldsymbol{\hat{c}})^T \end{bmatrix} \begin{bmatrix} \boldsymbol{\dot{P}} \\ \boldsymbol{\omega} \end{bmatrix} \tag{4.38}$$

The passive Jacobian matrix was found by using equations 4.25 and 4.27. The time derivative was computed on the loop closure equations containing the fixed-length link and the outboard upper control arm joint (eq. 4.39 & 4.40).

$$(\boldsymbol{\omega_B} \times \hat{\boldsymbol{b}})l_B = \dot{\boldsymbol{P}} + \boldsymbol{\omega} \times \boldsymbol{R}(\boldsymbol{BO_i} - \boldsymbol{P}) \tag{4.39}$$

$$0 = \dot{\boldsymbol{P}} + \boldsymbol{\omega} \times \boldsymbol{R}(\boldsymbol{S} - \boldsymbol{P}) \tag{4.40}$$

The passive Jacobian matrix was the linear transformation from the degrees of freedom in the platform to the twist vector of the moving platform. In this case, the twist vector of the moving platform was calculated by multiplying the passive Jacobian matrix with the camber rate and the steer rate. Therefore, equations 4.39 and 4.40 must define the spin rate and the velocity of a point on the moving platform in terms of the steer rate and the camber rate. An expression for the the spin rate was found by multiplying the unit vector of the fixed-length link, $\hat{\boldsymbol{b}}$, with equation 4.39 and using the cross product distributive property and the triple product circular-shift property (4.41). The velocity components of a point on the moving platform were found by rearranging equation 4.40 (eq. 4.42). Equations 4.41 and 4.42 were rewritten in matrix form to create equation 4.46.

$$\omega_y = \frac{(\hat{\boldsymbol{b}} \times \boldsymbol{R}(\boldsymbol{S} - \boldsymbol{BO_i}))_x}{(\hat{\boldsymbol{b}} \times \boldsymbol{R}(\boldsymbol{S} - \boldsymbol{BO_i}))_y}\omega_x + \frac{(\hat{\boldsymbol{b}} \times \boldsymbol{R}(\boldsymbol{S} - \boldsymbol{BO_i}))_z}{(\hat{\boldsymbol{b}} \times \boldsymbol{R}(\boldsymbol{S} - \boldsymbol{BO_i}))_y}\omega_z \tag{4.41}$$

$$\dot{\boldsymbol{P}} = [\boldsymbol{R}(\boldsymbol{S} - \boldsymbol{P})]_\times \boldsymbol{\omega} \tag{4.42}$$

$$\boldsymbol{R} = \begin{bmatrix} \boldsymbol{r_1^T} & \boldsymbol{r_2^T} & \boldsymbol{r_3^T} \end{bmatrix}^T \tag{4.43}$$

$$C_{wx} = \frac{(\hat{\boldsymbol{b}} \times \boldsymbol{R}(\boldsymbol{S} - \boldsymbol{BO_i}))_x}{(\hat{\boldsymbol{b}} \times \boldsymbol{R}(\boldsymbol{S} - \boldsymbol{BO_i}))_y} \tag{4.44}$$

$$C_{wz} = \frac{(\hat{\boldsymbol{b}} \times \boldsymbol{R}(\boldsymbol{S} - \boldsymbol{BO_i}))_z}{(\hat{\boldsymbol{b}} \times \boldsymbol{R}(\boldsymbol{S} - \boldsymbol{BO_i}))_y} \tag{4.45}$$

$$\begin{bmatrix} \dot{\boldsymbol{P}} \\ \boldsymbol{\omega} \end{bmatrix} = \begin{bmatrix} -C_{wx}(\boldsymbol{r_3} \cdot (\boldsymbol{S} - \boldsymbol{P})) & \boldsymbol{r_2} \cdot (\boldsymbol{S} - \boldsymbol{P}) - C_{wz}(\boldsymbol{r_3} \cdot (\boldsymbol{S} - \boldsymbol{P})) \\ \boldsymbol{r_3} \cdot (\boldsymbol{S} - \boldsymbol{P}) & -\boldsymbol{r_1} \cdot (\boldsymbol{S} - \boldsymbol{P}) \\ C_{wx}(\boldsymbol{r_1} \cdot (\boldsymbol{S} - \boldsymbol{P})) - \boldsymbol{r_2} \cdot (\boldsymbol{S} - \boldsymbol{P}) & C_{wz}(\boldsymbol{r_1} \cdot (\boldsymbol{S} - \boldsymbol{P})) \\ 1 & 0 \\ C_{wx} & C_{wz} \\ 0 & 1 \end{bmatrix} \begin{bmatrix} \omega_x \\ \omega_z \end{bmatrix} \tag{4.46}$$

The active Jacobian matrix and the passive Jacobian matrix were reiterated in equations 4.47 and 4.48. The active Jacobian matrix was multiplied by the passive Jacobian matrix to find the combined Jacobian matrix which was a two-by-two matrix(eq. 4.49) [34]. When the rank of the combined Jacobian matrix was symbolically calculated, it was full rank with a rank of two. Using Taghirad's singularity calculation method, there were no combined singularities in the workspace as the rank of the combined Jacobian matrix was equal to two at every instance calculated using both the forward kinematic model and inverse kinematic model.

$$\boldsymbol{J_a} = \begin{bmatrix} \hat{\boldsymbol{a}}^T & (\boldsymbol{R}(\boldsymbol{AO_i} - \boldsymbol{P}) \times \hat{\boldsymbol{a}})^T \\ \hat{\boldsymbol{c}}^T & (\boldsymbol{R}(\boldsymbol{CO_i} - \boldsymbol{P}) \times \hat{\boldsymbol{c}})^T \end{bmatrix} \tag{4.47}$$

$$\boldsymbol{J_p} = \begin{bmatrix} -C_{wx}(\boldsymbol{r_3} \cdot (\boldsymbol{S} - \boldsymbol{P})) & \boldsymbol{r_2} \cdot (\boldsymbol{S} - \boldsymbol{P}) - C_{wz}(\boldsymbol{r_3} \cdot (\boldsymbol{S} - \boldsymbol{P})) \\ \boldsymbol{r_3} \cdot (\boldsymbol{S} - \boldsymbol{P}) & -\boldsymbol{r_1} \cdot (\boldsymbol{S} - \boldsymbol{P}) \\ C_{wx}(\boldsymbol{r_1} \cdot (\boldsymbol{S} - \boldsymbol{P})) - \boldsymbol{r_2} \cdot (\boldsymbol{S} - \boldsymbol{P}) & C_{wz}(\boldsymbol{r_1} \cdot (\boldsymbol{S} - \boldsymbol{P})) \\ 1 & 0 \\ C_{wx} & C_{wz} \\ 0 & 1 \end{bmatrix} \tag{4.48}$$

$$\boldsymbol{J} = \boldsymbol{J_a}\boldsymbol{J_p} \tag{4.49}$$

Taghirad defined the inverse Jacobian matrix and forward Jacobian matrix as equations 4.51 and 4.52, respectively [34]. The function, $\boldsymbol{f}$ (eq. 4.50), is the geometric system of equations rearranged from equations 4.24 to 4.27. From the system of equations, it is apparent that the inverse Jacobian matrix was a two-by-two identity matrix for all configurations in the workspace. Therefore, there were no inverse singularity configurations. Therefore, the forward Jacobian matrix was equal to the combined Jacobian matrix. Taghirad's method indicated that there were no inverse, forward or combined singularities in the workspace of the corner module. The Matlab code for the Taghirad method is shown in appendix B.4.1.

$$\boldsymbol{f}(\boldsymbol{L}, \boldsymbol{X}) = \boldsymbol{0} \tag{4.50}$$

$$\boldsymbol{J_i} = \frac{\partial \boldsymbol{f}}{\partial \boldsymbol{L}} \tag{4.51}$$

$$\boldsymbol{J_f} = \frac{\partial \boldsymbol{f}}{\partial \boldsymbol{X}} \tag{4.52}$$

4.5.3 Zlatonov Method

Zlatonov proposed a precise method to determine if any of the six singularities defined in section 2.1.2 existed within a non-redundant parallel mechanism's workspace [40]. This was done using the Jacobian matrix that related the output twist to the velocities of the active and passive joints in the mechanism (eq. 4.53).

$$\boldsymbol{J} \begin{bmatrix} \boldsymbol{\omega} & \dot{l}_A & \dot{l}_C & \boldsymbol{\omega_A} & \boldsymbol{\omega_B} & \boldsymbol{\omega_C} \end{bmatrix}^T = \boldsymbol{J} \begin{bmatrix} \dot{\boldsymbol{X}} \\ \dot{\boldsymbol{L}} \\ \boldsymbol{\Omega_p} \end{bmatrix} = \boldsymbol{0} \tag{4.53}$$

For the parallel mechanism considered in this thesis, the output twist, $\dot{\boldsymbol{X}}$, consisted of the camber rate, ω_x, steer rate, ω_z, and spin rate, ω_y. The velocity vector for the active joints, $\dot{\boldsymbol{L}}$, consisted of the rear and cross cylinders' extension and compression rates, $\dot{l}_A$ and $\dot{l}_C$. The velocity vector for the passive joints, $\boldsymbol{\Omega_p}$, included the inboard joint velocities from the link and cylinders, $\boldsymbol{\omega_A}$, $\boldsymbol{\omega_B}$ and $\boldsymbol{\omega_C}$. Because the inboard joints were spherical joints, they only had three rotational velocities. The outboard joint rotational velocities were equal to the rotational velocity of the moving platform and therefore, they did not need to be defined in the system of equations.

Zlatonov made the following proposition to determine which type of singularity existed in a parallel mechanism's workspace [40].

i) $q \in \text{RI} \Leftrightarrow \text{rank}(\boldsymbol{J_O}) < \text{rank}(\boldsymbol{J_p}) + n$

ii) $q \in \text{RO} \Leftrightarrow \text{rank}(\boldsymbol{J_I}) < \text{rank}(\boldsymbol{J_p}) + n$

iii) $q \in \text{RPM} \Leftrightarrow \text{rank}(\boldsymbol{J_p}) < N - n$

iv) $q \in \text{II} \Leftrightarrow \text{rank}(\boldsymbol{J_I}) < \text{rank}(\boldsymbol{J})$

v) $q \in \text{IO} \Leftrightarrow \text{rank}(\boldsymbol{J_O}) < \text{rank}(\boldsymbol{J})$

vi) $q \in \text{IIM} \Leftrightarrow \text{rank}(\boldsymbol{J}) < N$

$$\boldsymbol{J} = \begin{bmatrix} \boldsymbol{J_X} & \boldsymbol{J_a} & \boldsymbol{J_p} \end{bmatrix} \tag{4.54}$$

$$\boldsymbol{J_O} = \begin{bmatrix} \boldsymbol{J_a} & \boldsymbol{J_p} \end{bmatrix} \tag{4.55}$$

$$\boldsymbol{J_I} = \begin{bmatrix} \boldsymbol{J_X} & \boldsymbol{J_p} \end{bmatrix} \tag{4.56}$$

The Jacobian output matrix, $\boldsymbol{J_O}$, consisted of the active and passive Jacobian matrices, $\boldsymbol{J_a}$ and $\boldsymbol{J_p}$, respectively. The Jacobian input matrix, $\boldsymbol{J_I}$, consisted of the Jacobian matrices related to platform twist and the active joint velocities, $\boldsymbol{J_X}$ and $\boldsymbol{J_a}$, respectively. For the corner module, the mobility of the platform, n, was equal to two, and the total degrees of freedom for all joints considered in the calculation of the Jacobian, N, was 11.

The Zlatonov Jacobian matrix, $\boldsymbol{J}$, was determined using equations 4.28 to 4.30. By taking the time derivative of these equations resulted in equations 4.57 to 4.59.

$$\dot{l}_A\hat{\boldsymbol{a}} + l_A(\boldsymbol{\omega_A} \times \hat{\boldsymbol{a}}) = \boldsymbol{\omega} \times \boldsymbol{R}(\boldsymbol{AO_i} - \boldsymbol{S}) \tag{4.57}$$

$$l_B(\boldsymbol{\omega_B} \times \hat{\boldsymbol{b}}) = \boldsymbol{\omega} \times \boldsymbol{R}(\boldsymbol{BO_i} - \boldsymbol{S}) \tag{4.58}$$

$$\dot{l}_C\hat{\boldsymbol{c}} + l_C(\boldsymbol{\omega_C} \times \hat{\boldsymbol{c}}) = \boldsymbol{\omega} \times \boldsymbol{R}(\boldsymbol{CO_i} - \boldsymbol{S}) \tag{4.59}$$

However, these three vector equations would only result in nine equations, and a minimum of 11 independent equations were required to determine the 11 joint velocities. Therefore, a minimum of two additional independent equations were required. The time derivative of the vector loop including the rear and cross cylinders provided three additional equations, however, only two equations were independent from the system of equations (eq. 4.61).

$$\boldsymbol{AI} + l_A\hat{\boldsymbol{a}} = \boldsymbol{R}(\boldsymbol{AO_i} - \boldsymbol{CO_i}) + l_C\hat{\boldsymbol{c}} + \boldsymbol{CI} \tag{4.60}$$

$$\dot{l}_A\hat{\boldsymbol{a}} + l_A(\boldsymbol{\omega_A} \times \hat{\boldsymbol{a}}) = \boldsymbol{\omega} \times (\boldsymbol{R}(\boldsymbol{AO_i} - \boldsymbol{CO_i})) + \dot{l}_C\hat{\boldsymbol{c}} + l_C(\boldsymbol{\omega_C} \times \hat{\boldsymbol{c}}) \tag{4.61}$$

Rearranging equations 4.57, 4.58, 4.59 and 4.61 into matrix form resulted in equation 4.62. Using Zlatonov's definitions, the Jacobian, input Jacobian, output Jacobian and passive Jacobian matrices are shown in equations 4.63, 4.64, 4.65 and 4.66, respectively.

$$\begin{bmatrix} -[\boldsymbol{R}(\boldsymbol{S} - \boldsymbol{AO_i})]_\times & \hat{\boldsymbol{a}} & \boldsymbol{0_{3\times1}} & -l_A[\hat{\boldsymbol{a}}]_\times & \boldsymbol{0_{3\times3}} & \boldsymbol{0_{3\times3}} \\ -[\boldsymbol{R}(\boldsymbol{S} - \boldsymbol{BO_i})]_\times & \boldsymbol{0_{3\times1}} & \boldsymbol{0_{3\times1}} & \boldsymbol{0_{3\times3}} & -l_B[\hat{\boldsymbol{b}}]_\times & \boldsymbol{0_{3\times3}} \\ -[\boldsymbol{R}(\boldsymbol{S} - \boldsymbol{CO_i})]_\times & \boldsymbol{0_{3\times1}} & \hat{\boldsymbol{c}} & \boldsymbol{0_{3\times3}} & \boldsymbol{0_{3\times3}} & -l_c[\hat{\boldsymbol{c}}]_\times \\ [\boldsymbol{R}(\boldsymbol{AO_i} - \boldsymbol{CO_i})]_\times & \hat{\boldsymbol{a}} & -\hat{\boldsymbol{c}} & -l_A[\hat{\boldsymbol{a}}]_\times & \boldsymbol{0_{3\times3}} & l_c[\hat{\boldsymbol{c}}]_\times \end{bmatrix} \begin{bmatrix} \boldsymbol{\omega} \\ \dot{l}_A \\ \dot{l}_C \\ \boldsymbol{\omega_A} \\ \boldsymbol{\omega_B} \\ \boldsymbol{\omega_C} \end{bmatrix} = \boldsymbol{0} \tag{4.62}$$

$$\boldsymbol{J} = \begin{bmatrix} -[\boldsymbol{R}(\boldsymbol{S} - \boldsymbol{AO_i})]_\times & \hat{\boldsymbol{a}} & \boldsymbol{0_{3\times1}} & -l_A[\hat{\boldsymbol{a}}]_\times & \boldsymbol{0_{3\times3}} & \boldsymbol{0_{3\times3}} \\ -[\boldsymbol{R}(\boldsymbol{S} - \boldsymbol{BO_i})]_\times & \boldsymbol{0_{3\times1}} & \boldsymbol{0_{3\times1}} & \boldsymbol{0_{3\times3}} & -l_B[\hat{\boldsymbol{b}}]_\times & \boldsymbol{0_{3\times3}} \\ -[\boldsymbol{R}(\boldsymbol{S} - \boldsymbol{CO_i})]_\times & \boldsymbol{0_{3\times1}} & \hat{\boldsymbol{c}} & \boldsymbol{0_{3\times3}} & \boldsymbol{0_{3\times3}} & -l_c[\hat{\boldsymbol{c}}]_\times \\ [\boldsymbol{R}(\boldsymbol{AO_i} - \boldsymbol{CO_i})]_\times & \hat{\boldsymbol{a}} & -\hat{\boldsymbol{c}} & -l_A[\hat{\boldsymbol{a}}]_\times & \boldsymbol{0_{3\times3}} & l_c[\hat{\boldsymbol{c}}]_\times \end{bmatrix} \tag{4.63}$$

$$\boldsymbol{J_I} = \begin{bmatrix} -[\boldsymbol{R}(\boldsymbol{S}-\boldsymbol{AO_i})]_\times & -l_A[\boldsymbol{\hat{a}}]_\times & \boldsymbol{0_{3\times3}} & \boldsymbol{0_{3\times3}} \\ -[\boldsymbol{R}(\boldsymbol{S}-\boldsymbol{BO_i})]_\times & \boldsymbol{0_{3\times3}} & -l_B[\boldsymbol{\hat{b}}]_\times & \boldsymbol{0_{3\times3}} \\ -[\boldsymbol{R}(\boldsymbol{S}-\boldsymbol{CO_i})]_\times & \boldsymbol{0_{3\times3}} & \boldsymbol{0_{3\times3}} & -l_c[\boldsymbol{\hat{c}}]_\times \\ [\boldsymbol{R}(\boldsymbol{AO_i}-\boldsymbol{CO_i})]_\times & -l_A[\boldsymbol{\hat{a}}]_\times & \boldsymbol{0_{3\times3}} & l_c[\boldsymbol{\hat{c}}]_\times \end{bmatrix} \tag{4.64}$$

$$\boldsymbol{J_O} = \begin{bmatrix} \boldsymbol{\hat{a}} & \boldsymbol{0_{3\times1}} & -l_A[\boldsymbol{\hat{a}}]_\times & \boldsymbol{0_{3\times3}} & \boldsymbol{0_{3\times3}} \\ \boldsymbol{0_{3\times1}} & \boldsymbol{0_{3\times1}} & \boldsymbol{0_{3\times3}} & -l_B[\boldsymbol{\hat{b}}]_\times & \boldsymbol{0_{3\times3}} \\ \boldsymbol{0_{3\times1}} & \boldsymbol{\hat{c}} & \boldsymbol{0_{3\times3}} & \boldsymbol{0_{3\times3}} & -l_c[\boldsymbol{\hat{c}}]_\times \\ \boldsymbol{\hat{a}} & -\boldsymbol{\hat{c}} & -l_A[\boldsymbol{\hat{a}}]_\times & \boldsymbol{0_{3\times3}} & l_c[\boldsymbol{\hat{c}}]_\times \end{bmatrix} \tag{4.65}$$

$$\boldsymbol{J_p} = \begin{bmatrix} -l_A[\boldsymbol{\hat{a}}]_\times & \boldsymbol{0_{3\times3}} & \boldsymbol{0_{3\times3}} \\ \boldsymbol{0_{3\times3}} & -l_B[\boldsymbol{\hat{b}}]_\times & \boldsymbol{0_{3\times3}} \\ \boldsymbol{0_{3\times3}} & \boldsymbol{0_{3\times3}} & -l_c[\boldsymbol{\hat{c}}]_\times \\ -l_A[\boldsymbol{\hat{a}}]_\times & \boldsymbol{0_{3\times3}} & l_c[\boldsymbol{\hat{c}}]_\times \end{bmatrix} \tag{4.66}$$

Although the Jacobian matrix has a dimension of 12×14, the global rank of the Jacobian is 11 (the global ranks of the Jacobian matrices were calculated symbolically). A rank of 11 was expected as one of the equations in the vector equation 4.61 was not independent from other equations in the system. The input Jacobian matrix had a rank of nine and a dimension of 12×12. The output Jacobian matrix had a rank of eight and a dimension of 12×11. The passive Jacobian matrix had a rank of six and a dimension of 12×9. When the Jacobian matrices were determined for each configuration, all instantaneous Jacobian ranks were equal to their respective global Jacobian matrices. All of the Jacobian matrices were globally rank deficient, however, according to Zlatonov's proposition, only three types of singularities existed globally.

i) $q \in \text{RI} \Leftrightarrow \text{rank}(\boldsymbol{J_O}) = 8 < \text{rank}(\boldsymbol{J_p}) + n = 8$

ii) $q \in \text{RO} \Leftrightarrow \text{rank}(\boldsymbol{J_I}) = 9 < \text{rank}(\boldsymbol{J_p}) + n = 8$

iii) $q \in \text{RPM} \Leftrightarrow \text{rank}(\boldsymbol{J_p}) = 6 < N - n = 9$

iv) $q \in \mathrm{II} \Leftrightarrow \mathrm{rank}(\boldsymbol{J_I}) = 9 < \mathrm{rank}(\boldsymbol{J}) = 11$

v) $q \in \mathrm{IO} \Leftrightarrow \mathrm{rank}(\boldsymbol{J_O}) = 8 < \mathrm{rank}(\boldsymbol{J}) = 11$

vi) $q \in \mathrm{IIM} \Leftrightarrow \mathrm{rank}(\boldsymbol{J}) = 11 < N = 11$

According to Zlatonov's definition, RPM-type, II-type and IO-type singularities existed in the entire workspace of the corner module. This result was expected since redundancy was added to the mechanism to simplify the design and prevent configurations where the mechanism gained or lost a degree of freedom. The original mechanism that satisfied the Grübler-Kutzbach mobility equation had two prismatic joints, four spherical joints and three universal joints. However, the mechanism that the singularity analysis was performed on had two prismatic joints and seven spherical joints. Understandably, there would be three redundant passive motion in the mechanism. The redundant passive motion was one of the rotations in each of the cylinders and the fixed-length link. The rotation about the axis connecting the inboard and outboard joints is uncontrolled. These uncontrolled, passive rotations are also the reason why II-type and IO-type singularities exist. II-type (IO-type) singularities exist when there exists an input (output) that cannot be determined by any output (input) and passive velocity vector combination. This is the case globally because the passive rotations are undefined with multiple solutions (app. B.4.2).

These singularities disappeared from the workspace when the Jacobian matrix was calculated for the original mechanism with two prismatic joints, four spherical joints and three universal joints. The mobility, n, for the mechanism remained the same at two degrees of freedom. However, the total number of joints, N, used in the calculation changed to eight because the three redundant passive rotations were removed from the system. To remove the specified rotations, equation 4.61 was removed from the system of equations, and instead, it used to eliminate one rotational velocity component from each of the inboard joints on the rear and cross cylinder limbs (eq. 4.69 & 4.71). An expression for one of the rotational velocity components on the inboard joint of the fixed-length link was formed using the definition of the dot product that defines the angle between the link vector and the vector from the inboard link joint to the outboard upper control arm joint (eq. 4.67). This angle, θ_B, was always when the outboard upper control arm joint was fixed. The fixed-length link and outboard upper control arm joint formed a three-bar linkage that had only one degree of freedom. That degree of freedom was the rotation about the axis from the inboard link joint to the outboard upper control arm joint. Therefore, the time derivative of equation 4.67 was equal to zero on the right side (eq. 4.68). An expression for a rotational velocity component of the inboard link joint was formed by rearranging equation 4.68 (eq. 4.70).

$$\hat{\boldsymbol{b}} \cdot (\boldsymbol{S} - \boldsymbol{BI}) = \|\boldsymbol{S} - \boldsymbol{BI}\| \cos\theta_B \tag{4.67}$$

$$(\boldsymbol{\omega_B} \times \hat{\boldsymbol{b}}) \cdot (\boldsymbol{S} - \boldsymbol{BI}) = 0 \tag{4.68}$$

$$\begin{split}\omega_{Ax} = \frac{1}{l_A \hat{a}_z}((\boldsymbol{R}(\boldsymbol{AO_i} - \boldsymbol{CO_i}))_z \omega_x - (\boldsymbol{R}(\boldsymbol{AO_i} - \boldsymbol{CO_i}))_x \omega_z + \hat{a}_y \dot{l}_A - \hat{c}_y \dot{l}_C \\ + \hat{a}_x l_A \omega_{Az} + \hat{c}_z l_C \omega_{Cx} - \hat{c}_x l_C \omega_{Cz})\end{split} \tag{4.69}$$

$$\omega_{Bx} = \frac{((S_x - BI_x)\hat{b}_z - (S_z - BI_z)\hat{b}_x)\omega_{By} + ((S_y - BI_y)\hat{b}_x - (S_x - BI_x)\hat{b}_y)\omega_{Bz}}{(S_y - BI_y)\hat{b}_z - (S_z - BI_z)\hat{b}_y} \tag{4.70}$$

$$\begin{split}\omega_{Cy} = \frac{1}{l_C \hat{c}_z}(-(\boldsymbol{R}(\boldsymbol{AO_i} - \boldsymbol{CO_i}))_z \omega_y + (\boldsymbol{R}(\boldsymbol{AO_i} - \boldsymbol{CO_i}))_y \omega_z + \hat{a}_x \dot{l}_A - \hat{c}_x \dot{l}_C \\ + \hat{a}_z l_A \omega_{Ay} - \hat{a}_y l_A \omega_{Az} + \hat{c}_y l_C \omega_{Cz})\end{split} \tag{4.71}$$

When equations 4.69 to 4.71 were substituted into equation 4.62, Zlatonov's criteria for singularity changes to the following list below. Based on Zlatonov's singularity criteria, there were no global singularities. The ranks of the instantaneous Jacobian matrices were the same as the ranks for the global Jacobian matrices. Therefore, there were no configurations in the workspace which result in a singularity.

i) $q \epsilon \text{ RI} \Leftrightarrow \text{rank}(\boldsymbol{J_O}) = 8 < \text{rank}(\boldsymbol{J_p}) + n = 8$

ii) $q \epsilon \text{ RO} \Leftrightarrow \text{rank}(\boldsymbol{J_I}) = 9 < \text{rank}(\boldsymbol{J_p}) + n = 8$

iii) $q \epsilon \text{ RPM} \Leftrightarrow \text{rank}(\boldsymbol{J_p}) = 6 < N - n = 6$

iv) $q \epsilon \text{ II} \Leftrightarrow \text{rank}(\boldsymbol{J_I}) = 9 < \text{rank}(\boldsymbol{J}) = 8$

v) $q \epsilon \text{ IO} \Leftrightarrow \text{rank}(\boldsymbol{J_O}) = 8 < \text{rank}(\boldsymbol{J}) = 8$

vi) $q \epsilon \text{ IIM} \Leftrightarrow \text{rank}(\boldsymbol{J}) = 8 < N = 8$

4.6 Sensitivity Analysis

A sensitivity analysis was performed on the final corner module concept to determine the sensitivity in steer angle to both of the rear and cross cylinders when the camber was kept fixed. Figure 4.12 shows the steer angle rate of change over the rear cylinder length rate of change for different steer and camber positions. From the figure, it is apparent that there are large magnitudes of sensitivity. This was not caused by an extreme change in steer angle. Instead, the rear cylinder length hardly changed in these locations to achieve a change in steer angle at constant camber angle. The change in steer angle was kept constant at 5° while the step size in the rear cylinder varied for each configuration. These configurations were not singularities because the steer angle is changed using the cross cylinder. At these configurations, the rear and cross cylinders were decoupled. The lowest

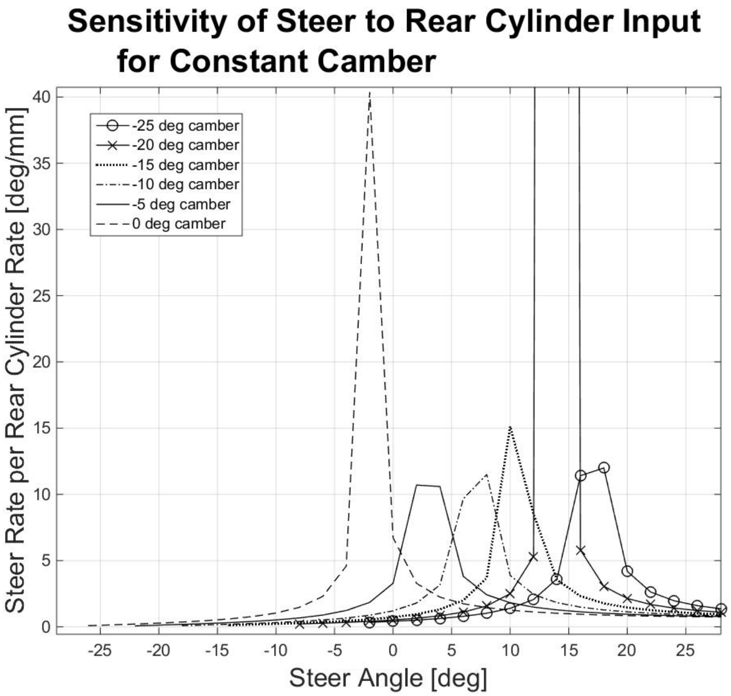

Figure 4.12: Sensitivity of the steer angle output to the rear cylinder length input.

sensitivity ratio in figure 4.12 was 0.082 °/mm. At this configuration, a 1° change in steer angle was caused by a 12.2 mm change in the rear cylinder length. Fortunately, this location occurred at the edge of the workspace at 0° camber and −26° steer.

The sensitivity of the steer angle change to a change in cross cylinder length is shown in figure 4.13. There were no relatively large sensitivity ratios on this graph. Therefore, the cross cylinder length change always influenced the steer angle. The lowest value on the sensitivity curves for cross cylinder input was 0.155 °/mm. Therefore, to change the steer angle by 1° at this location required a 6.5 mm length change in the cross cylinder. This sensitivity ratio value occurred at −5° camber and −22° steer.

The sensitivity of the camber angle change to the change in length of the rear and cross cylinders at constant steer angles is shown in figures 4.14 and 4.15, respectively. None of

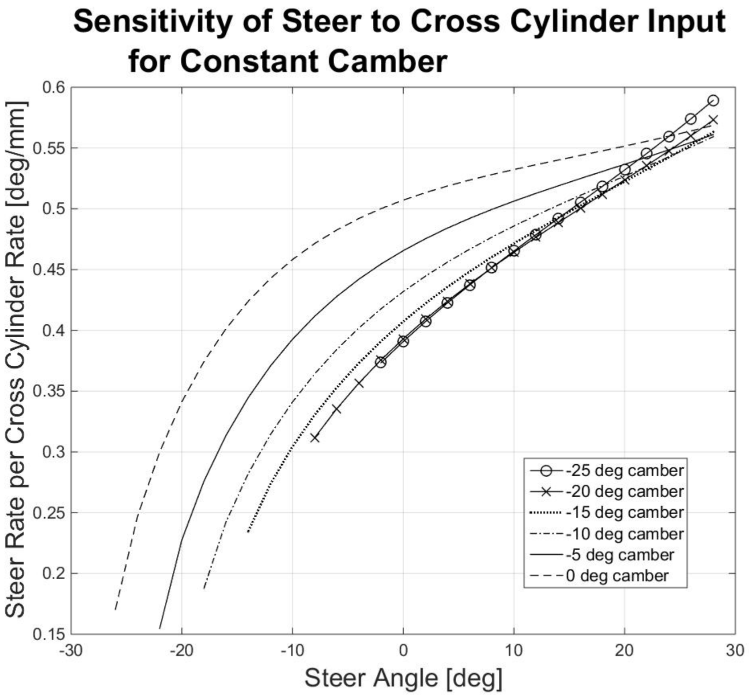

Figure 4.13: Sensitivity of the steer angle output to the cross cylinder length input.

the sensitivity ratios for either cylinder were of a magnitude greater than one. Therefore, both cylinders were always active when controlling the camber angle. In both figures, sensitivity data was missing for certain steer angles at 0° camber. This was caused by the large step size in the available data points. Data was also missing from steer angles greater than $-18°$. This was also caused by that large step size. The camber angle sensitivity to the rear cylinder had a smallest sensitivity ratio of approximately 0.09 °/mm. The camber angle sensitivity to the cross cylinder had a smallest sensitivity ratio of approximately 0.25 °/mm. Both of these minimum ratios occurred at $-20°$ steer and $-5°$. The camber angle was more difficult to control at lower negative steer angles.

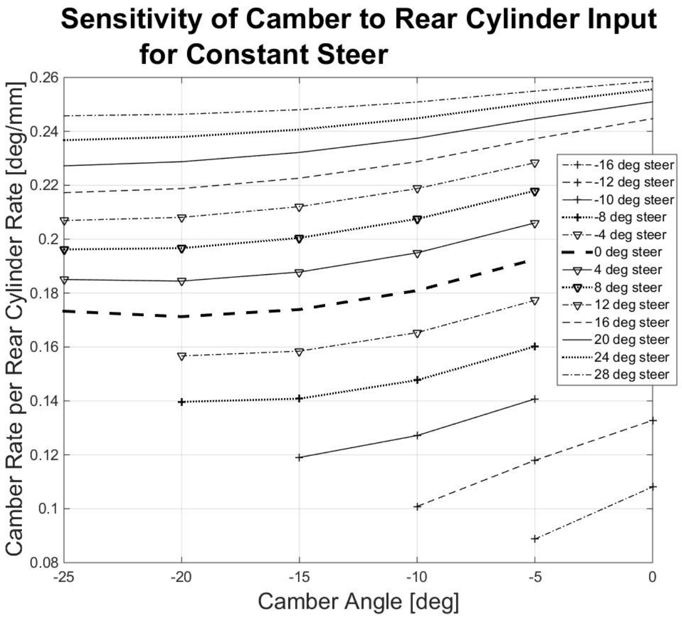

Figure 4.14: Sensitivity of the camber angle output to the rear cylinder length input.

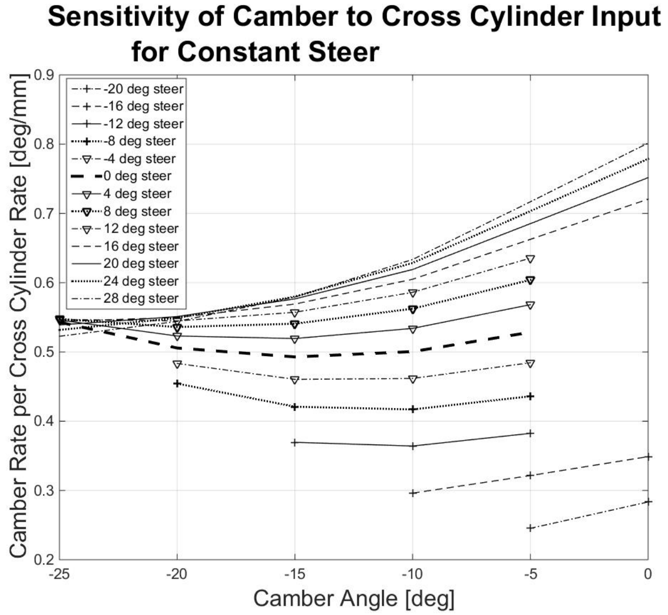

Figure 4.15: Sensitivity of the camber angle output to the cross cylinder length input.

Chapter 5

Suspension Kinematic and Dynamic Modelling

5.1 Bump Camber

Once the hard point optimization was complete, the locations of the rear cylinder joints, fixed-length link joints and outboard upper control arm joint were known. However, the inboard upper control arm joint positions still needed to be determined. Placement of the inboard upper control arm joints in the y- and z-directions would impact the passive bump camber (and camber-by-roll) behaviour of the vehicle and the dynamic translation of the center of gravity (CG) of the sprung mass about the roll center (fig. 5.1). The fore and aft inboard upper control arm joints were placed concentric to one another along an axis parallel to the x-axis. This was done to simplify the design. Anti-dive and anti-squat mechanism geometry was not considered for this iteration of the corner module.

To increase the understeer tendencies of the vehicle in a turn, the outside tires should have negative camber angles [17][1]. Therefore, the position of the inboard upper control arm joints should cause the wheel to increase in negative camber when the spring was compressed. The amount of body roll for a lateral acceleration is dependent on the spring

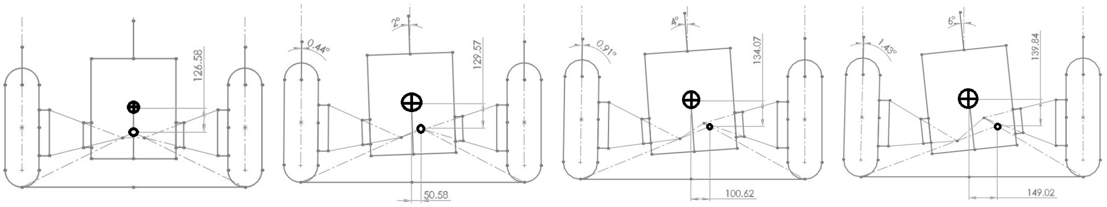

(a) 0° roll angle (b) 2° roll angle (c) 4° roll angle (d) 6° roll angle

Figure 5.1: Geometric definition of the roll center with respect to the sprung mass CG.

stiffness and the distance between the CG and the roll center. The vehicle body would roll less if the roll center was closer to the center of gravity. Therefore, the roll center should not be too far away from the CG so that there isn't excessive body roll, but it also should not be so close to the CG that the tire forces are overloaded by the lateral acceleration. The roll center should not be above the CG as this would reduce the tire forces on the outside wheel and cause the vehicle body to lift. It was also important to minimize the travel of the roll center to maintain driving predictability. Figure 5.2 shows the camber alteration at various mechanism configurations.

The vehicle will have understeer tendencies if the front camber-by-roll coefficient is less than the rear camber-by-roll coefficient [1]. However, the vehicle had three wheels in the tadpole configuration. Therefore, the type of suspension geometry on the rear corner module would dictate whether the roll center would be located at the ground or located to the left or the right side of the vehicle depending on how the rear corner module is mounted to the body.

Consider the case where the proposed corner module is used as the rear wheel. The roll center will be above ground and below the CG. However, depending on whether the left or right corner module is used, the roll center will be located either to the left or the right of the xz-plane of the vehicle. Therefore, the vehicle body with have different roll behaviour depending on whether the vehicle is completing a left or a right turn.

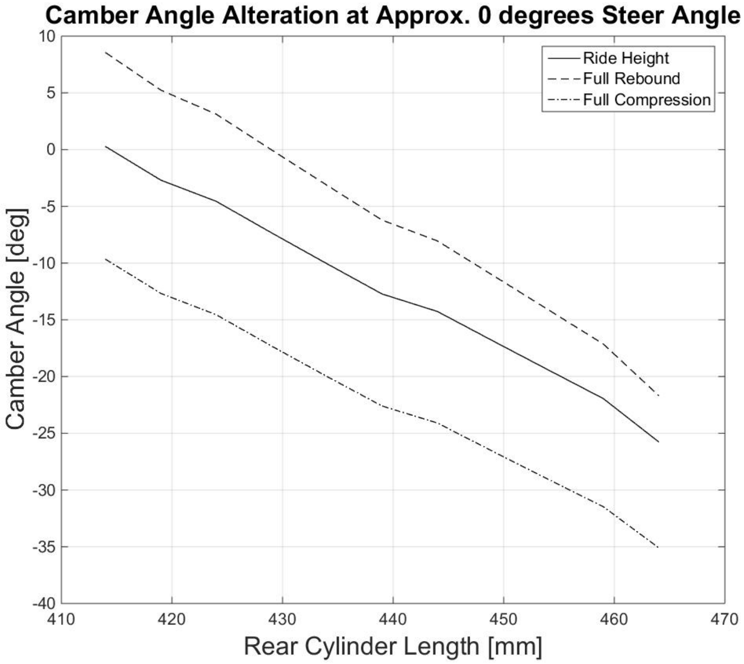

Figure 5.2: Camber alteration at approximately 0° steer angle.

Now consider the case where a trailing arm suspension is used for the rear with combined with the proposed corner modules in the front of the vehicle. The rear roll center will be located at the ground if a trailing arm suspension is used. Therefore, when the body rolls, the rear wheel will rotate with vehicle body about the roll center on the ground. The rear wheel will camber out of the turn and subsequently reduce the lateral force at the rear wheel. This will decrease the understeer tendencies of the vehicle. Therefore, it is preferable to use a suspension geometry, such as a trailing arm suspension, that has a roll center at the ground for the rear wheel of the three-wheeled vehicle. To offset the decrease in understeer tendencies, an active camber system should be used on the rear wheel. Also, the corner module could be designed such that there is minimal camber alteration the yz-lengths of the upper and lower control arms equal to one another.

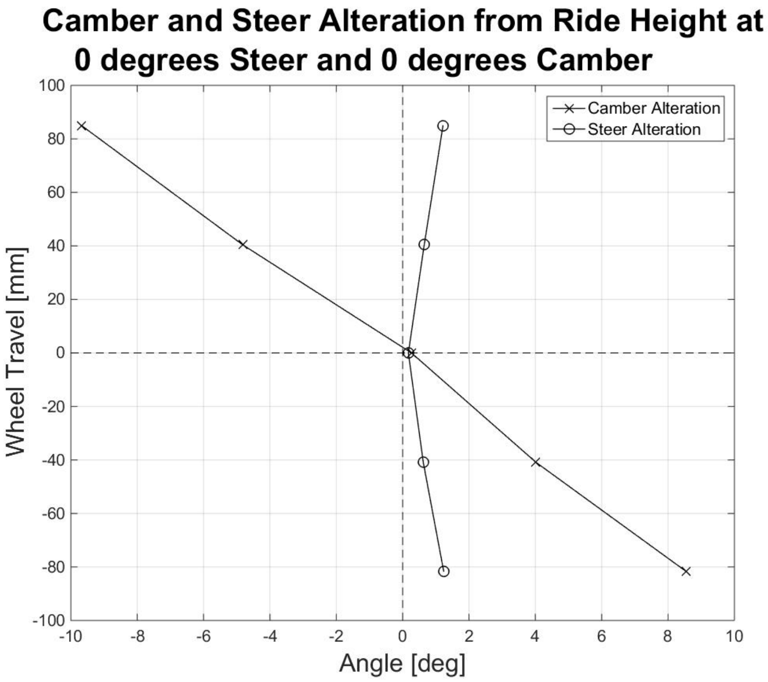

Figure 5.3: Steer and camber alteration from approximately 0 steer angle and 0 camber angle.

5.2 Bump Steer

The bump steer characteristic of the corner module was influenced by the placement of the cross cylinder. However, the cross cylinder placement also impacted the distribution of force in the suspension links. Therefore, the cross cylinder was packaged to minimize the bump steer behaviour and minimize the forces in the links while meeting the packaging constraints and the cylinder stroke and compressed length constraints.

To minimize the bump steer, the cross cylinder was aligned such that the axis concentric with the cross cylinder intersected the roll axis of the wheel assembly in the ride height position at 0° steer and 0° camber. The roll axis of the wheel assembly was coincident with the plane formed by the three joints on the upper control arm. This axis connected

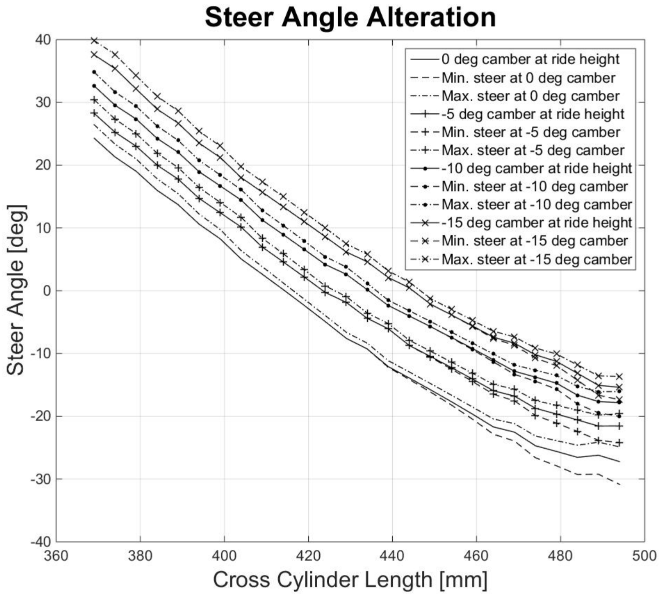

Figure 5.4: Steer alteration at approximately 0°, $-5°$,$-10°$ and $-15°$ camber angles.

the two points where the lines concentric with the fixed-length link and the rear cylinder intersected the upper control arm plane.

The forces in the links were more equally distributed when the cross cylinder was parallel to the vehicle body when the wheel was in the 0° steer, 0° camber and ride height position. This could not be achieved without increasing the bump steer or causing component interference. Therefore, a compromise was necessary. The cross cylinder did not have to be parallel with the vehicle body as long as the forces in the cylinders did not exceed 19 kN in compression and 9 kN in tension, and ±12 kN in the fixed-length link. The cylinders and fixed-length link would fail at these limits.

The cross cylinder was successfully packaged to meet the constraints and sufficiently minimize the bump steer. All of the forces were within the acceptable range (sec. 5.5). The steer alteration caused by bump is shown in figure 5.4. The maximum steer alteration within the workspace was a change of 4.01° from full rebound to full compression. This

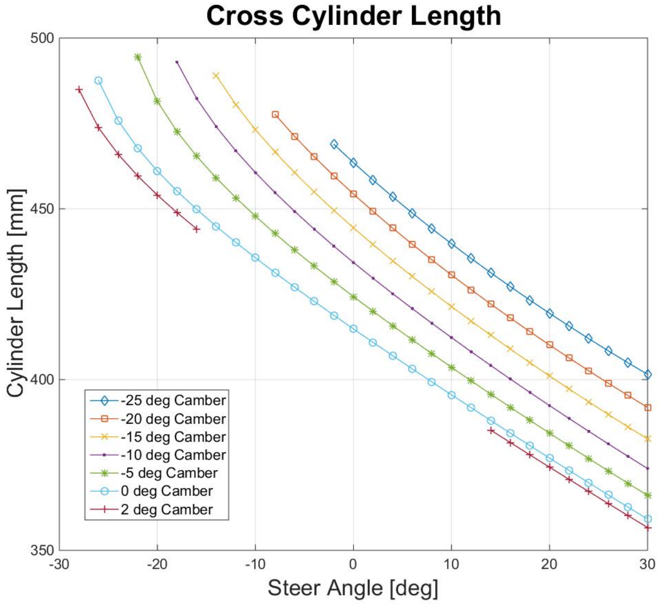

Figure 5.5: Cross cylinder length for various camber and steer angles [35].

occurred at the edge of the workspace at 0° camber and −25.6° steer. In this configuration, the bump steer factor wass approximately 0.024°/mm. The average bump steer factor was approximately 0.017°/mm. The cross cylinder length variation is shown in figure 5.5 given varying steer and camber angle combinations.

5.3 Spring and Damper Selection

The spring and damper could not be packaged until all of the hard points of the corner module were known. Placement of the spring and damper would determine the motion ratio. In the optimization, the outboard upper control arm joint, $\boldsymbol{S}$, was constrained by the z-component upper limit of 450 mm from the ground at ride height. This was done to allow packaging space for the spring and damper above the upper control arm. The spring stiffness, k_s, free spring length, l_{free}, motion ratio, K_{MR} and damper force-velocity curve had to be known in order to size a spring and damper for the vehicle.

Due to packaging constraints, a damper with a coil-over spring was integrated into the suspension. When fully extended, the damper could fit a spring of 7.75" in length, therefore, any springs longer than 7.75" would develop a preload before the weight of the vehicle was applied to the spring. The length of the spring at ride height was found using equation 5.1.

$$l_{RH} = l_{free} - l_{pre} - \frac{m_s b K_{MR}}{2(a+b)k_s} \tag{5.1}$$

The spring parameters also depended on the motion ratio, the target natural frequencies of the sprung and unsprung masses (f_{n1} and f_{n2} in Hz or ω_{n1} and ω_2 in rad/s), and the tire stiffness, k_u. The target natural frequencies of the unsprung and sprung masses were between 10 and 12 Hz, and between 1 and 1.33 Hz [2], respectively. These targets were selected such that the vehicle body would not resonate at frequencies that excite the human body [20]. A two degree of freedom quarter car model was used to determine the spring stiffness. Therefore, only half of the front sprung mass, m_f, was used in the model as the vehicle body or sprung mass. After some trial and error, a body natural frequency of 1.1 Hz was selected to define the spring stiffness. Equations 5.2 to 5.7 were used to determine the spring stiffness. Once the spring stiffness was known, the wheel natural frequency was calculated to verify that it was within 10 and 12 Hz (eq. 5.8 & 5.9) [22]. Trial and error was completed to package the spring, select the free length and determine the natural frequencies. It resulted in a spring stiffness of 350 lb/in, spring length of 8" and a motion ratio of 2.5.

$$r_1 = \frac{\omega_{n1}}{\omega_s} \tag{5.2}$$

$$\omega_u = \sqrt{\frac{k_u}{m_u}} \tag{5.3}$$

$$a = \frac{\omega_s}{\omega_u} \tag{5.4}$$

$$e = \frac{m_f}{2m_u} \tag{5.5}$$

$$r_1 = \sqrt{\frac{1}{2a^2}(1 + (1+e)a^2 - \sqrt{(1 + (1+e)a^2)^2 - 4a^2}} \tag{5.6}$$

$$k_s = \omega_s^2 \frac{m_f}{2} K_{MR}^2 \tag{5.7}$$

$$r_2 = \frac{\omega_{n2}}{\omega_s} \tag{5.8}$$

$$r_2 = \sqrt{\frac{1}{2a^2}(1 + (1+e)a^2 + \sqrt{(1 + (1+e)a^2)^2 - 4a^2}} \tag{5.9}$$

The damper valve sizes were specified after the spring parameters were selected. The valves determined the force-velocity curves of the damper. The damping coefficients for the high and low damper speeds were specified to minimize the vibration transmission to the sprung mass. Damping coefficient, c, depended on the sprung mass, spring stiffness, motion ratio and damping ratio, ζ, (eq. 5.10).

$$c_w = \zeta 2 \sqrt{k_s m_s} K_{MR}^2 \tag{5.10}$$

The high and low speed damping ratios were selected using figure 5.6. The low speed damping coefficient selected was 0.5, and the high speed damping coefficient selected was 0.2. The damping velocity at which the damping ratios changed was chosen based on figure 5.6a. From the figure, it is apparent that the minimum damping ratio curve becomes the maximum of the five curves at a frequency ratio of 1.377.

The frequency at which the damping ratio changes is called the knee frequency. The knee frequency was determined using the equation for the frequency ratio (eq. 5.11) given the sprung mass natural frequency and the frequency ratio at the knee. The knee damper velocity was determined using equation 5.12 for an average road amplitude, A. By knowing the knee velocity and the high and low damping coefficients, the average damping force for any damper velocity could be found (eq. 5.13).

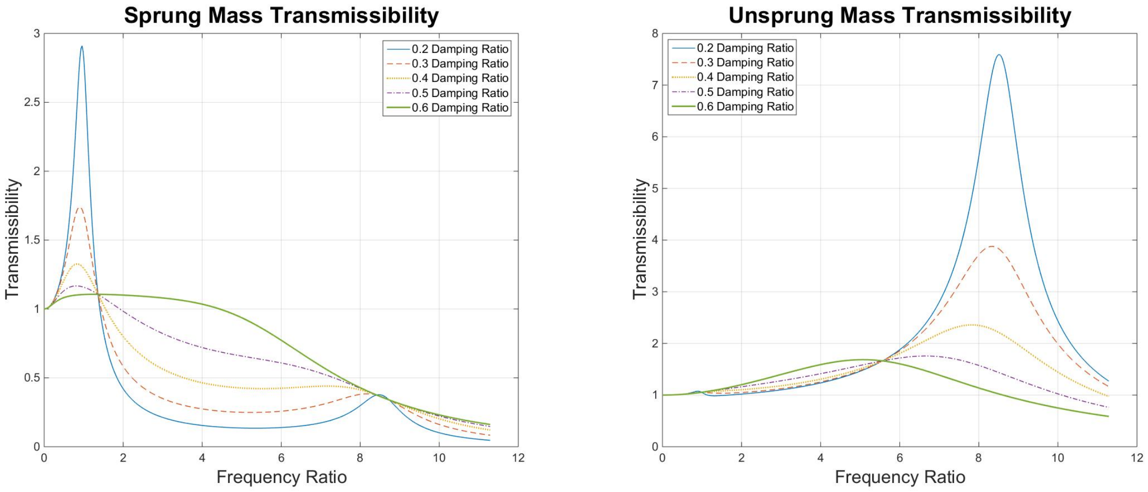

(a) Sprung mass transmissibility.

(b) Unsprung mass transmissibility.

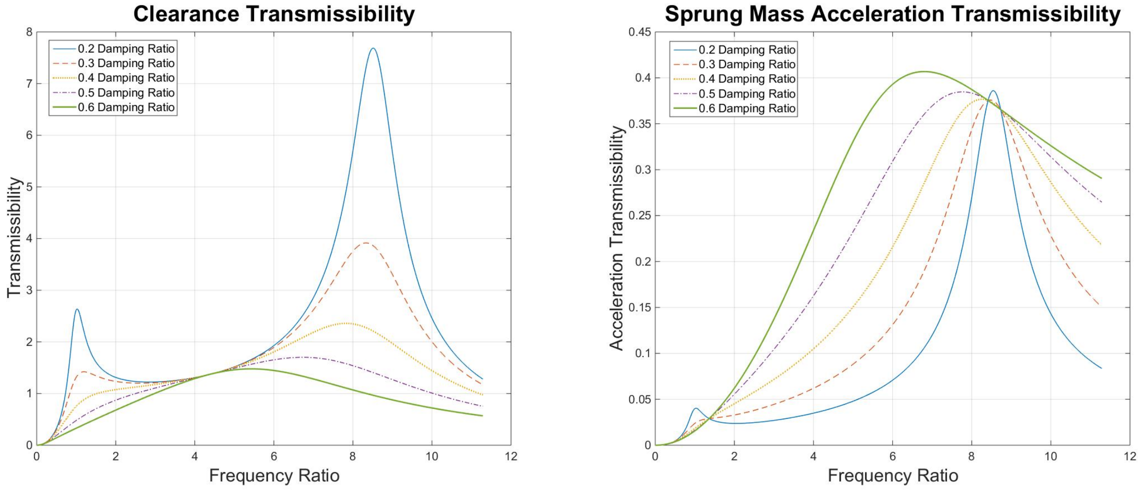

(c) Wheel clearance transmissibility.

(d) Sprung mass acceleration transmissibility.

Figure 5.6: Transmissibility results for selected spring and damper.

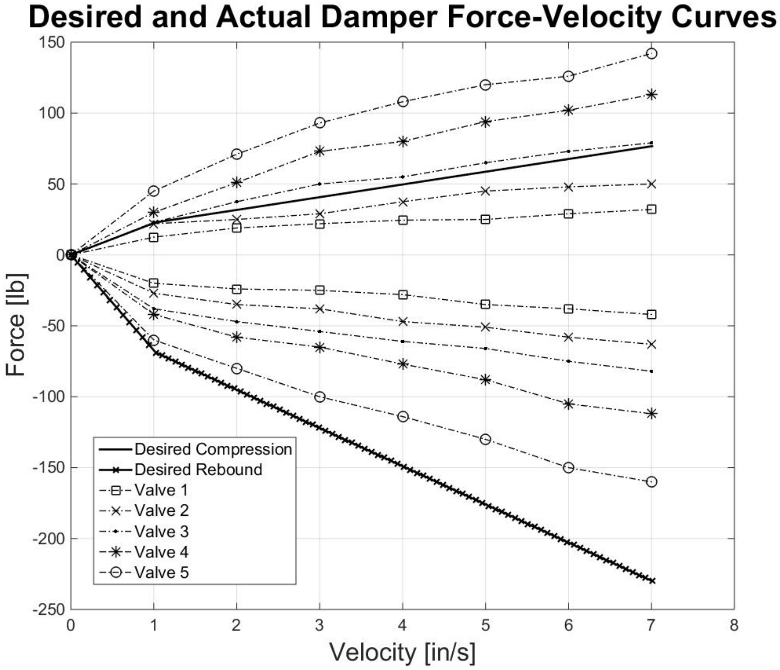

Figure 5.7: Desired and actual force-velocity curves for different valving options. Positive force is compression and negative is rebound.

$$\omega_k = r_k \omega_s \tag{5.11}$$

$$v_k = \frac{A\omega_k}{K_{MR} 2\pi} \tag{5.12}$$

$$F_m = cv \tag{5.13}$$

The desired compression and rebound forces were found as a function of the average damping force and ratio of rebound force to compression force. This ratio is usually 3 to 5 for passenger vehicles [18]. A ratio of 3 was used for the rebound force and compression force calculations. The compression and rebound forces were determined using equations 5.14 and 5.15, respectively [18].

$$F_{comp} = F_m \frac{2}{1 + r_{r-c}} \tag{5.14}$$

$$F_{reb} = -F_m \frac{2r_{r-c}}{1 + r_{r-c}} \tag{5.15}$$

Once the desired force-velocity curve for the corner module's damper was constructed, compression and rebound valves for the damper were selected such that the actual force-velocity curve would closely match the desired force-velocity curve. The different valve options as well as the desired compression and rebound curves are shown in figure 5.7. Different valves for the could be selected for rebound and compression. Valve 3 was selected for the damper compression, and valve 5 was selected for the damper rebound.

5.4 Caliper and Rotor Selection

The rotor and caliper were selected using a longitudinal vehicle model for the condition of locked braking undergoing a deceleration of 1 g. The maximum brake pressure in the lines was 1500 psi. The theoretical brake pressure was calculated using equation 5.18 [27]. The free design variables were the rotor radius, r_{rotor}, and the piston area, A_p. The effective rotor radius, r_e (eq. 5.16 [9]), and the normal force on one of the front tires, F_{zfl} (eq. 5.17 [27]), had to be calculated to determine the brake pressure, P_{brake}. The local piston pressure, p, was assumed to be uninfluenced by a change in radius between the upper and lower brake pad radii (r_o and r_i).

$$r_e = \frac{\int_{r_i}^{r_o} pr^2 dr}{\int_{r_i}^{r_o} prdr} = \frac{2(r_o^3 - r_i^3)}{3(r_o^2 - r_i^2)} \tag{5.16}$$

$$F_{zfl} = mg\left(\frac{b}{2(a+b)} + \frac{a_x h}{g(a+b)}\right) \tag{5.17}$$

$$P_{brake} = \frac{\mu_{road} F_{zfl} r_{wheel}}{\mu_{pad} A_p r_e} \tag{5.18}$$

Packaging was also considered when selecting a rotor and a caliper. A steel, 11.44" diameter rotor and a caliper with a piston area of 2.46 in^2 required a brake pressure of

Figure 5.8: Wheel assembly showing the packaging of the selected rotor and caliper. The rotor connects to the wheel via the rotor coupler.

1316 psi to lock the wheels during a longitudinal deceleration of 1 g. A caliper and rotor combination that met these requirements was also capable of fitting in the designated packaging space (fig. 5.8).

5.5 Force Analysis

5.5.1 Lateral Dynamics

To complete a force analysis on the various suspension components, the forces at the contact patch had to be estimated. A three degree of freedom handling model was used to estimate the forces at the contact patch. This model accounted for the lateral, yaw and roll accelerations of the vehicle (eq. 5.19 to 5.21) [24]. The longitudinal velocity was assumed to be constant. The model calculated the forces at different wheel configurations given the steer and camber angles. When the steer angle was 0°, this handling model was not practical as there would be no lateral acceleration or yaw rate. At 0° steer, a simplified braking model was used for 1 g of longitudinal deceleration. This model was explained in section 5.4. The Simulink diagram for the handling model is shown in appendix B.5.

$$m(\dot{v} + ur) = F_{yfl} + F_{yfr} + F_{yr} = 2(C_{\alpha f}\alpha_f + C_{\gamma f}\gamma_f) + (C_{\alpha r}\alpha_r + C_{\gamma r}\gamma_r) \tag{5.19}$$

$$I_z\dot{r} = a(F_{yfl} + F_{yfr}) + bF_{yr} = 2a(C_{\alpha f}\alpha_f + C_{\gamma f}\gamma_f) + (C_{\alpha r}\alpha_r + bC_{\gamma r}\gamma_r) \tag{5.20}$$

$$m_s h(\dot{v} + ur) = I_{xx}\ddot{\phi} + c_t\dot{\phi} + (k_t - m_s g h)\phi \tag{5.21}$$

The normal forces for the front left, front right and rear tires were estimated using equations 5.22, 5.23 and 5.24, respectively [24]. These equations accounted for lateral load transfer.

$$F_{zfl} = \frac{mg}{2}\left(\frac{a}{a+b} + \frac{a_y h}{gT} - \frac{m_s h}{m(a+b)}\sin\phi\right) \tag{5.22}$$

$$F_{zfr} = \frac{mg}{2}\left(\frac{a}{a+b} - \frac{a_y h}{gT} - \frac{m_s h}{m(a+b)}\sin\phi\right) \tag{5.23}$$

$$F_{zr} = \frac{mga}{a+b} \tag{5.24}$$

The front lateral forces were calculated using the tire cornering stiffness, C_α, the side slip angle, α, the tire cambering stiffness, C_γ, and the camber angle, γ (eq. 5.25) [24]. The side slip angle was dependent on the steer angle, δ, steer-by-roll coefficient, K_{sbr}, roll angle, ϕ, lateral velocity, v, longitudinal velocity, u, yaw rate, r, and longitudinal distance from the front wheels to the CG, a (eq. 5.26) [24]. The camber angle was the addition of the initial camber angle and the change in camber angle with roll (eq. 5.27) [24].

$$F_{yf} = 2(C_{\alpha f}\alpha_f + C_{\gamma f}\gamma_f) \tag{5.25}$$

$$\alpha_f = \delta_f + K_{sbr-f}\phi - \tan^{-1}\left(\frac{v + ar}{u}\right) \tag{5.26}$$

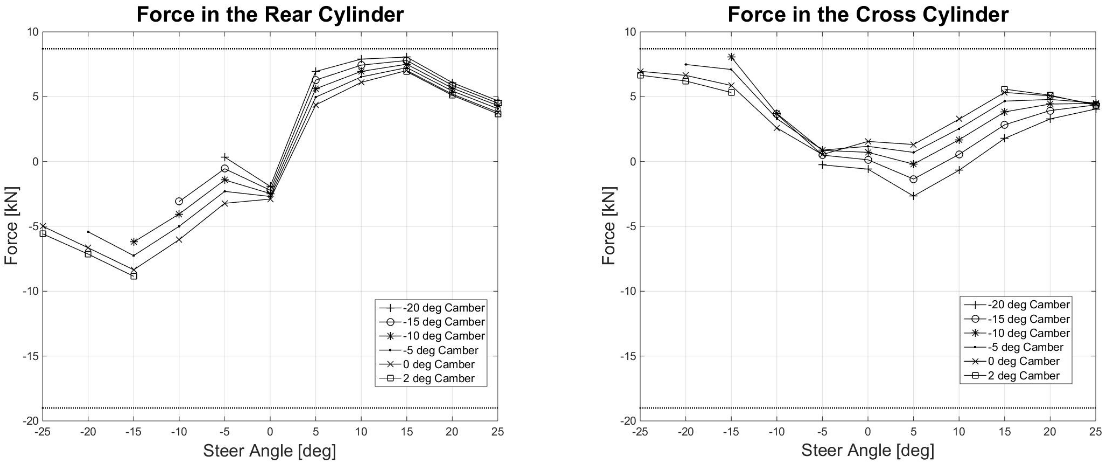

(a) Force in the rear cylinder.

(b) Force in the cross cylinder.

Figure 5.9: Forces in the cylinders.

$$\gamma_f = \gamma + K_{cbrf}\phi \tag{5.27}$$

Once the forces at the contact patch were known, the forces in the suspension components could be determined using the sum of the forces and sum of the moments equations. The directions of the forces in the fixed-length link and the cylinders was known without calculation because they were two-force links. Therefore, the force would always act along the length of the link in either compression or tension. There were only x-, y- and z-component forces acting on the outboard upper control arm joint because it was a spherical bearing and did not resist any moments. Therefore, there were six equations and six unknowns so the forces could be solved.

Figures 5.9 and 5.10 show the forces in the suspension components for the selected placement of the cross cylinder. For the two-force links, a positive force indicates that the link is in tension whereas a negative force indicates that the link is in compression. The horizontal lines on figure 5.9a, 5.9b and 5.10a indicate there upper and lower bounds at which either the cylinders or the fixed-length link will deform. The forces shown in these

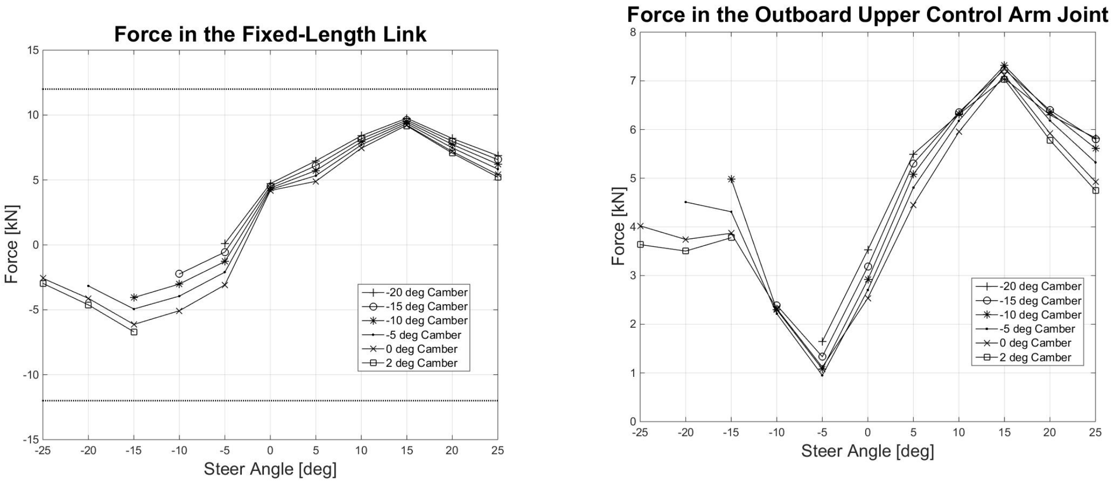

(a) Force in the fixed-length link.

(b) Resultant force in the outboard upper control arm joint.

Figure 5.10: Forces in the fixed-length link and upper control arm outboard joint.

four figures represent a worst case scenario as the lateral acceleration is between 0.7 g and 1 g for steer angles between $-15°$ and $15°$, and less than 0.5 g for steer angles outside of $-15°$ and $15°$.

5.5.2 Vertical Dynamics

The vertical dynamics of the vehicle were modeled using a two degree of freedom system similar to the one used in section 5.3. The objective of this model was to determine the maximum force exerted by the spring and damper when the vehicle traverses a pothole. This force was used later as the maximum load experienced by the upper control arm from the shock absorber.

The maximum forces acting on the upper control arm were determined using a two degree of freedom quarter car model. The system consisted of the sprung mass supported by one of the front wheels, m_s, which was connected to the unsprung mass, m_u, by the spring and damper. It was assumed that the unsprung mass would remain in contact with the road through a spring with a stiffness equivalent to the tire's vertical stiffness, k_t. The spring stiffness, k_s, and the damping coefficient, c_s, were inline with the wheel travel for the system of equations below (eq. 5.28 & 5.29) [19]. The Simulink model for the system of equations below is presented in appendix B.6. The sprung mass, unsprung mass and road vertical displacements were defined as x_s, x_u and y, respectively.

$$m_s\ddot{x}_s + c_s(\dot{x}_s - \dot{x}_u) + k_s(x_s - x_u) = 0 \tag{5.28}$$

$$m_u\ddot{x}_u + c_s(\dot{x}_u - \dot{x}_s) + k_s(x_u - x_s) + k_t(x_u - y) = 0 \tag{5.29}$$

The event where the vehicle impacting a bump while traveling at 100 km/hr was simulated. This was assumed to be the worst case scenario. The bump was modeled as a Watts speed bump which is 10 cm in amplitude and 370 cm long (fig. 5.11a). Figure 5.11b shows the vertical displacement of the sprung mass and unsprung mass as well as the wheel clearance before it hits the shock absorber bump stop. The vertical velocities of the sprung and unsprung masses are shown in figure 5.11c. The forces exerted by the spring, damper, sprung mass and unsprung mass are shown in figure 5.11d. From equation 5.28, the force exerted by the sprung mass wass the addition of the damper force and spring force. Therefore, the force transferred to the upper control arm at the damper mount was equal to the sprung mass force. The force from the unsprung mass acted at the outboard ball joint. These forces caused an oscillating rotation of the upper control arm about the inboard bushings (fig. 5.12).

The rotational acceleration was found by transforming the linear acceleration of the unsprung mass to be perpendicular with the radius of the upper control arm, then converting it to a rotational acceleration using the same radius (eq. 5.30 & 5.31). It was assumed that the unsprung mass displacement was equal to the vertical displacement of the outboard upper control arm ball joint. It was determined from the SolidWorks model

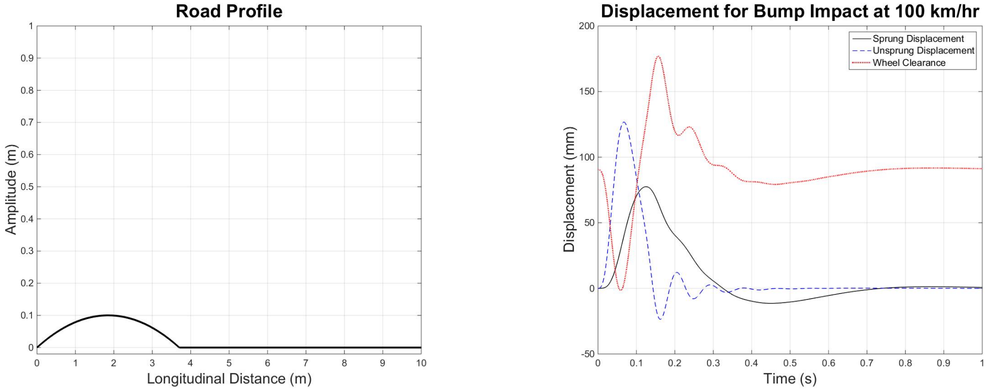

(a) Road profile (b) Displacement and wheel clearance

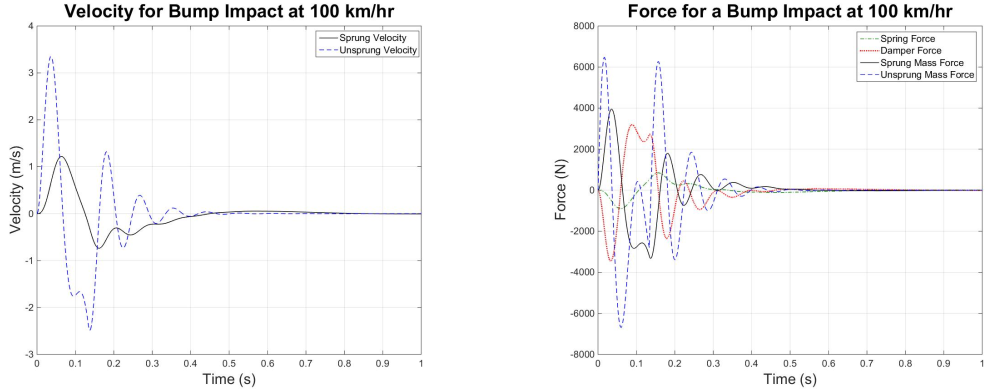

(c) Velocity (d) Force

Figure 5.11: Two degree of freedom, quarter car model during the event of bump impact at 100 km/hr.

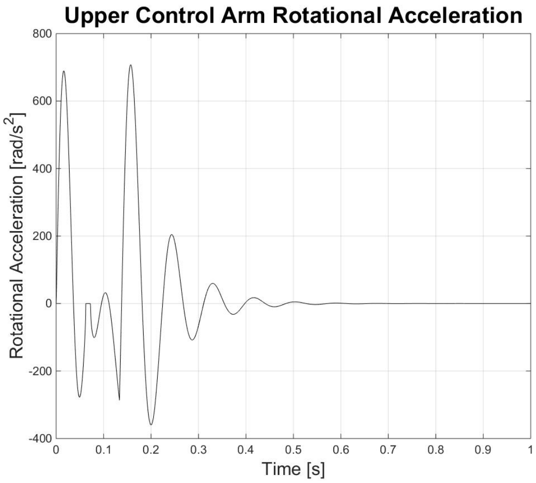

Figure 5.12: Upper control arm rotational acceleration [rad/s^2].

that the upper control arm had a mass moment of inertia of 0.0078 kg-mm^2 about the x-axis at its center of mass. Using the parallel axis theorem (eq. 5.32), the mass moment of inertia about the center axis of the bushings was determined to be 0.0263 kg-mm^2.

$$\alpha = \frac{\ddot{x}_u \cos\theta}{r} \tag{5.30}$$

$$\theta = \sin^{-1}\left(\frac{x_u + x_o}{r}\right) \tag{5.31}$$

$$I = I_{x,cm} + md^2 \tag{5.32}$$

Chapter 6

Detailed Design

6.1 Rotor Coupler

Similar to the caliper and rotor selection, the case that would induce the maximum load in the rotor coupler was when the vehicle underwent locked braking and 1 g of deceleration. Due to the normal force applied by the caliper to the rotor, the rotor coupler would have to resist the induced torsion as well as planar forces. For the worst case scenario, the rotor was assumed to be rigid. The rotor coupler is shown in figure 5.8.

The bolt size at the rotor was already determined because the rotor was a standard, purchased part. There were 8 bolt holes in the rotor equally spaced at a radius of 88.9 mm, and designed for 5/16" diameter bolts. Although calculations suggested that the bolts and the rotor coupler could withstand the shear force, it was preferable that the bolt clamping be substantial enough to prevent any shear load on the bolts. All calculations to determine the factor of safety in the custom parts (sections 6.1 to 6.6) were done using the equations specified in the 9th edition of Shigley's Mechanical Engineering Design textbook [9].

In the condition of locked braking during a deceleration of 1 g, the moment generated by the wheel was 477 Nm (eq. 6.1) [14][28]. Therefore, the preload in a set of bolts must be capable of withstanding that moment. The method for calculating the factors of safety and preload forces were the same for the rotor connecting bolts and the motor connecting bolts. The only differences were the bolt diameters and center radii. In this section, d will represent the bolt diameter and R will represent the center radius. The normal force at the contact patch was found using equation 5.17. The longitudinal force at the contact patch was found using a simplified tire model that depended on the longitudinal slip, s, and the coefficient of friction between the tire and the road, μ_{road} [14]. The longitudinal slip factor was equal to 1 as the wheels were locked.

$$M_w = \frac{\mu_{road} F_{zfl}}{80}(-30s + 86) r_{wheel} \tag{6.1}$$

The preload force and preload torque per bolt was calculated using equations 6.2 and 6.3, respectively [9]. Because both sets of bolts were fastening to aluminium material, the proof strength, Sp, was that of the aluminium. The connection type was non-permanent (a=0.75), and both sets of bolts required a threadlocker liquid so a torque factor, K, of 0.15 was used. The clamping moment generated by the bolt preload force was found by multiplying the frictional force between the two parts to be clamped with the center radius of the bolt pattern and the number of bolts, N, in the bolt pattern (eq. 6.4). The factor of safety, FoS, against the rotor coupler rotating with respect to the rotor or the motor was determined using equation 6.5. The factors of safety for the rotor slip and motor slip assuming a low coefficient of friction between the two clamped surfaces was 2.26 and 2.08, respectively.

$$F_i = a S_p A_t \tag{6.2}$$

$$T_i = K F_i d \tag{6.3}$$

$$M_c = \mu F_i R N \tag{6.4}$$

$$FoS = \frac{M_c}{M_w} \tag{6.5}$$

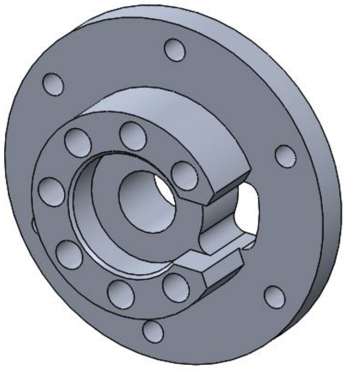

Figure 6.1: Upright Coupler.

6.2 Upright Coupler

The upright coupler connected the motor to the upright. Figure 6.1 shows the final design of the upright coupler which was made from 6061-T6 aluminium. Only seven bolt holes were used for the connection to the motor because the motor wires had to be fed through the location where the 8th bolt hole would have been placed. It was imperative that enough clamp force was generated by the motor fasteners so that bolts would not have to withstand the large shear force caused by the small center radius of the M8 bolt pattern. The upright coupler featured a larger inner diameter so that the motor shaft could fit inside the upright coupler. A long M16 bolt fastened the motor to the upright coupler through the center hole to increase the tensile force connecting the two parts. Bending at the motor bolts was also a concern because the bolts would have to withstand the static and dynamic vertical loads of the 45 kg motor and wheel assembly.

The maximum tensile forces in the motor connecting bolts were calculated for the outside wheel in the case where the vehicle is cornering at 1 g of lateral acceleration. In this case, the lateral force at the contact patch is pushing the wheel into the upright. Therefore, the moment about the x-axis caused by the vertical force at the contact patch was the primary load inducing a bending stress into the connection between the motor and the upright coupler. Seven M8 bolts and one M16 bolt was used to connected the coupler to the motor. First, the forces and moments acting on the shared face of the motor and upright coupler were found. Then, the tensile stresses in the eight bolts were determined using the equation for bending stress (eq. 6.6). The distance from the local x-axis to the farthest edge of the bolt, c, varied depending on the bolt location. The area moment of inertia about the x-axis, I_x, was calculated for only the bolt cross-section so that a worst case scenario where only the bolts handle the bending moments would be assumed.

$$\sigma_{bend} = \frac{M_x c}{I_x} \tag{6.6}$$

The tensile force in each bolt was found by multiplying the bending stress at the bolt by it's area (eq. 6.7). The bolt with the maximum tensile force was chosen for further analysis [9].

$$P = \sigma_{bend} A_{bolt} \tag{6.7}$$

To hold the bending moment, the fastened interface between the motor and the upright coupler had to be strong enough to resist bolt failure and joint separation. The factors of safety against bolt failure and joint separation are shown in equations 6.8 and 6.9 [9]. The preload force in the bolt was found using equation 6.2 as described in the previous section. The bolt and member stiffnesses (k_b and k_m) were determined using equations 6.10 and 6.11, respectively [9]. The clamped zone to calculate the member stiffness was aproximated by a frustum of a cone with a half-apex angle, α, of 30°. Once the bolt and member stiffnesses were known, the stiffness ratio, C, could be found using equation 6.12 [9].

$$n_b = \frac{S_p A_t - F_i}{CP} \tag{6.8}$$

$$n_m = \frac{F_i}{(1 - C)P} \tag{6.9}$$

$$k_b = \frac{A_d A_t E}{A_d l_d + A_t l_d} \tag{6.10}$$

$$k_m = \frac{\pi E d \tan\alpha}{2 \ln \frac{(l \tan\alpha + d_w - d)(d_w + d)}{(l \tan\alpha + d_w + d)(d_w - d)}} \tag{6.11}$$

$$C = \frac{k_b}{k_b + k_m} \tag{6.12}$$

These factors of safety were calculated for the M8 bolt with the maximum tensile force and the center M16 bolt. The center bolt had factors of safety greater than 4. Whereas the M8 bolt had a bolt failure factor of safety of 4.17, and a joint separation factor of safety of 1.62. Given the assumptions made, a factor of safety of 1.62 was deemed acceptable. A similar bolt tension analysis was completed for the six bolts at the upright and upright coupler interface resulting in safety factors above 1.70.

6.3 Upright

The upright was a complicated part to design as it had to connect all of the outboard joints to the wheel assembly. The upright connected to the upright coupler via six 1/4" bolts in a circular pattern. They had to have a large enough center radius so that the bolts connecting the upright coupler to the motor could be accessed with a tool, and allow the motor wires to be routed through the center of the upright. The upright connected to the outboard cross cylinder joint by a welded, steel mount. The upright coupler, upright and outboard cross cylinder mount were made in three separate parts, as opposed to one part, to reduce machining time, scrap material and cost. The caliper bolted to the upright through two 3/8" bolts. The outboard upper control arm ball joint had a tapered stud with a nut and washer. To accommodate the stud, a taper was machined into the upright and a flat surface for the nut and washer was incorporated into the design.

The outboard joints on the rear cylinder and fixed-length link could not be supported in double shear due to size constraints on the upright. They also had to screw into the upright. The preload torques for the bolts were determined using equations 6.2 and 6.3 presented in section 6.1. However, shear of the internal threads was investigated. Equation 6.13 determined the equivalent tensile area of the internal threads [3]. The tensile area was a function of the thread pitch, p, length of the engaged threads, L_e, minimum major diameter of the external threads, D_{min}, and the maximum pitch diameter of the internal threads, E_{max}. The factor of safety against internal, aluminum thread shear was calculated, knowing the aluminum shear strength, S_u, internal thread tensile area, A_t, and the maximum tensile force, $F_i + \Delta F_{max}$ (eq. 6.14).

$$A_t = \pi p L_e D_{min} \left(\frac{1}{2p} + 0.57735(D_{min} - E_{max}) \right) \tag{6.13}$$

$$n_{thread} = \frac{S_u A_t}{F_i + \Delta F_{max}} \tag{6.14}$$

A finite element analysis was performed on the upright using SolidWorks. To increase the accuracy of the model, the simulation was executed on an assembly including the upright as opposed to just the upright. All parts other than the upright were assumed to be rigid. The part containing the bolts connecting the upright to the upright coupler was fixed. The forces were applied to the upper control arm, rear cylinder and link studs, and the outboard cross cylinder bracket. Three load cases were analyzed. The first two load cases examined the forces in the suspension components during a 1 g lateral acceleration turn in two separate configurations. The third load case investigated a 1 g longitudinal deceleration for locked braking.

The forces in the first and second load cases were determined from the analysis completed in section 5.5.1 (fig. 5.9 & 5.10). Two corner module configurations were simulated: 15° steer, 0° camber and 15° steer and −15° camber. A steer angle of 15° was selected because it resulted in the maximum load case. It was expected for the maximum load case to occur at a positive steer angle because this indicated that it was the outside wheel during a cornering maneuver. 0° and −15° camber were selected to check the different

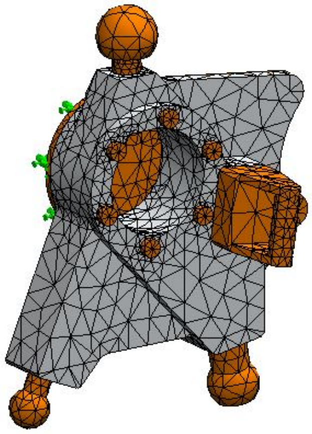

Figure 6.2: Upright with mesh, fixture (green) and rigid parts (orange).

camber settings. The directions of the forces were also accurately modeled depending on the configuration under observation.

The connection assumptions were the same for all simulations. The connection assumption for the rear cylinder and link studs were set to bonded with the upright. This assumption was chosen because these studs were threaded into the upright with threadlocker. The remaining parts were connected to the upright under the assumption that no penetration could occur. This condition was set for every face that was coincident with a face on the upright. Therefore, bolt preload forces were not included in these simulations. A curvature based mesh was used in all simulations. The simulations had a minimum element size of 3.82 mm and a maximum mesh size of 19.1 mm with a total of 38971 nodes (fig. 6.2).

The maximum von Mises stress that developed in the first load case was 214 MPa (fig. 6.3a). It occurred at the lowest upright coupler bolt hole beneath the bolt head. This maximum stress resulted in a factor of safety of 1.29, therefore, this load case could be endured by the upright. The maximum deflection occurred at the outboard fixed-length link stud (fig. 6.3b). The resulting deflection was 0.42 mm. This was acceptable as

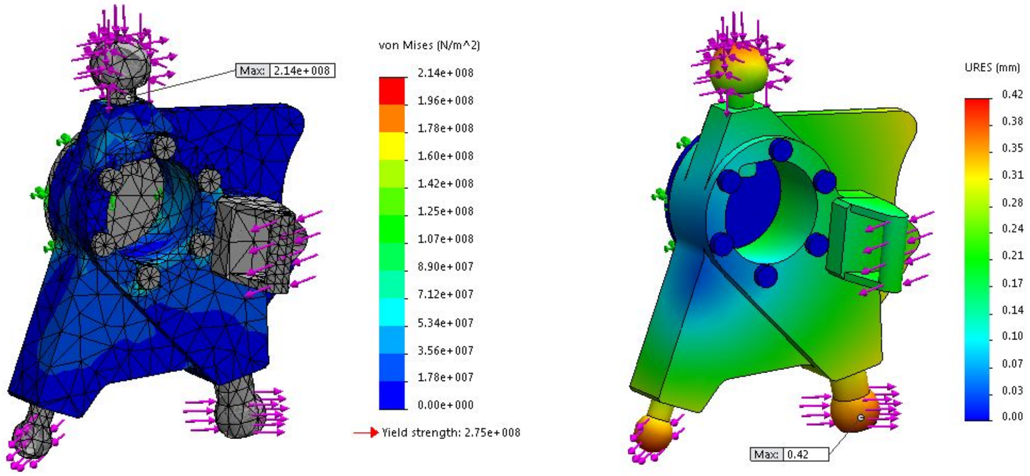

(a) Von Mises stress [N/m^2].

(b) Resultant deflection [mm].

Figure 6.3: Upright simulation results for load case 1: 1 g lateral acceleration at 15° steer and 0° camber.

component interference was not a concern for such a small deflection. The outboard cross cylinder mount also deflected, but only by approximately 0.21 mm. Again, this small of a deflection was not a concern for the operation of the corner module.

The second load case resulted in a higher maximum stress and maximum deflection than the first load case. The lateral force at the outboard upper control arm joint and the forces in the rear cylinder and link were greater in the second load case. The directions of the forces in the link and cylinders also changed because the corner module was cambered $-15°$. The maximum von Mises stress occurred at the outboard upper control arm stud (fig. 6.4a). The maximum stress was 239 MPa. This resulted in a factor of safety of 1.15. Although this factor of safety was very low, the load case in which the vehicle experiences 1 g of lateral acceleration is highly unlikely due to the operational driving conditions. Therefore, the design was deemed acceptable. For this load case, the outboard rear cylinder stud had a maximum resultant deflection of 0.95 mm (fig. 6.4b). No interference would occur in the event of a 0.95 mm deflection at this location.

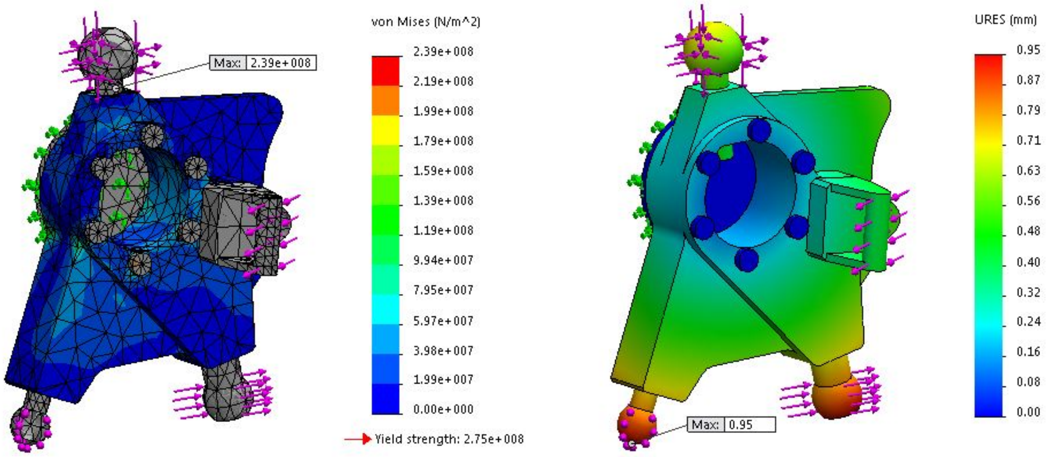

(a) Von Mises stress [N/m^2]. (b) Resultant deflection [mm].

Figure 6.4: Upright simulation results for load case 2: 1 g lateral acceleration at 15° steer and −15° camber.

In the third load case, the forces were applied to two rigid bolts which would connect the caliper to the upright. There were only x- and z-component forces acting at each bolt. The forces acting on the caliper bolts were assumed to be equally distributed. To reduce the computation time, the static forces acting on the mounts and studs were assumed negligible. The maximum von Mises stress developed in the top caliper bolt with a value of 105 MPa (fig. 6.5a). This resulted in a factor of safety of 2.6 (fig. 6.5b). The maximum deflection occurred at the outboard fixed-length link stud with a value of 0.88 mm. Similar to the previous load cases, the maximum resultant deflection was not enough to cause an interference between the fixed-length link and other components.

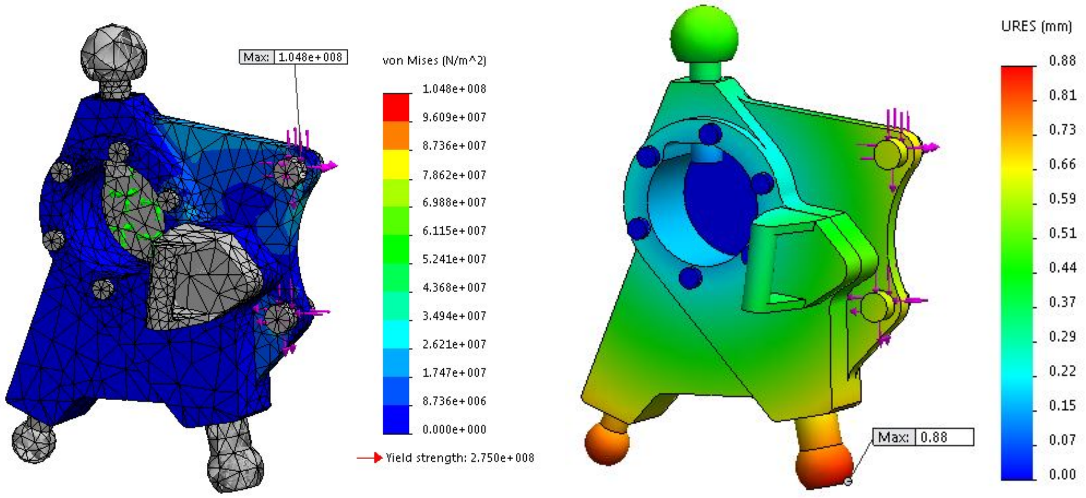

(a) Von Mises stress [N/m^2]. (b) Resultant deflection [mm].

Figure 6.5: Upright simulation results for load case 3: 1 g longitudinal deceleration with locked braking.

6.4 Upper Control Arm

Upper control arms are typically produced in high volumes and are manufactured by casting or stamping with post-process machining. However, such processes were unavailable for this project as they would be too expensive to fabricate a single part. The upper control arm was welded together using sheetmetal and tubes (fig. 6.6). The upper control arm connected the outboard ball joint, inboard bushings and the outboard damper rod end to one another. The locations of these joints were already known from the hard point optimization, bump camber design and motion ratio selection (sections 4.4, 5.1 and 5.3). A mount for the rotary sensor that measured ride height was also welded to the upper control arm.

The outboard ball joint sleeve was rotated out of the upper control arm's cross-sectional plane to prevent interference between the outboard ball joint's housing and stud. The outboard ball joint was selected due to its very high misalignment angle of 64°. How-

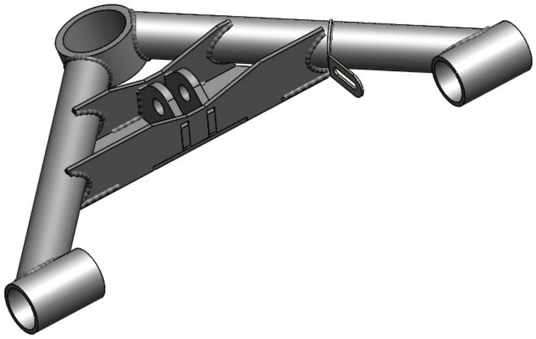

Figure 6.6: Final design of the left front wheel's upper control arm.

ever, the outboard ball joint had to be rotated out of plane because the wheel's spin angle increases drastically as the camber angle is increased (fig. 4.9). Therefore, the centerlines of tubes connected the inboard bushing housings to the outboard sleeve could not be in the same plane.

A finite element analysis was performed on the damper mount that would connect to the bracing tubes (fig. 6.7). This analysis assumed that the bracing tubes were rigid and the welds connecting the mount to the tubes would not fail. Therefore, the damper mount was fixed at the tube weld seams. A 5 kN force was applied to a rigid bolt in the center of the mount. A no penetration connection was the condition assumed for the bolt and the mount. No preload force from the bolt was applied to the mount. The locations of high stress on the mount occurred in the center of the C-channel where the height of the vertical plates reduces. Increasing the height of the vertical plates would have reduced the stress, but then interference would occur between the damper mount and damper rod end. The maximum stress at these locations was well below the yield stress of the steel plates, therefore, the design was determined to be acceptable for the prototype corner module.

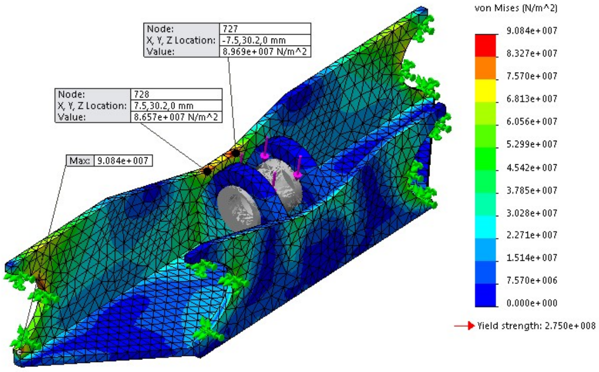

Figure 6.7: Von Mises stress (N/m^2) developed in the upper control arm damper mount.

6.5 Fixed-Length Link

The link design had to incorporate a two-force member with spherical joints at either end (fig. 6.8). Loads to be considered in the design were the maximum compression and maximum tension forces that would develop in the link. The link was composed of a tube with tube adapters on either end to fasten to the rod ends. Although the link was expected to withstand a maximum tensile force of 10 kN and a maximum compressive force of approximately 7 kN, it's design was constrained by the outboard rod end. The upright could only support outboard spherical joints in single shear as opposed to double shear. Therefore, a rod end with a stud was required for the outboard link joint. However, studded rod ends are generally weaker in radial loading as compared to rod end that are supported on both sides of the ball. A 3/4" rod end with a stud was the smallest studded rod end that could support the 10 kN tensile load. Therefore, a tube outer diameter of 1.25" with a wall thickness of 0.095" was required for the 3/4" tube adapter. The link design was also inspected for buckling failure (eq. 6.15) and tensile failure, however, due to the outboard rod end, the factor of safety for both of these failure modes was greater

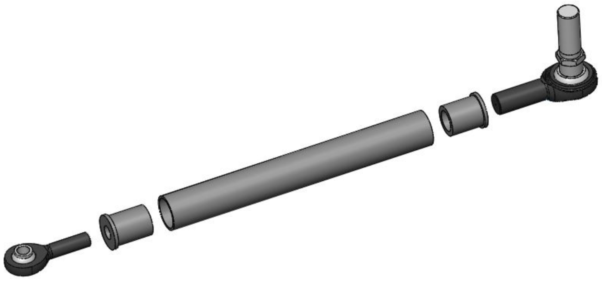

Figure 6.8: Exploded view of the fixed-length link assembly.

than 3.

$$F_{crit} = \frac{\pi^2 EI}{L^2} \tag{6.15}$$

6.6 Mounts

There were a variety of mounts to be designed for this corner module as there were six inboard joints and one outboard joint requiring mounts. The preload forces and torques in the bolts were determined using equations 6.2 and 6.3, respectively. After the preloads were found, each bolt was inspected for sleeve yield in compression and sleeve slip in shear. The compressive stress in the sleeve was found using the preload force and the cross-sectional area of the sleeve (eq. 6.16). Dividing the sleeve yield strength by the compressive stress resulted in the factor of safety against sleeve yielding (eq. 6.17). The factor of safety against the sleeve slipping as a result of the maximum shear force exerted on the bolt was determined using the preload force and the coefficient of friction between the sleeve and mount surfaces. Mostly, the sleeve and mount surfaces were steel so the coefficient of friction was assumed to be 0.5. The safety factors are summarized in table 6.1.

$$\sigma_i = \frac{F_i}{\frac{\pi}{4}(d_o^2 - d_i^2)} \tag{6.16}$$

Table 6.1: Safety factors against sleeve yield and sleeve slip for various joints.

Bolt Description	Sleeve Yield FoS	Sleeve Slip FoS
7/16 Cylinder Bolts	1.31	1.48
7/16 Link Bolt	1.43	2.22
1/2 Shock Shoulder Bolts	2.23	3.07
5/8 UCA Shoulder Bolts	1.52	2.81

$$n_{sy} = \frac{S_y}{\sigma_i} \tag{6.17}$$

$$n_{ss} = \frac{\mu F_i}{F_{max}} \tag{6.18}$$

Bolts were also checked for failure in the case of a shear load (in the case of sleeve slip). The various failure modes included bolt shear, bolt bending, member tensile tear-out, member bearing and member shear tear-out (eq. 6.19 to 6.23). Each of the stress cases were compared to either the material yield strength for normal stress or material shear strength for shear stress to determine the respective factors of safety.

$$\tau_b = \frac{F}{2\pi r^2} \tag{6.19}$$

$$\sigma_{bend} = \frac{Mr}{I} \tag{6.20}$$

$$\sigma_t = \frac{F}{2w_{min}t} \tag{6.21}$$

$$\sigma_b = \frac{F}{2dt} \tag{6.22}$$

$$\tau_t = \frac{F}{2et} \tag{6.23}$$

6.6.1 Outboard Cylinder Mount

The tensile forces in the bolts connecting the outboard cylinder mount to the upright were large due to the limited packaging space to increase the leverage distance. The upright

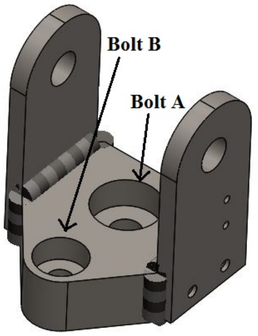

Figure 6.9: Outboard cylinder mount showing the locations of bolt A and bolt B.

connecting bolts were selected based on a maximum cross cylinder tensile load of 10 kN. Under this condition, a tensile load of 19 kN developed bolt B and a compressive load of 19 kN developed in bolt A (fig. 6.9). Bolt A was not investigated for bolt failure or joint separation because a compressive load was applied to bolt A. The bolt stiffness for bolt B was calculated using equation 6.10. The outboard cylinder mount was made of 1045 steel, and the upright was composed of 6061-T6 aluminum. Therefore, the member stiffness was found by determining the individual stiffness of each material and treating them as springs in series (eq. 6.24) [9]. Then, the factors of safety against bolt failure and joint separation could be found for bolt B (eq. 6.8 & 6.9). For an 8 mm shoulder bolt, the factor of safety against bolt failure was 1.76 and the factor of safety against joint separation was 2.09.

$$\frac{1}{k_m} = \frac{1}{k_{steel,1}} + \frac{1}{k_{steel,2}} + \frac{1}{k_{Al,1}} + \frac{1}{k_{Al,2}} \tag{6.24}$$

To prevent the bolts from experiencing any shear load, an M10 bolt was used for bolt A. The preload force exerted by this bolt would supply a sufficient friction force between the steel and aluminum to prevent the outboard cylinder mount from slipping with respect to the upright. A friction coefficient of 0.6 was assumed for the steel and aluminum surfaces. This resulted in a factor of safety of 2.53. Even if the coefficient of friction was 0.3, the factor of safety would be 1.27 for this extreme case.

The shear stress at the welds that joined the side plates to the base of the outboard cylinder mount were also inspected for failure. The factor of safety against weld failure were calculated for a fillet weld with a rectangular cross-section and a fillet weld with a C-channel cross-section. The maximum shear stress would occur at the corners of the weld cross-section. The shear stress at each corner was determined by resolving the pure shear stress and torsional stress components for each corner (eq. 6.25 & 6.26). The allowable shear stress for a weld is less than one third of the material shear stress as authorized by the AISC code for weld metal [9].

$$\tau_{shear} = \frac{V}{2A} \tag{6.25}$$

$$\tau_{tor} = \frac{Tc}{2J} \tag{6.26}$$

The dimensions of the two cross-sections remained the same, but their areas and polar moments of inertia were different (eq. 6.27 to 6.30) [9]. The factor of safety for the rectangular cross-section was 2.06 and the factor of safety for the c-channel cross-section was 1.49 (eq. 6.31). The rectangular cross-section was chosen for the weld pattern in the outboard cylinder mount for its higher factor of safety.

$$A_R = 1.414t(h+w) \tag{6.27}$$

$$J_R = 0.707t\left(\frac{(h+w)^3}{6}\right) \tag{6.28}$$

$$A_C = 0.707t(2h+w) \tag{6.29}$$

$$J_C = 0.707t\left(\frac{8h^3+6hw^2+w^3}{12} - \frac{h^4}{2h+w}\right) \tag{6.30}$$

$$n_{weld} = \frac{0.3S_u}{\tau} \tag{6.31}$$

6.6.2 Inboard Cylinder Mount

The inboard cylinder mount fastened the rear cylinder and the cross cylinder to the back plate. One mount was designed instead of one mount per cylinder because the inboard

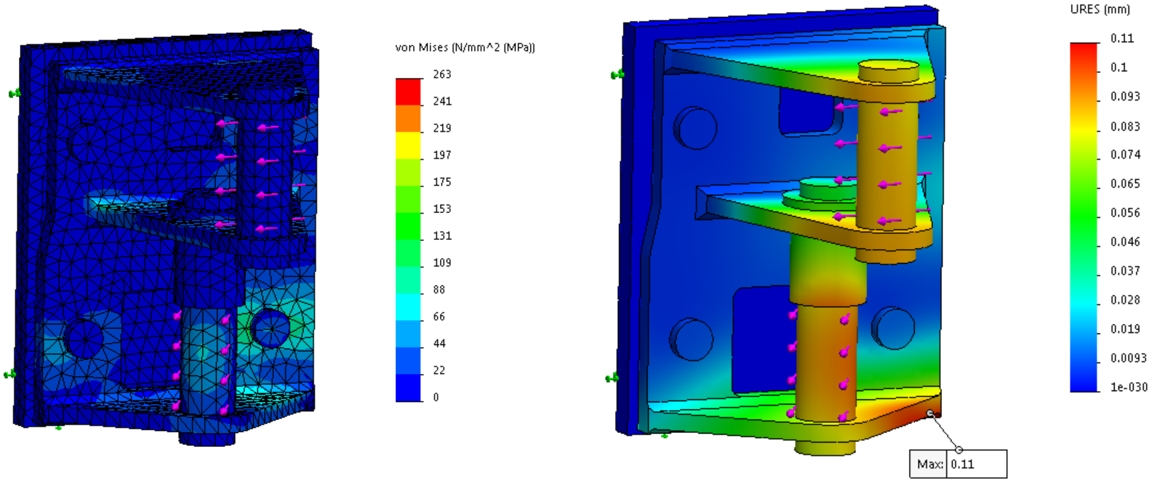

(a) Von Mises stress [N/mm^2]

(b) Deflection [mm]

Figure 6.10: Inboard cylinder mount finite element analysis.

cylinder joints were close enough to one another to make one mount feasible. Clearance slots were placed in the base of the mount so that the back plate could be bolted to the frame. A slot pattern was also generated on the top plate so that a rotary sensor could be fastened to the mount.

Along with the sleeve failure calculations described previously, a finite element analysis was performed on the inboard cylinder mount. The load case used for the inboard cylinder mount was the same as the second load case used for the upright. A 1 g lateral acceleration was applied to the vehicle when the left wheel was steered 15° and cambered to $-15°$. This load case generated a 7.8 kN tensile load in the rear cylinder and a 2.8 kN tensile load in the cross cylinder. The finite element analysis was executed on an assembly containing the inboard cylinder mount to increase the accuracy at the bolt connections. All parts other than the inboard cylinder mount were set as rigid. All contacting surfaces between the inboard cylinder mount and other parts had a no penetration condition. Bolt preload forces were not considered in this simulation. The rigid part modeling the back plate and its bolts was fixed, and the cylinder loads were applied to the rigid bolts. The mesh size for this simulation was curvature based. The maximum von Mises stress that developed in the inboard cylinder mount was 263 MPa. The factor of safety for this load case was 1.33. The maximum deflection that occurred in the mount was 0.11 mm. The factor of safety and maximum deflection were deemed acceptable for this worst case scenario.

6.6.3 Shock Mount

Due to the limited packaging constraints set by the frame design, the shock mount had to extend above the front portion of the frame. Fortunately, the shock did not exert any significant side load (longitudinal load in the vehicle assembly) on the mount. The shock mount side plates had to be separated enough to allow the shock absorber to rotate in between the mount as the wheel's vertical travel altered. A finite element analysis was carried out for a 5 kN impact load on the mount. Similar to the previous simulations, the parts other than the shock mount were made rigid with connecting surface condition of no penetration. Again, bolt preload was not accounted for in the simulation. The back plate was fixed, and the load was applied to the rigid bolt. The shock mount had a maximum stress of 88 MPa which translated to a safety factor of 3.97 (fig. 6.11a). The maximum deflection occurred at the inboard shock bolt with a value of 0.25 mm (fig. 6.11b). The safety factor and maximum deflection were more than acceptable for the worst case scenario. Although the shock mount could have been designed using less material and still have a safety factor greater than 1.5, the final designed was approved. The design was for was prototype, therefore, it was more important to validate the concept than to reduce the weight of the corner module.

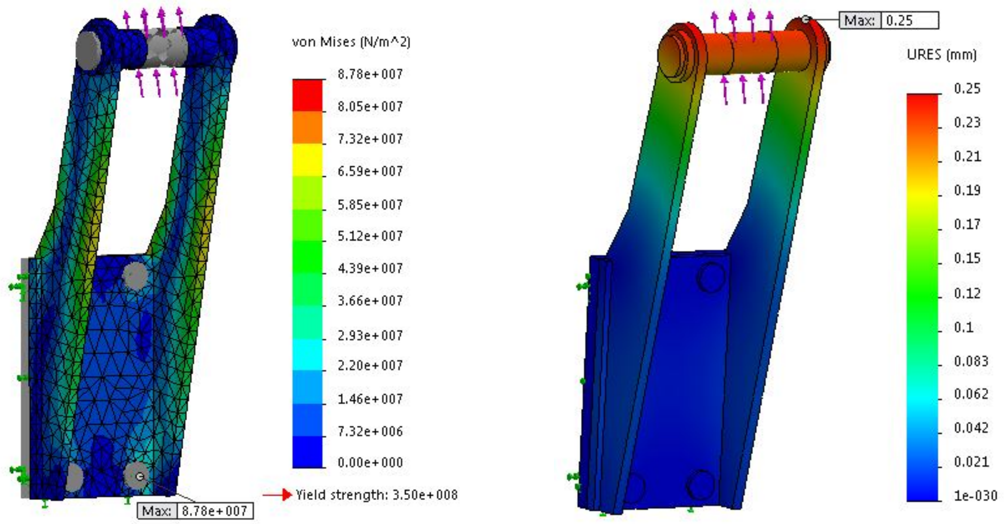

(a) Von Mises stress [N/m^2] (b) Deflection [mm]

Figure 6.11: Shock mount finite element analysis.

Chapter 7

Fabrication and Experimental Testing

7.1 Fabrication

Before the detailed drawings of the corner module components were sent out for manufacturing, a scaled prototype was fabricated to validate the motion of the corner module. To expedite the prototyping process, the scaled model was made using a 3D printer (fig. 7.1). The corner module assembly was simplified so that the assembly could be printed by the 3D printer without any assembly required after printing. Holes were added to the moving interfaces so that the filler material could escape from the enclosed parts such as the cylinders and shock absorber. Holes were also added to the ball joint housings for this purpose. Although the assembly was simplified, the hard points remained the same. Therefore, the motions of the scaled model were the same as those of the corner module.

The upright, rotor coupler and upright coupler were milled from 6061-T6 aluminum using a CNC milling machined (fig. 7.2). The inboard fixed-length link bracket was milled from 1045 steel because it was a relatively small part and the narrow packaging required a custom design. The outboard cross cylinder mount was also made from 1045 steel. The


(a) Front view (b) Side view

Figure 7.1: 3D printed, scaled model of the corner module.

bracket was milled because it was made in three parts to reduce manufacturing time and cost. Only the base of the outbaord cross cylinder mount required milling. The side brackets were made out of laser-cut sheetmetal. All milled parts were outsourced.

The shock mount, inboard cylinder mount, sensor mounts, upper control arm fixture and parts of the upper control arm were made from sheetmetal. In mass production, these parts would have been fabricated by cast or stamped. However, due to the low volume, welded sheetmetal was selected as the manufacturing process as it is inexpensive for low volume regardless of the complexity of the shape. The sheetmetal for the sensor mounts was bent and welded at the seam to achieve its shape because the thickness of the sheetmetal was thin enough to allow for bending. The bending operation was done in-house using a brake. All other sheetmetal parts were placed in a fixture and bolted together with spacers to locate the sheetmetal components with respect to one another. The laser cutting and welding was outsourced, but the sheetmetal assembly and tacking was completed in-house.

The upper control arm was constructed from sheetmetal and tubes. Tubes were used to connect the inboard bushings to the outboard ball joint. The tubes connecting the inboard

(a) Upright coupler.

(b) Upright.

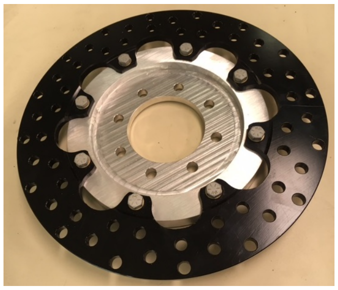

(c) Rotor coupler with rotor.

Figure 7.2: Milled aluminum components.

bushing housings and outboard ball joint sleeve were profiled so that the gaps between tubes would be minimized for welding. The inboard bushing housings were mounted to the fixture base using L-brackets. A steel bar was routed through both front and rear bushing housings to keep them concentric and prevent movement during welding (fig. 7.3). The outboard ball joint was a standard part selected for its high misalignment angle. The ball joint came with a threaded sleeve to be welded to the control arm (fig. 7.3b). The sleeve was connected to the fixture using a bent sheetmetal mount to achieve the location and orientation of the sleeve with respect the inboard bushings. This fixture mount was pressed into the sleeve to prevent movement and deformation of the sleeve during welding. The location of the shock mount was also located using the fixture to ensure that the motion ratio would not change. Figure 7.4 shows the side and front views of the suspension and

(a) Upper control arm fixture.

(b) Outboard ball joint sleeve.

Figure 7.3: Upper control arm assembly welding.

steering systems of the corner module fully assembled when it is mounted to the frame. To better view the different members, the wheel is not mounted to the upright in the figure. The corner module was assembled with ease once all of the components were built.

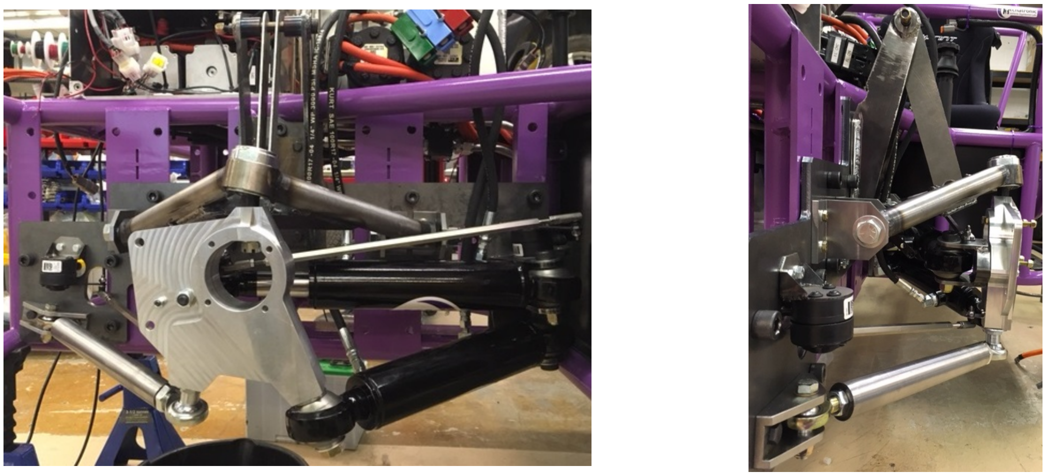

(a) Side view

(b) Front view

Figure 7.4: Final assembly of the steering and suspension system for the corner module.

7.2 Sensor Calibration

Three rotary sensors were used to determine the orientation of the wheel and subsequently the lengths of the cylinders. All three rotary sensors were fixed to the vehicle frame. Two of the sensors were connected to the upright using a fixed-length link with two spherical joints for each sensor. The vertical travel of the wheel was measured by connecting one of the rotary sensors to the upper control arm (fig. 7.5). This sensor was titled the ride height rotary sensor as it would relay information regarding the instantaneous length of the shock absorber and the instantaneous location of the outboard upper control arm spherical joint. The other two sensors were called the front and rear rotary sensors based on their position on the left side corner module. The front and rear rotary sensors would sense the steer and camber angles of the wheel. The ride height rotary sensor was decoupled from the steer and camber motions of the wheel. However, the front and rear rotary sensors were not decoupled from the vertical wheel travel. Therefore, a 3-dimensional matrix was required to determine the orientation of the wheel for any combination of the sensor voltages.

The ride height sensor was easily calibrated to determine to position of the outboard upper control arm spherical joint using the known geometry of the upper control arm (fig. 7.6). The longitudinal position of the outboard upper control arm spherical joint remained constant. The vertical and lateral positions of the outboard joint changed with the position of the ride height sensor (fig. 7.7). Equations 7.1, 7.2 and 7.3 are the calibration equations relating the sensor voltage to the angle, and the z- and y-components of the outboard joint.

$$\theta_{RH} = -28.762V_{RH} + 140.24 \tag{7.1}$$

$$S_z = z_o + h\cos\theta_{RH} = 341.78 + 191.5\cos\theta_{RH} \tag{7.2}$$

$$S_y = y_o + h\sin\theta_{RH} - h\sin\theta_{RH,o} = -149.5 + 191.5\sin\theta_{RH} - 191.5\sin(69.72) \tag{7.3}$$

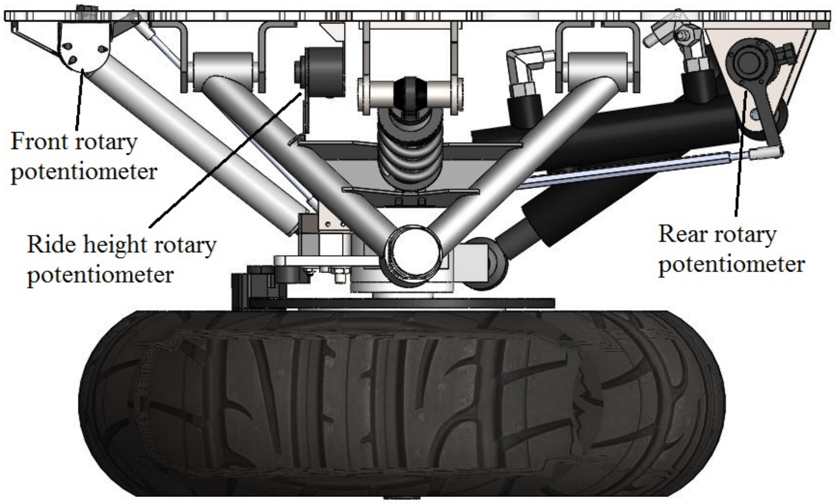

Figure 7.5: Top view of the left side corner module showing the front, rear and ride height rotary potentiometers.

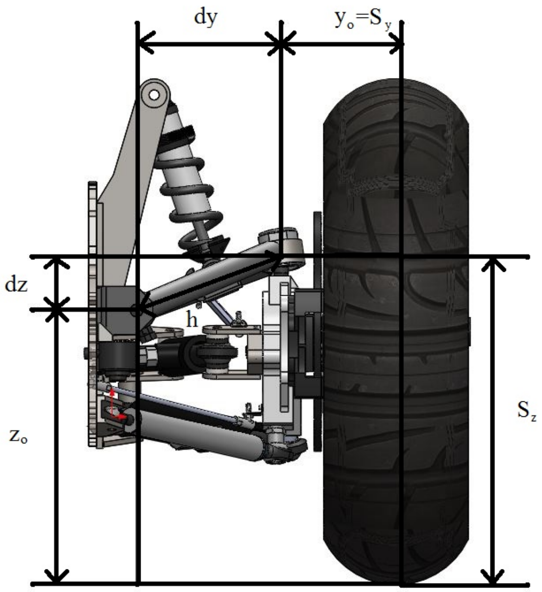

Figure 7.6: Ride height sensor geometry.

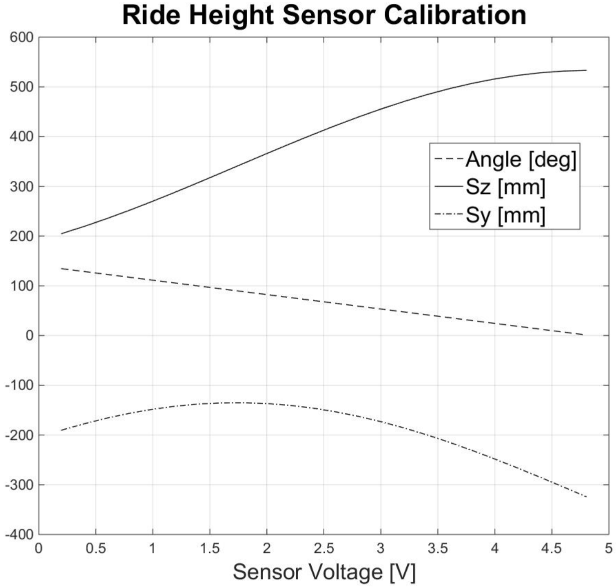

Figure 7.7: Ride height sensor calibration curves for the angle between h and dz, and the z- and y-components of the outboard upper control arm joint.

The forward kinematic model was used to determine the steer and camber angles of the wheel from the front and rear sensors. However, instead of the length of two of the links changing, the inboard joints on two of the links move about a fixed circle while the link lengths remain constant. Before the wheel orientation could be determined, the locations of the inboard joints connected to the sensors had to be found. The process of finding the inboard joint locations of the sensors was the same for both sensors. The fixed origins, $\boldsymbol{O}$, reference vectors, $\boldsymbol{v_{ref}}$, distances from the origin to the ball joint stud, l, and normal vectors of the planes containing the reference vector and inboard joint vector, $\hat{\boldsymbol{n}}$, of both sensors were known (fig. 7.8). Given the sensor voltage, the angle of rotation could be calculated using equations 7.4 and 7.5 for the front and rear sensors, respectively.

$$\theta_F = 28.762V_F + 17 \tag{7.4}$$

$$\theta_R = 28.762V_R + 212 \tag{7.5}$$

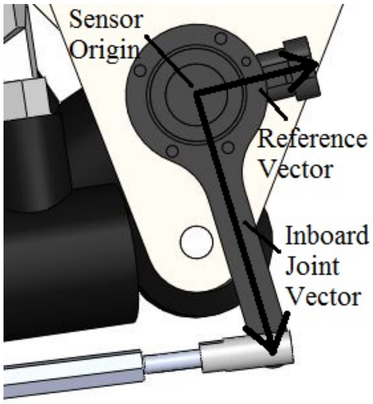

Figure 7.8: Rear sensor top view.

The angle of rotation about the normal axis and the normalized normal vector were used to find the rotation matrix of the inboard joint (eq. 7.6). The front and rear sensors' inboard joint instantaneous positions with respect to the parallel mechanism's fixed coordinate system were found using equations 7.7 and 7.8.

$$\boldsymbol{R_{sensor}} = \cos\theta \boldsymbol{I} + \sin\theta[\boldsymbol{\hat{n}}]_{\times} + (1 - \cos\theta)\boldsymbol{\hat{n}} \cdot \boldsymbol{\hat{n}} \tag{7.6}$$

$$\boldsymbol{LI} = \boldsymbol{O_L} + l_L(\boldsymbol{R_{sensor}}\boldsymbol{v_{ref}})_L \tag{7.7}$$

$$\boldsymbol{KI} = \boldsymbol{O_K} + l_K(\boldsymbol{R_{sensor}}\boldsymbol{v_{ref}})_K \tag{7.8}$$

The orientation and position of the wheel was found from the voltages of all three sensors. The ride height sensor revealed the position of the outboard upper control arm joint, $\boldsymbol{S}$. The front and rear sensors determined the positions of the inboard sensor link joints, $\boldsymbol{LI}$ and $\boldsymbol{KI}$, respectively. By using this information and the initial positions of the outboard sensor link joints, $\boldsymbol{LO_i}$ and $\boldsymbol{KO_i}$, the forward kinematic model was used to determine the steer and camber angles of the wheel. Then, the cylinder lengths could be determined by using inverse kinematics and the instantaneous orientation of the wheel. Figures 7.9 and 7.10 show the steer and camber angles of the wheel for any given front and rear sensor voltages when the wheel is in the ride height position (spring and damper have a length of 9.325 inches). Figures 7.11 and 7.12 show variations of the figures 7.9 and 7.10, but at different ride height sensor voltages. Figures 7.13 and 7.14 show the rear and cross cylinder lengths for any given front and rear sensor voltages when the wheel is in the ride height position.

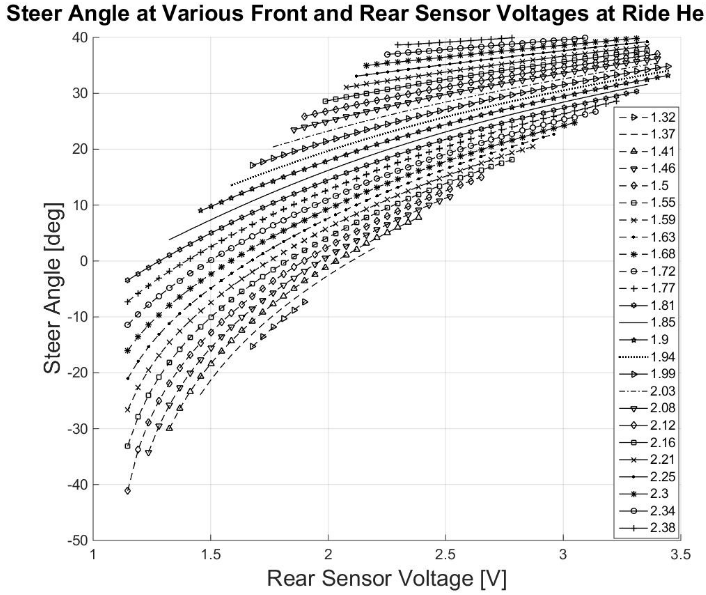

Figure 7.9: Steer angle for given front and rear sensor voltages at ride height.

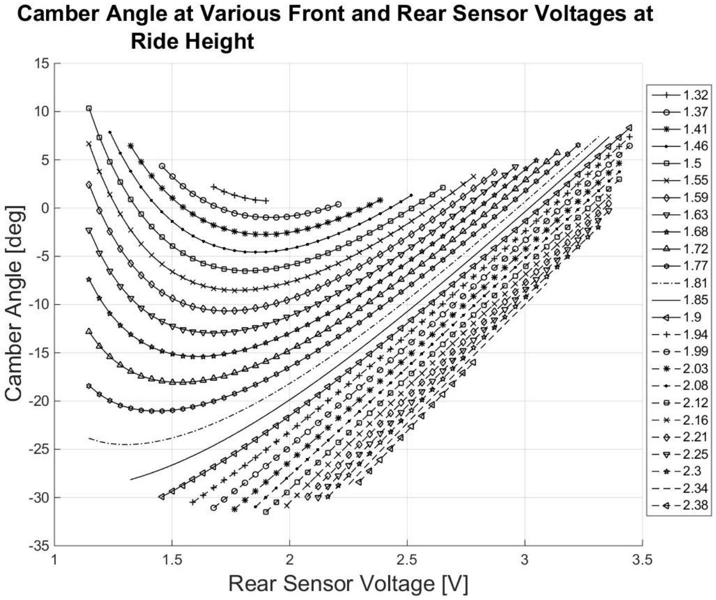

Figure 7.10: Camber angle for given front and rear sensor voltages at ride height.

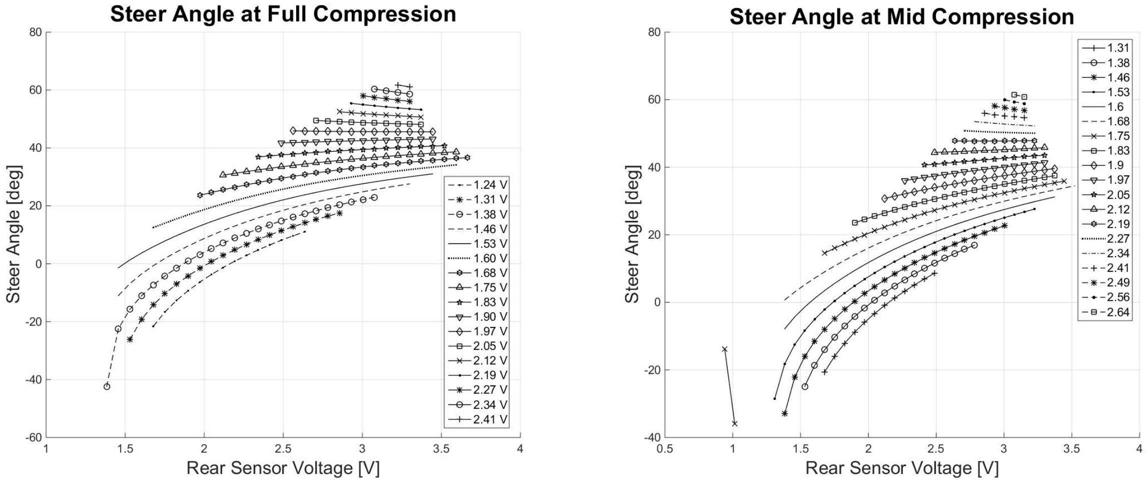

(a) Full compression

(b) Mid compression

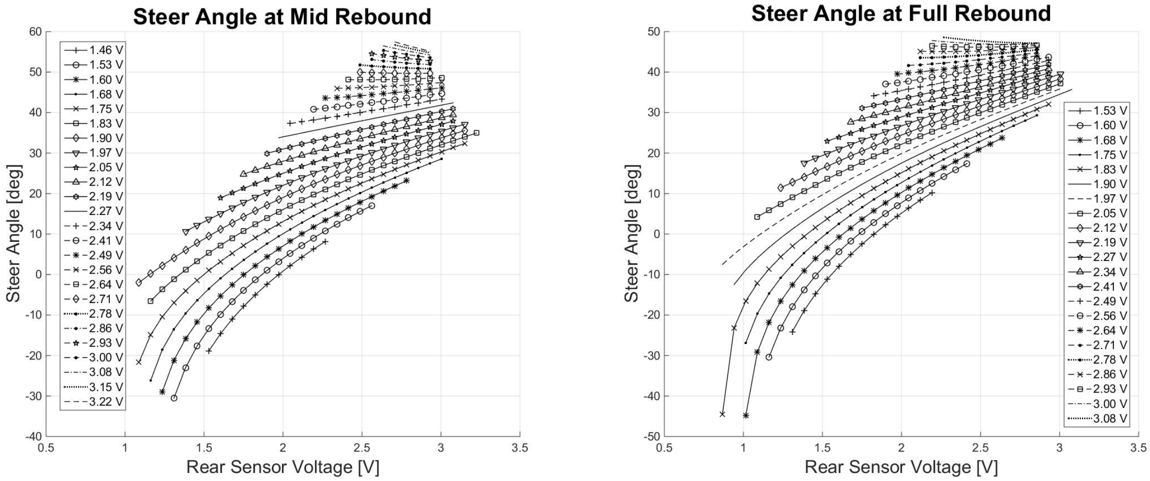

(c) Mid rebound

(d) Full Rebound

Figure 7.11: Steer angle as determined by the sensor voltages.

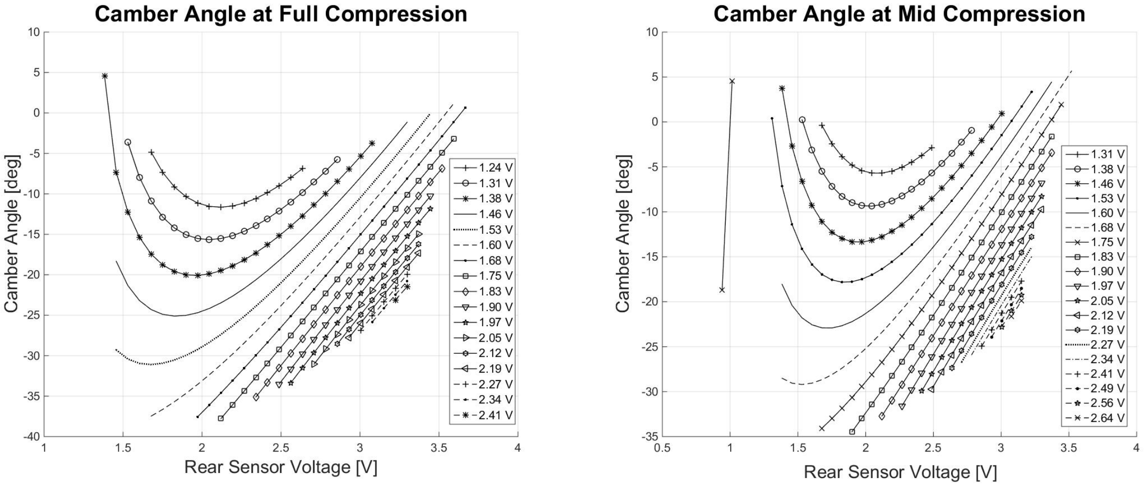

(a) Full compression (b) Mid compression

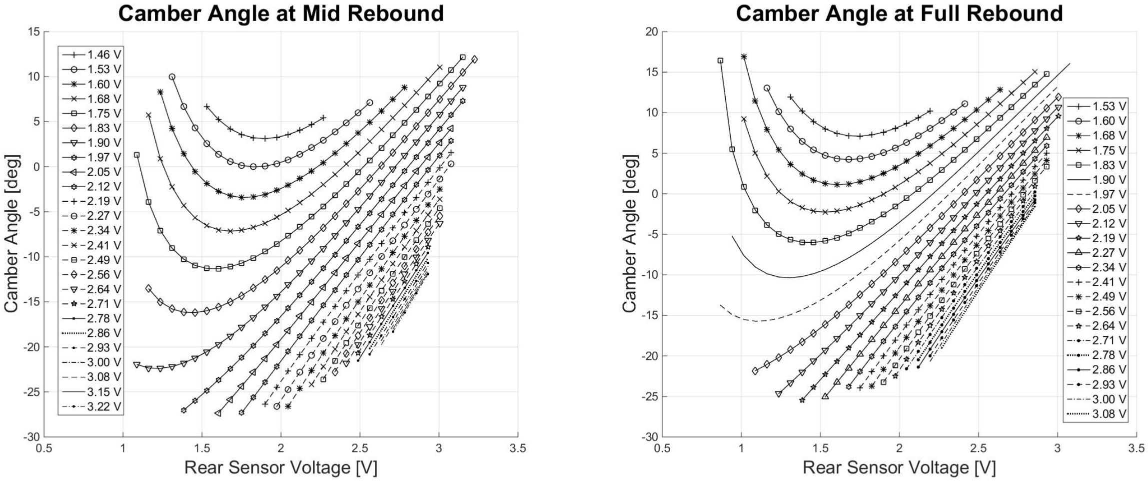

(c) Mid rebound (d) Full Rebound

Figure 7.12: Steer angle as determined by the sensor voltages.

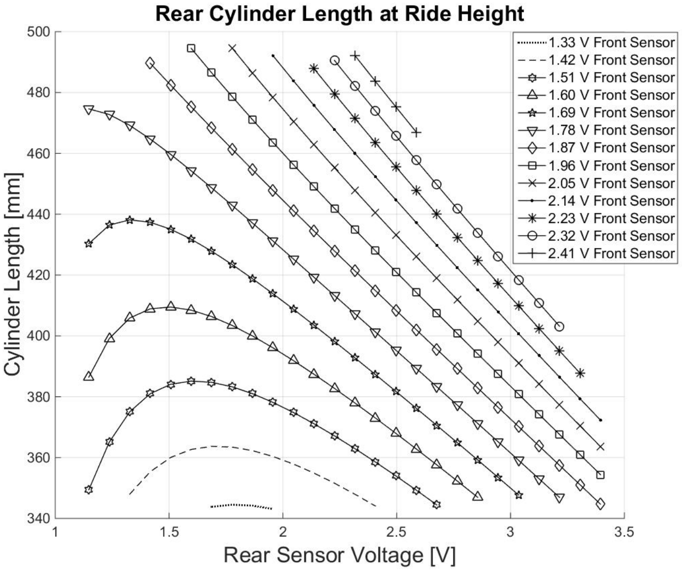

Figure 7.13: Rear cylinder length vs rear sensor voltage at ride height for constant front sensor voltage.

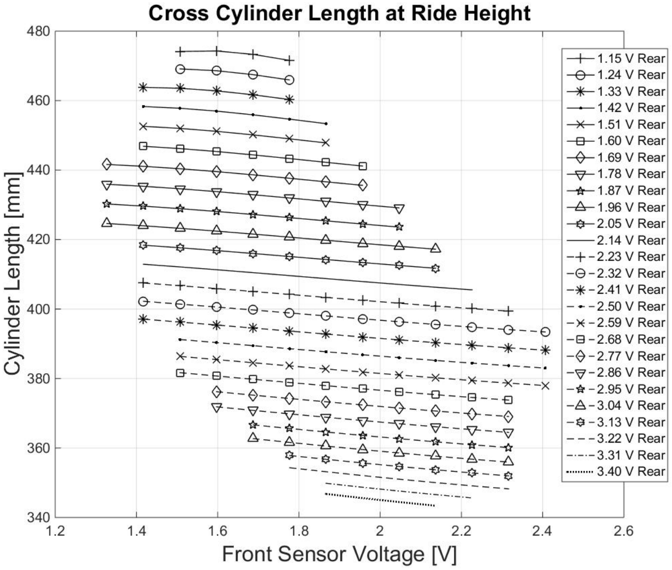

Figure 7.14: Cross cylinder length vs front sensor voltage at ride height for constant rear sensor voltage.

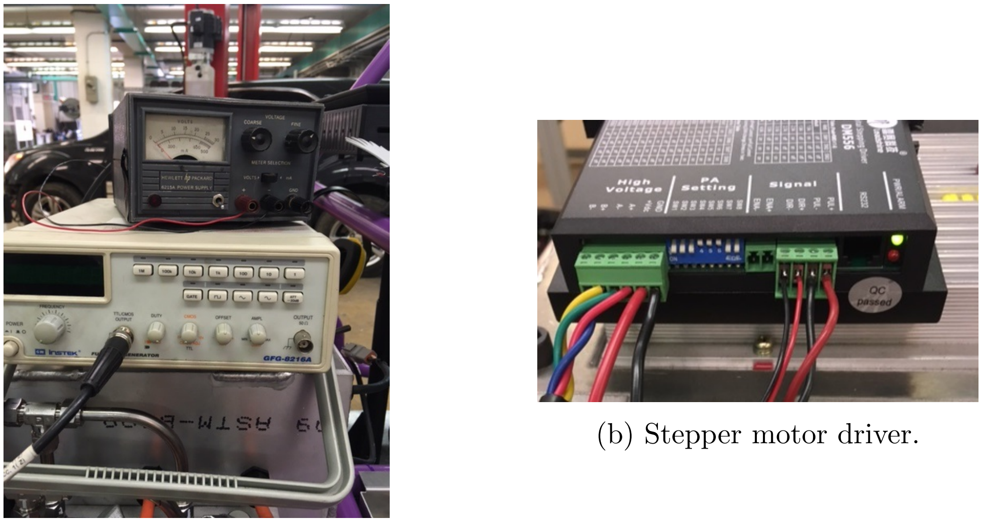

(a) 5V power supply and signal generator.

(b) Stepper motor driver.

Figure 7.15: Test equipment

7.3 Equipment

Various test equipment was required to control the corner module and measure its parameters. Testing of the corner module was completed while it was mounted to the vehicle frame. This was done so that the hydraulic system which was installed in the frame could be used to control the corner module. Besides the hydraulic system and the frame, a multimeter, 5V power supply, 12V battery, signal generator, line laser level, tape measure, protractor, 4 foot 90° angle and stepper motor driver were required for testing. The 5V power supply, signal generator and stepper motor driver are shown in figure 7.15. The signal generator provided a pwm signal to the stepper motor driver. When a signal was sent, the motor would cycle the valve which would cause the cylinder to extend or contract. The direction of the cylinder depended on whether a 5V signal was sent to the driver or not. The 5V power supply was connected to the driver and to the three sensors on the corner module. Unfortunately, a data acquisition system was not available for this test.

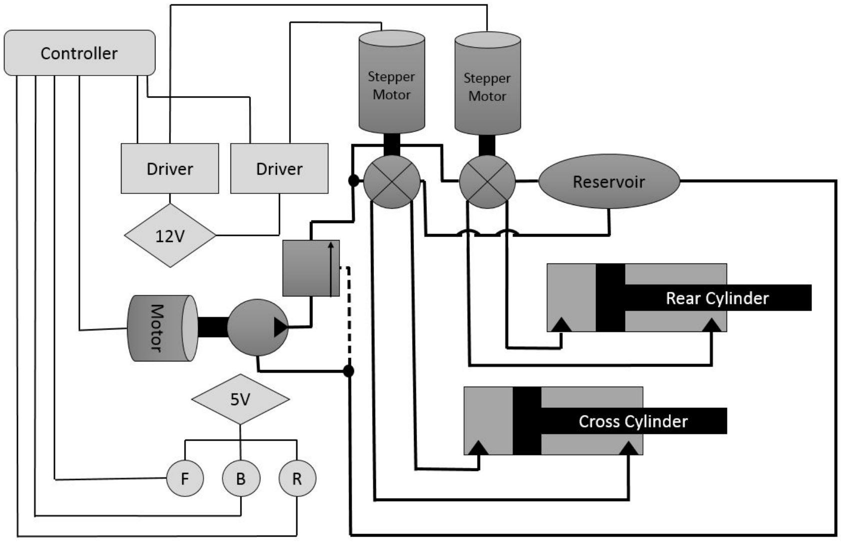

Figure 7.16: Control and hydraulic system diagram.

A multimeter was used to measure the voltage from the sensors. Figure 7.16 shows a diagram of the control and hydraulic systems for the corner module. The circled F, B and R represent the front, rear and ride height sensors, respectively. In the experiments, the controller was replaced with a multimeter and a signal generator.

7.4 Test Procedure

For the test, the corner module was not subject to any static load from the vehicle. The sensor voltages were recorded at the ride height, full compression and full rebound positions because the front and rear sensors were not decoupled from the ride height sensor (vertical wheel travel). The spring and damper were replaced with an adjustable rigid link to set the vertical travel of the wheel. A summary of the test procedure is listed below.

1. Move the suspension and the cylinders such that the corner module is in the ride height position at 0° steer and 0° camber.

2. Record the voltages for all three sensors and make a note that this is the nominal position so that the sensors can be zeroed when post-processing the data.
3. Move the suspension to the ride height position.
4. Move the rear cylinder to the desired length.
5. Move the cross cylinder to the desired length.
6. Record the voltages for all three sensors or report any component interference.
7. Measure and record the camber and steer angles.
8. Move the suspension to the full compression position.
9. Record the voltages for all three sensors or report any component interference.
10. Measure and record the camber and steer angles.
11. Move the suspension to the full rebound position.
12. Record the voltages for all three sensors or report any component interference.
13. Measure and record the camber and steer angles.
14. Repeat steps 3 to 13 for all desired cylinder lengths.

7.5 Experimental Results

The sensor voltages for all three sensors were successfully obtained from the experiment for different wheel orientations. The voltages were used to determine the actual steer angles, camber angles, cylinder lengths and wheel travel. Once the experimental data was post-processed, the forward kinematic model (appendix B.3) was used to calculated the

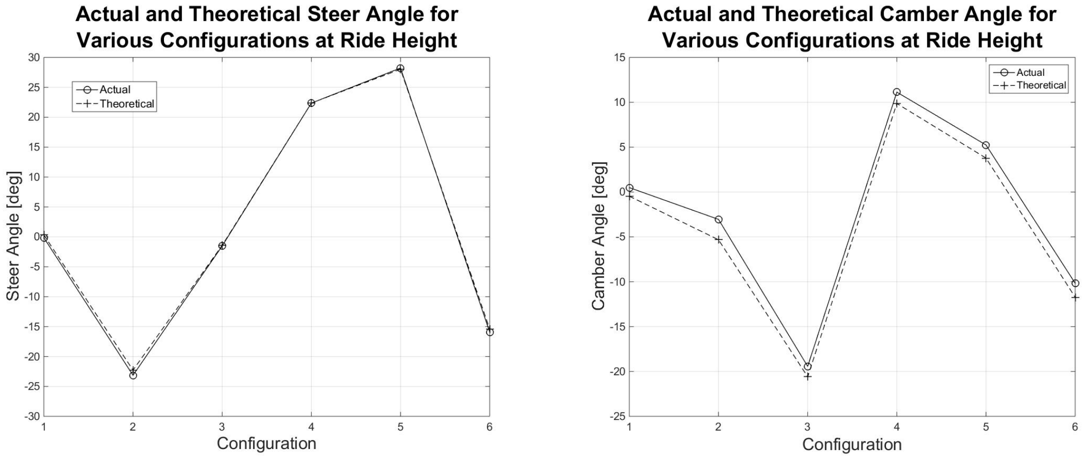

(a) Steer angle [deg]

(b) Camber angle [deg]

Figure 7.17: Actual and theoretical angles at ride height for various configurations.

theoretical steer and camber angles at each configuration measured in the experiment. The cylinder lengths and wheel travel found from the post-processed experimental data was used as the inputs to the forward kinematic model.

Table 7.1: Configurations examined in the experiment.

Configuration	**Steer Angle [deg]**	**Camber Angle [deg]**
1	-0.14	0.49
2	-23.14	-3.05
3	-1.52	-19.43
4	22.36	11.13
5	28.23	5.24
6	-15.91	-10.17

The configurations examined in the experiment were selected so that a wide range of steer and camber angles would be investigated. The configurations are shown in table 7.1. There were minor deviations between the actual and theoretical results. The theoretical steer angle calculation closely predicted the actual steer angle with an maximum deviation of 0.74° and a minimum deviation of 0.03° (fig. 7.17a). The theoretical camber

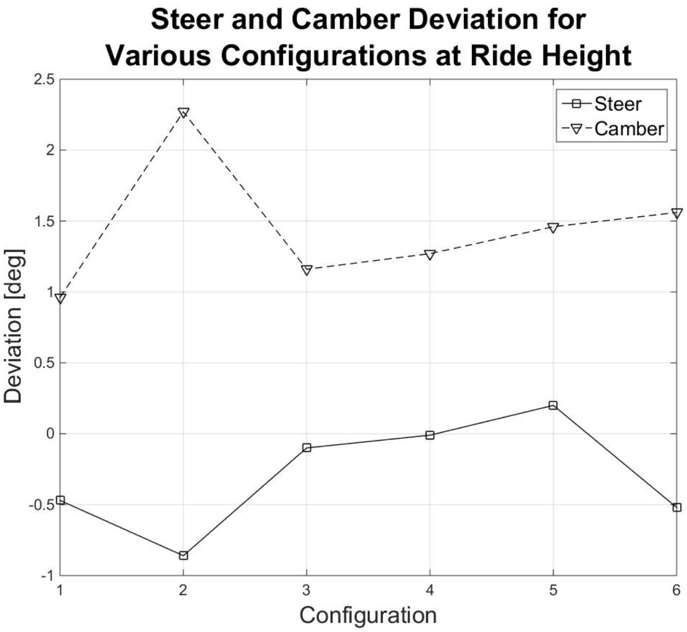

Figure 7.18: Steer and camber deviation at ride height for various configurations.

estimated the actual camber less accurately than the theoretical steer calculation. The maximum camber deviation was 2.25° which occurred in the second configuration. The minimum camber deviation was 0.96° (fig. 7.17b). The steer and cambers deviations for all configurations is shown in figure 7.18. Errors in the experimental data could have been caused by the differences between the computer generated model and the physical corner module. The theoretical data used the computer generated model to calculate the steer and camber angles given a combination of sensor voltages. Whereas the experimental data was calculated using sensor voltages that depended on the geometry of the physical corner module.

Chapter 8

Conclusion and Recommendations

8.1 Conclusions

A novel corner module concept was invented to resolve the handling instability and packaging challenges faced by narrow urban electric vehicles. This new corner module design was optimized to meet various objectives while remaining within the packaging and cylinder constraints. The optimized corner module exceeded the minimum steer and camber ranges. At 0° steer, its camber range was $-25°$ to $0°$. At 0° camber, its steer range was $-26°$ to $30°$. The mechanism met the lateral wheel travel target objective. The wheel traveled approximately 100 mm laterally at 0° steer and $-15°$ camber. The longitudinal wheel travel at 0° camber was minimized to 80 mm.

Both the Taghirad method and the Zlatonov method for determining the existence of singularities within a parallel mechanism's workspace were performed on the optimized corner module. The Taghirad method can only determine the existence of RI-type, RO-type and combined singularities whereas the Zlatonov method can find RI-type, RO-type, II-type, IO-type, RPM-type and IIM-type singularities. The Taghirad method found no singularities in the workspace while the Zlatonov method found II-type, IO-type and RPM-type singularities. The II-type, IO-type and RPM-type singularities existed throughout the entire workspace of the mechanism. These singularities existed because three redundant passive motions were added to the mechanism so that universal joints were not used in the final design. When these three additional degrees of freedom were removed from the mechanism, the Zlatonov method found no singularities in the workspace.

The bump camber and bump steer behaviours were specified for the corner module by selecting the locations of the inboard upper control arm joints and the cross cylinder. The bump camber was selected such that camber would be negative during spring compression and positive during spring extension. The bump steer was minimized by placing the cross cylinder such that its concentric axis intersected the instantaneous rotation axis of the wheel in the neutral position. The spring and damper were selected based on a two degree of freedom quarter car model. The caliper and rotor were sized to withstand 1 g of longitudinal deceleration given a maximum brake line pressure of 1500 psi. The forces in the various suspension components were determined for three different vehicle load cases: a longitudinal deceleration of 1 g with locked brakes, 1 g of lateral acceleration for various steer and camber angles, and a bump impact travelling at 100 km/hr. The suspension components were designed to withstand all three vehicle load cases.

A scaled version of the corner module was constructed using a 3D printer. The scaled model verified the general motions of the corner module, therefore, a full-scale corner module was built. The full-scale model was built using prototype manufacturing methods. Parts were either machined using a CNC mill and lathe, or they were welded together using sheetmetal and profiled tubes. The corner module was successfully assembled and then tested to validate the mathematical model. Test results showed that the mathematical model accurately estimated the steer angle within a maximum deviation of $0.74°$ and the camber angle within a maximum deviation of $2.25°$. The corner module presented in this thesis provides a viable solution to increase the feasibility of urban electric vehicles.

8.2 Future Work

Although the work successfully achieved the research goals, future work would be improved by implementing the following recommendations. As opposed to optimizing for pre-set corner module parameters, the optimization should have objectives describing the resulting vehicle performance and stability. The longitudinal wheel travel should be a packaging constraint instead of an objective, and the lateral wheel travel target should be described in terms of vehicle stability. The vehicle including the optimized corner module should be modelled in Adams/Car to provide a detailed analysis of the vehicle dynamics during multiple load cases.

The components in corner module were designed to be durable so that physical testing could be completed without concern for parts failing. However, that being said, there are components that could be redesigned to reduce the weight of the corner module. Also, the inboard fixed-length link rod end could potentially be replaced with a bushing because the fixed-length link rotates about a fixed axis when the shock absorber is fixed. The concentric axis of the bushing should be aligned with the rotation axis of the fixed-length link in the ride height position.

The front and rear rotary sensors could be replaced with linear sensors mounted on the cylinders. This would decouple the sensors from the vertical wheel travel, and significantly increase the accuracy of the sensor calibration tables. The stroke of the cylinders should be reduced so that the corner module has mechanical stops that will prevent component interference.

References

[1] *The Automotive Chassis*, chapter 3. Butterworth-Heinemann, 225 Wildwood Avenue, Woburn, MA 01801-2041, 2 edition, 2001.

[2] *The Automotive Chassis*, chapter 5. Butterworth-Heinemann, 225 Wildwood Avenue, Woburn, MA 01801-2041, 2 edition, 2001.

[3] Screw thread design. Technical report, Fastenal Company, 2009.

[4] World urbanization prospects: The 2014 revision, highlights. Technical report, United Nations, Department of Economic and Social Affairs, Population Division, 2014.

[5] Jorge Angeles. The qualitative synthesis of parallel manipulators. *Journal of Mechanical Design*, 126:617–624, July 2004.

[6] O. Bohigas, D. Zlatanov, L. Ros, M. Manubens, and J. M. Porta. A general method for the numerical computation of manipulator singularity sets. *IEEE Transactions on Robotics*, 30(2):340–351, April 2014.

[7] C.E. Borroni-Bird, A.B. Chernoff, and M.D. Shabana et al. Wheel module, October 2009.

[8] C.E. Borroni-Bird, R.L. Vitale, and J. Lee et al. Modular robotic vehicle, July 2015.

[9] Richard Budynas and Keith Nisbett. *Shigley's Mechanical Engineer Design*. Mc-Graw Hill Education, 9 edition, January 2010.

[10] John C. Dixon. *Suspension Geometry and Computation*. John Wiley Sons Ltd, Chichester, West Sussex, PO198SQ, United Kingdom, 2009.

[11] Grigore Gogu. Chebychev-grübler-kutzbach's criterion for mobility calculation of multi-loop mechanisms revisited via theory of linear transformations. *European Journal of Mechanics - A/Solids*, 24(3):427–441, February 2005.

[12] Grigore Gogu. *Structural Synthesis of Parallel Robots*, chapter 2. Springer, 3300 AA Dordrecht, The Netherlands, 2008.

[13] Grigore Gogu. *Structural Synthesis of Parallel Robots*, chapter 4. Springer, 3300 AA Dordrecht, The Netherlands, 2008.

[14] A. Goodarzi. Braking model. Lecture Notes, 2015.

[15] Clement Gosselin and Jorge Angeles. Singularity analysis of closed-loop kinematic chains. *IEEE Transactions on Robotics and Automation*, 6(3), June 1990.

[16] J. Hag. Wheel corner modules: technology and concept analysis. Master's thesis, Aeronautical and Vehicle Engineering, Royal Institute of Technology, Stockholm, Sweden, 2011.

[17] Bernd Heißing and Metin Ersoy, editors. *Chassis Handbook: Fundamentals, Driving Dynamics, Components, Mechatronics, Perspectives*, chapter 1, page 18. Vieweg+Teubner Verlag, 2011.

[18] Bernd Heißing and Metin Ersoy, editors. *Chassis Handbook: Fundamentals, Driving Dynamics, Components, Mechatronics, Perspectives*, chapter 3, page 221. Vieweg+Teubner Verlag, 2011.

[19] Bernd Heißing and Metin Ersoy, editors. *Chassis Handbook: Fundamentals, Driving Dynamics, Components, Mechatronics, Perspectives*, chapter 2, page 18. Vieweg+Teubner Verlag, 2011.

[20] Bernd Heißing and Metin Ersoy, editors. *Chassis Handbook: Fundamentals, Driving Dynamics, Components, Mechatronics, Perspectives*, chapter 5, page 221. Vieweg+Teubner Verlag, 2011.

[21] Z. Huang and Q.C. Li. Type synthesis of symmetrical lower-mboility parallel mechanisms using the constraint-synthesis method. *The International Journal of Robotics Research*, 22(1):59–79, January 2003.

[22] Daniel J. Inman. *Engineering Vibration*. Pearson Education, Inc., Upper Saddle River, New Jersey, US, 4 edition, 2014.

[23] M. Jonasson and J. Andreasson. Exploiting autonomous corner modules to resolve force constraints in the tyre contact patch. *Vehicle System Dynamics*, 46(7):553–573, July 2008.

[24] A. Khajepour, S. Fallah, and A. Goodarzi. *Electric and Hybrid Vehicles: Technologies, Modeling and Control: A Mechatronic Approach*, chapter 7. John Wiley & Sons Ltd, Chichester, West Sussex, PO198SQ, United Kingdom, 2014.

[25] D. Laurent and M. Sebe. Vehicle suspension having active camber variation, April 2003.

[26] D. Laurent, M. Sebe, and D. Walser. Assembly comprising a wheel and a suspension integrated into the wheel, September 2000.

[27] William F. Milliken and Douglas L. Milliken. *Race Car Vehicle Dynamics*, chapter 20. Society of Automotive Engineers, Inc., 400 Commonwealth Drive, Warrendale, PA 15069-0001 USA, 1995.

[28] William F. Milliken and Douglas L. Milliken. *Race Car Vehicle Dynamics*, chapter 18. Society of Automotive Engineers, Inc., 400 Commonwealth Drive, Warrendale, PA 15069-0001 USA, 1995.

[29] G. Nagaya. In-wheel motor system, October 2007.

[30] M.-A. Rajaie. Design and fabrication of a novel corner wheel module for urban vehicles. Master's thesis, University of Waterloo, Waterloo, ON, Canada, 2016.

[31] J. Ridley and B. Bluethmann. Mrv - modular robotic vehicle. Technical Report 20150019646, NASA, Houston, TX, November 2015.

[32] H. Sadjadian and H.D. Taghirad. Kinematic analysis of the hydraulic shoulder: A 3-dof redundant parallel manipulator. In *Mechatronics and Automation, 2005 IEEE International Conference*, pages 1442–1446, Niagara Falls, Canada, July 2005. IEEE.

[33] C.A. Sawyer. Around the ecorner. In C.A. Sawyer, editor, *Automotive Design & Production*, volume 118, page 52. Gardner Business Media Inc., 6915 Valley Avenue, Cincinnati, OH, US, October 2006.

[34] Hamid D. Taghirad. *Parallel Robots: Mechanics and Control*. Taylor & Francis Group, 6000 Broken Sound Parkway NW, Suite 300, Boca Raton, FL, 2013.

[35] A.J. Waters and A. Khajepour. Optimization of novel corner module for urban electric vehicle. In *Proceedings of the 19th International Conference on Advanced Vehicle Technologies*, Cleveland, OH, August 2017. ASME.

[36] S. Zetterström. Vehicle wheel suspension arrangement, May 2002.

[37] D. Zlatanov, R.G. Fenton, and B. Benhabib. Singularity analysis of mechanisms and robots via a velocity-equation model of the instantaneous kinematics. In *Proceedings of the 1994 IEEE International Conference on Robotics and Automation*, San Diego, CA, USA, May 1994. IEEE.

[38] Dimiter Zlatanov, Ilian A. Bonev, and Clément M. Gosselin. Constraint singularities as configuration space singularities. In *Proceeding of the Advances in Robot Kinematics (ARK)*, Caldes de Malavella, Spain, June 2002.

[39] Dimiter Zlatanov, Ilian A. Bonev, and Clément M. Gosselin. Constraint singularities of parallel mechanisms. In *Proceedings of the 2002 IEEE International Conference on Robotics and Automation*, Washington, DC, May 2002.

[40] D.S. Zlatanov. *Generalized Singularity Analysi of Mechanisms*. PhD thesis, University of Toronto, 1998.

APPENDICES

Appendix A

Concept Generation Tables

A.1 Generated Concepts from Grübler-Kutzbach Mobility Formula

Table A.1: Link and joint combinations

Joints	**Links**	**1 DOF Joints**	**2 DOF Joints**	**3 DOF Joints**
4	4	0	3	1
4	4	1	1	2
5	5	3	0	2
5	5	2	2	1
5	5	1	4	0
6	5	1	1	4
6	5	0	3	3
6	6	4	1	1
6	6	3	0	2

Joints	**Links**	**1 DOF Joints**	**2 DOF Joints**	**3 DOF Joints**
7	6	3	0	2
7	6	2	2	3
7	6	1	4	2
7	6	0	6	1
8	6	1	1	6
8	6	0	3	5
7	7	6	0	1
7	7	5	2	0
8	7	4	1	3
8	7	1	7	0
8	7	3	3	2
8	7	2	5	1
9	7	1	4	4
9	7	0	6	3
9	7	3	0	6
10	7	1	1	8
8	8	7	1	0
9	8	6	0	3
9	8	5	2	2
9	8	3	6	0
10	8	1	7	2
10	8	4	1	5
10	8	3	3	4
11	8	3	0	8
11	8	2	2	7
11	8	1	4	6
12	8	1	1	10

A.2 Configurations for Limb and Joint Combinations with Unknown Joints

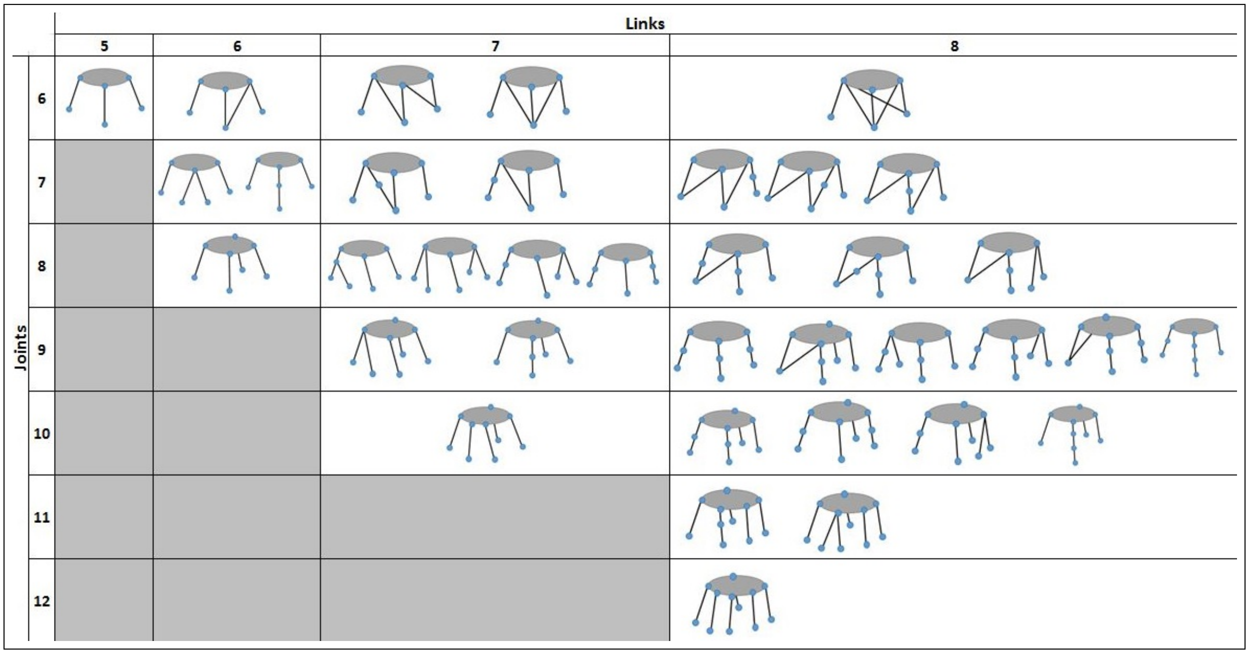

Figure A.1: Parallel mechanism configuration

Appendix B

Matlab Code

B.1 Genetic Algorithm

```matlab
% Lower and upper bounds
%     [ AIx, AIz, BIx,  Sx,  Sy,  Sz, AOix, AOiy, AOiz, BOix, BOiy, BOiz];
LB = [-280, 170, 100,-150,-180, 370, -250, -180,  160,    0, -180,  160];
UB = [-100, 315, 310,  20,-150, 450,    0, -150,  270,  250, -150,  270];

% Linear inequality constraints: A*x<=b
% AIx-AOix<=0
% BOix-BIx<=0
% BOix-AOix<=400
% AOiz-AIz<=-40
% AIz-AOiz<=100
% AOix-BOix<=-150
A = [1,0,0,0,0,0,-1,0,0,0,0,0;0,0,-1,0,0,0,0,0,0,1,0,0;...
      0,0,0,0,0,0,-1,0,0,1,0,0;0,-1,0,0,0,0,0,0,1,0,0,0;...
      0,1,0,0,0,0,0,0,-1,0,0,0;0,0,0,0,0,0,1,0,0,-1,0,0];
b = [0;0;400;-40;100;-150];

% Linear equality constraints: Aeq*x==beq
```

```
Aeq = [];
beq = [];

% Genetic algorithm options
options = gaoptimset('Display','iter','Generations',1000,...
    'PopulationSize',100,'TolCon',0.01,'PopInitRange',[LB;UB],...
    'CrossoverFraction',0.6,'FitnessLimit',0,'StallGenLimit',...
    10,'StallTimeLimit',2700,'PlotFcns',...
    {@gaplotbestf,@gaplotstopping});

% Run genetic algorithm
[x,fval,exitflag,output] = ga(@fitnessfun,12,A,b,Aeq,beq,LB,UB,[],options);
```

```
function [ obj ] = fitnessfun( x )
% Units are mm, kg, s
%% Inputs
% Fixed Points
AI = [x(1);-340;x(2)];        %Inboard rear actuator joint location
BI = [x(3);-340;x(2)];        %Inboard bar link joint location
S  = [x(4);x(5);x(6)];        %Outboard A-arm joint location

% Initial Points
AOi = [x(7);x(8);x(9)];       %Outboard rear actuator joint location
BOi = [x(10);x(11);x(12)];    %Outboard bar link joint location
Wi  = [0;0;315];              %Wheel inboard center location

%% Constants
minact = 200;
maxact = 600;
lB   = norm(BOi-BI);
c = [0,-5,-10,-15];
s = [25,20,15,10,5,0,-5,-10,-15,-20,-25];

%% Paramenter Initialization
xTravel = nan(length(c),length(s));
yTravel = nan(length(c),length(s));
```

```
ActLen1 = nan(length(c),length(s));
xTravel(1,length(s)) = 100;
xTravel(1,1) = 100;

%% Workspace Calculation
for i=1:length(c)
    for j=1:length(s)
        [xt,yt,~,~,A,~,~,~]=InverseKinematic(s(j),c(i),BI,BOi,AOi,BOi,...
                                                              S,lB,Wi);
        ActLen1(i,j)=norm(A-AI);
        if ActLen1(i,j)<maxact && ActLen1(i,j)>minact
            xTravel(i,j)=xt;
            yTravel(i,j)=yt;
        else
            ActLen1(i,j)=NaN;
        end
    end
end

%% Objective Function
if isnan(xTravel(1,11))
    xTravel(1,11)=100;
end
if sum(isnan(ActLen1(1,2:10)))<1
    if sum(isnan(ActLen1(4,4:8)))<1
        if sum(isnan(ActLen1(2,3:9)))<1
            yTravel0=max(yTravel(:,6));
            xTravelmin=min(xTravel(1,:));
            xTravelmax=max(xTravel(1,:));
            obj=2*abs(yTravel0-100)+1*abs(xTravelmin)+1*abs(xTravelmax)+...
                abs(xTravel(1,11));
        else
            obj=350;
        end
    else
        obj=400;
```

```
        end
else
    obj=500;
end

end
```

B.2 Inverse Kinematic Model

```
function [ CPx,CPy,CPz,W,AO,BO,CO,CPA,d ] = ...
                                InverseKinematics( s,c,BI,BOi,AOi,COi,S,RB,Wi )

s=s*pi/180;     %Steer angle [rad]
c=c*pi/180;     %Camber angle [rad]
Rz=[cos(-s),-sin(-s),0;sin(-s),cos(-s),0;0,0,1];
Rx=[1,0,0;0,cos(-c),-sin(-c);0,sin(-c),cos(-c)];
Si=S;

%% Solve Nonlinear Inverse Kinematic Model
xb = [BOi(1);BOi(2);BOi(3);0];                          %Initial Points
options = optimoptions('fsolve','Display','off');      %Options
[xs,fval] = fsolve(@(x)Kinematics(x,S,Si,BI,BOi,RB,Rx,Rz),xb,options);

BO = [xs(1);xs(2);xs(3)];   %Outboard fixed-length link joint
d = xs(4);                  %Spin angle [rad]

%% Linear Calculation of Joint and Contact Patch Locations
if sum(abs(fval))<0.001
    Ry  = [cos(xs(4)),0,sin(xs(4));0,1,0;-sin(xs(4)),0,cos(xs(4))];
    W   = Rz*Rx*Ry*(Wi-S)+S;     %Wheel Center
    AO  = Rz*Rx*Ry*(AOi-S)+S;    %Outboard rear cylinder joint
    CO  = Rz*Rx*Ry*(COi-S)+S;    %Outboard cross cylinder joint
    CPA = Rz*Rx*Ry*(-S)+S;       %Contact Patch without disc
```

```
        approximation

    % Contact Patch with Disc Approximation
    Wheelt = linspace(pi,2*pi-0.03142,500);
    Wheelx = Wi(1)-S(1)+315*cos(Wheelt);
    Wheely = Wi(2)-S(2)+315*0*Wheelt;
    Wheelz = Wi(3)-S(3)+315*sin(Wheelt);
    Wheelpnts     = [Wheelx;Wheely;Wheelz];
    % Parameter Initialization
    Wheelpntsnew = zeros(3,length(Wheelt));
    % Rotate all disc points
    for i=1:length(Wheelt)
        Wheelpntsnew(:,i)=Rz*Rx*Ry*Wheelpnts(:,i)+S;
    end
    CPz = min(Wheelpntsnew(3,:));              %z-component of contact patch
    index = find(Wheelpntsnew(3,:)==CPz);   %Index of contact patch
    CPx = Wheelpntsnew(1,index);              %x-component of contact patch
    CPy = Wheelpntsnew(2,index);              %y-component of contact patch
else
    CPx=NaN;
    CPy=NaN;
    CPz=NaN;
    W=nan(3,1);
    AO=nan(3,1);
    CO=nan(3,1);
    CPA=nan(3,1);
end
end
```

```
function [ Eq ] = Kinematics( x,S,Si,BI,BOi,RB,Rx,Rz )
%Unknown variables
BO = [x(1);x(2);x(3)];  %Outboard fixed-length link joint
b  = x(4);               %Spin angle [rad]

```

```
Ry = [cos(b),0,sin(b);0,1,0;-sin(b),0,cos(b)];

Eq1 = Rz*Rx*Ry*(BOi-Si)+S-BO;    %Rigid upright condition
Eq2 = abs(norm(BO-BI)-RB);       %Fixed-length link condition
Eq  = [Eq1;Eq2];
end
```

B.3 Forward Kinematic Model

```
function [ Eq ] = ForwardKinematics( x,AI,BI,CI,S,Pa,Pc,Pb,...
                             lA,lB,lC,lSA,lSB,lSC,lSAO,lSBO,lSCO )

s  = x(1);  %Steer angle [rad]
c  = x(2);  %Camber angle [rad]
b  = x(3);  %Spin angle [rad]
Ay = x(4);  %Normalized outboard rear cylinder y-component
Az = x(5);  %Normalized outboard rear cylinder z-component
By = x(6);  %Normalized outboard fixed-length link y-component
Bz = x(7);  %Normalized outboard fixed-length link z-component
Cy = x(8);  %Normalized outboard cross cylinder y-component
Cz = x(9);  %Normalized outboard cross cylinder z-component

v_SAI = S-AI;
v_SBI = S-BI;
v_SCI = S-CI;

cosA = (lSAO^2-lA^2-lSA^2)/(-2*lA*lSA);
cosB = (lSBO^2-lB^2-lSB^2)/(-2*lB*lSB);
cosC = (lSCO^2-lC^2-lSC^2)/(-2*lC*lSC);

Ax = (lSA*cosA-v_SAI(2)*Ay-v_SAI(3)*Az)/v_SAI(1);
Bx = (lSB*cosB-v_SBI(2)*By-v_SBI(3)*Bz)/v_SBI(1);
Cx = (lSC*cosC-v_SCI(2)*Cy-v_SCI(3)*Cz)/v_SCI(1);

a_unit = [Ax;Ay;Az];        %Rear cylinder unit vector
b_unit = [Bx;By;Bz];        %Fixed-length link unit vector
c_unit = [Cx;Cy;Cz];        %Cross cylinder unit vector
```

```

Rx = [1,0,0;0,cos(c),sin(c);0,-sin(c),cos(c)];
Ry = [cos(b),0,-sin(b);0,1,0;sin(b),0,cos(b)];
Rz = [cos(s),sin(s),0;-sin(s),cos(s),0;0,0,1];
R = Rz*Rx*Ry;                    %Wheel Rotation Matrix

Eq1 = S+R*Pa-AI-lA.*a_unit; %Loop closure for rear cylinder limb
Eq2 = S+R*Pb-BI-lB.*b_unit; %Loop closure for link limb
Eq3 = S+R*Pc-CI-lC.*c_unit; %Loop closure for cross cylinder limb

Eq=[Eq1;Eq2;Eq3];

end
```

B.4 Singularity Determination

B.4.1 Taghirad Method

```
function [ r ] = Singularity( AI,AO,BI,BO,CI,CO,S,c,s,b,Pa,Pc,Pb,
    Ps )

Rx = [1,0,0;0,cos(c),-sin(c);0,sin(c),cos(c)];
Ry = [cos(b),0,sin(b);0,1,0;-sin(b),0,cos(b)];
Rz = [cos(s),-sin(s),0;sin(s),cos(s),0;0,0,1];
R = Rz*Rx*Ry;

 la = norm(AO-AI);
 lc = norm(CO-CI);
 A_unit = (AO-AI)./la;
 C_unit = (CO-CI)./lc;
 B_unit = (BO-BI)./norm(BO-BI);
 wB_unit = (S-BI)./norm(S-BI);

% Active Jacobian Matrix
 Ja = [transpose(A_unit), transpose(cross(R*Pa,A_unit));...
       transpose(C_unit), transpose(cross(R*Pc,C_unit))];

```

```
RPb = R*Pb;
RPs = R*Ps;

C_Bx =  wB_unit(2)*B_unit(3)-B_unit(2)*wB_unit(3);
C_By = -wB_unit(1)*B_unit(3)+B_unit(1)*wB_unit(3);
Cx = RPb(1)-RPs(1);
Cy = RPs(2)-RPb(2);
Czy = RPb(3)-RPs(3);
Czx = -Czy;

Cwz = (C_Bx/(C_By*Czy))*(Cx-(C_By/C_Bx)*Cy);
Cwx = (C_Bx/(C_By*Czy))*Czx;

% Passive Jacobian Matrix
Jp = [         -RPs(3)*Cwx,  RPs(2)-RPs(3)*Cwz;...
                   RPs(3),            -RPs(1);...
         RPs(1)*Cwx-RPs(2),        RPs(1)*Cwz;...
                         1,                 0;...
                       Cwx,               Cwz;...
                         0,                 1];

% Combined Jacobian Matrix
J = Ja*Jp;

% Rank of Combined Jacobian Matrix
r = rank(J);

end
```

B.4.2 Zlatonov Method

```
function [ rL,rLI,rLO,rLP,L,LI,LO,LP] = SingularityZlatonov2( AI,
   AO,BI,BO,CI,CO,AOi,BOi,COi,S,c,s,b )
%Rotation Matrix
Rx = [1,0,0;0,cos(c),-sin(c);0,sin(c),cos(c)];
Ry = [cos(b),0,sin(b);0,1,0;-sin(b),0,cos(b)];
Rz = [cos(s),-sin(s),0;sin(s),cos(s),0;0,0,1];
R = Rz*Rx*Ry;
```

```

la = norm(AO-AI);         %Length of rear cylinder
lb = norm(BO-BI);         %Length of fixed-length link
lc = norm(CO-CI);         %Length of cross cylinder
A_unit = (AO-AI)./la;     %Rear cylinder unit vector
C_unit = (CO-CI)./lc;     %Cross cylinder unit vector
B_unit = (BO-BI)./lb;     %Fixed-length link unit vector

O = zeros(3,3);
vO = zeros(3,1);

vRSA = R*(S-AOi);
vRSB = R*(S-BOi);
vRSC = R*(S-COi);
vRAC = R*(AOi-COi);

WA = -skew3(vRSA);
WB = -skew3(vRSB);
WC = -skew3(vRSC);
AC = -skew3(vRAC);
wA = skew3(la.*A_unit);
wB = skew3(lb.*B_unit);
wC = skew3(lc.*C_unit);

%% Jacobian Matrix Calculations
L = [WA, A_unit,      vO,-wA,   O,   O;...
     WB,     vO,      vO,   O,-wB,   O;...
     WC,     vO,  C_unit,   O,   O,-wC;...
     %tO,     0,       0,  tO, TB, tO;
     AC, A_unit,-C_unit,-wA,   O, wC];     %Full Jacobian Matrix

LI = [L(:,1:3),L(:,6:14)];   %Input Jacobian Matrix
LO = L(:,4:14);              %Output Jacobian Matrix
LP = L(:,6:14);              %Passive Jacobian Matrix

%% Rank Calculations
rL = rank(L);                %Rank of Full Jacobian Matrix
rLI = rank(LI);              %Rank of Input Jacobian Matrix
```

```
rLO = rank(LO);                 %Rank of Output Jacobian Matrix
rLP = rank(LP);                 %Rank of Passive Jacobian Matrix

end
```

B.5 3DOF Handling Model Simulink Diagram

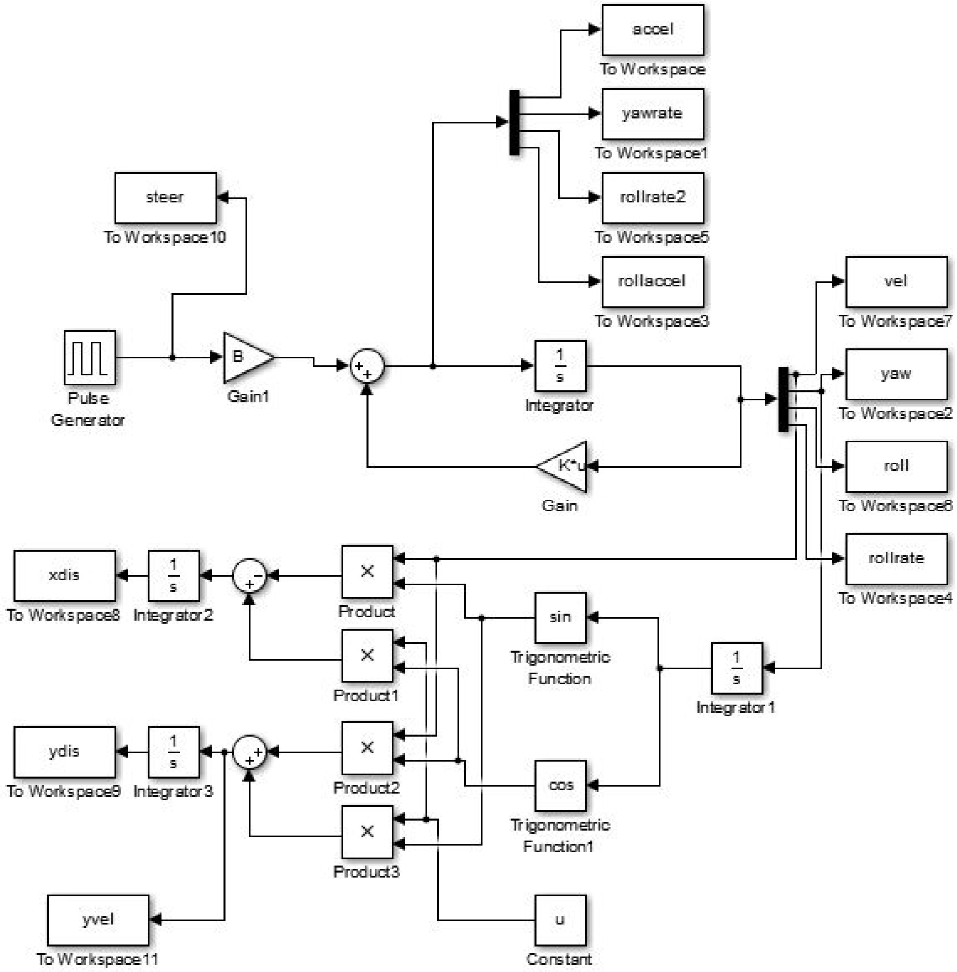

Figure B.1: Simulink diagram for 3DOF handling model.

B.6 2DOF Quarter Car Model Simulink Diagram

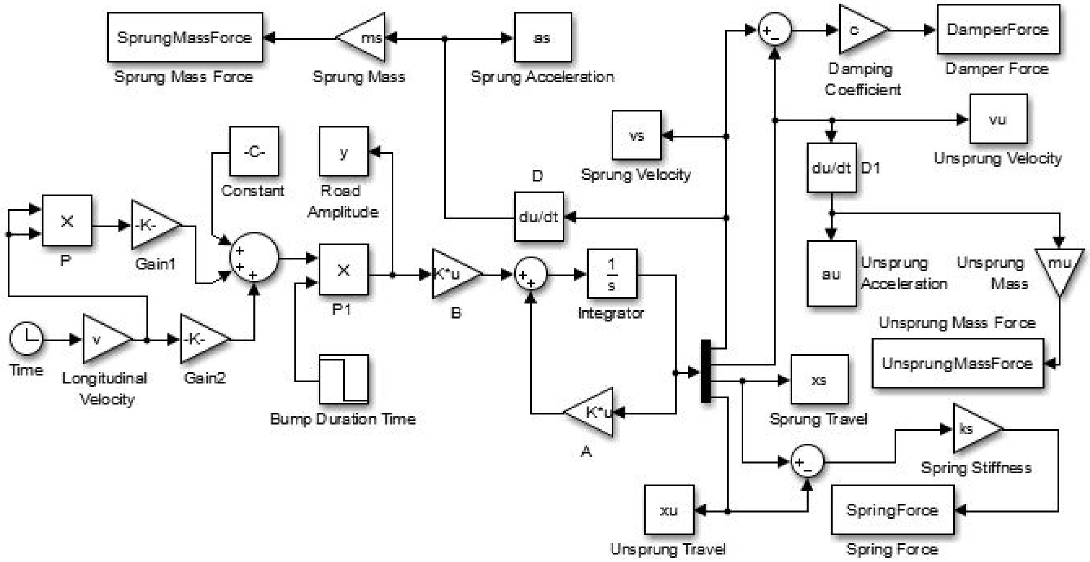

Figure B.2: Simulink diagram for 2DOF quarter car model.

GLOSSARY

bump camber Wheel rotation about the wheel's x-axis induced by the wheel traversing a bump or pothole. 7, 60

bump scrub Wheel translation along the wheel's y-axis induced by the wheel traversing a bump or pothole. 7

bump steer Wheel rotation about the wheel's z-axis induced by the wheel traversing a bump or pothole. 7, 15

camber-by-roll Wheel rotation about the wheel's x-axis induced by body roll. 7, 60

caster offset The longitudinal distance between the kingpin axis and the center of the wheel. When the kingpin axis is in front of the wheel center, caster trail is said to be positive. 6

caster trail The longitudinal distance between the kingpin axis and the contact patch at the ground. When the kingpin axis is in front the contact patch at ground level, caster trail is said to be positive. 6

inclination offset The lateral distance between the kingpin axis and the contact patch at the ground. When the kingpin axis is angled towards the body, the inclination angle is said to be positive 6, 7

scrub-by-roll Wheel translation along the wheel's y-axis induced by body roll. 7

singularity A position in a mechanism's workspace where a large change in actuator input results in little to no mechanism output motion or a large change in mechanism output motion occurs without any actuator input. 12

steer-by-roll Wheel rotation about the wheel's z-axis induced by body roll. 7

tadpole configuration A configuration of a three-wheeled vehicle having two wheels in the front and one wheel in the back. 3